Air Pocket Modeling in Water Mains With an Air Valve

by

Bernardo Carvalho Trindade

A thesis submitted to the Graduate Faculty of
Auburn University
in partial fulfillment of the
requirements for the Degree of
Master of Science

Auburn, Alabama
May 7, 2012

Keywords: Water, Air, Water Mains

Approved by

José Goes Vasconcelos Neto, Chair, Professor of Civil Engineering
Prabakhar Clement, Professor of Civil Engineering
Xing Fang, Professor of Civil Engineering

Abstract

Water mains filling events follow certain maintenance operations that require the complete or partial emptying of pipelines. These operational procedures are performed carefully in order to prevent air pocket formation, as such pockets may trigger damaging surges, as well impose blockages that reduce pipe conveyance. While previous research addressed the modeling of the pipeline filling events, the air phase within the conduits is in most cases either not included in the simulation, or its formulation is very simplified, not including air pressure gradients. This paper presents two modeling frameworks which couple a Two-Component Pressure Approach model to simulate water flow with models for the air phase flow within the conduits. The first is a discretized model for air phase based on the isothermal Euler equations and the second is based on the ideal gas law (as presented in [Zhou et al., 2002a]). Also, the results of an experimental investigation with an apparatus based on the experimental setup presented by [Trajkovic et al., 1999] without ideal ventilation which includes the essential features of a pipeline filling event are presented and discussed. Relevant and flow features characteristics during the filling event are analyzed such as the occurrence of interface breakdown. These experimental results as well as field data of the filling of an actual water main are used to calibrate and assess the model. A feasible modeling framework to simulate the filling of water mains accounting for air effects was presented. Also, it was demonstrated that lumped approach for air phase modeling has comparable accuracy with discretized model based on Euler equations at a much reduced computational effort.

Acknowledgments

I would like to thank my advisor and friend, Professor Jose Goes Vasconcelos, for all the patience and time spent in the development of my numerical and experimental research, as well as for all the funny talks about all sorts of non professional topics which made work more pleasant. I also would like to thank Carmen Chosie for the help in the laboratory with the experiments (and with the squeegee) and my dear friend Paulo Ferreira for the help with programming.

I would like also to thank my parents, Aluisio (dad) and Regina (mom) Trindade, whose examples were the most important inspiration source for me to move on and want to always achieve greater things in life, both professionally and personally. My thanks to my dear sister, Helena Trindade, for all the funny and sad moments shared up until now, for the constant support during easy and hard times here so far away from home, and for making everything in life more colorful to me.

Finally, I am also grateful to all my friends in the civil engineering department who made my time spent in the university very enjoyable. Those are: Gabriel Leite, Zheng Min, Luana Ozelim, Jessica Looper, Tom Hatcher, the nepalian crew (Sushban Shrestha, Nirajan Dhakal and Manoj KC). I would like also to thank Audrey Blackmon for the nice and calming resting breaks and for being with me at late nights while I wrote the the second half of this document.

Table of Contents

List of Figures

List of Tables

List of Abbreviations

a	celerity the acoustic waves in the pressurized flow
A	water flow cross sectional area
A_{orif}	orifice area
A_{air}	air flow cross sectional area $\frac{\pi}{4}D^2 - A$
b_{vel}	pressurizing bore velocity
C_d	discharge coefficient that is assumed as $C_d = 0.65$
d_{orif}	ventilation orifice diameter
d^*	normalized ventilation diameter d_{orif}/D
D	pipeline diameter E is the total energy per unit volume
f	friction head loss in the short pipe portion inside the boundary condition right after the inlet
F_g	Gravitaty force acting on a control volume
F_{Shear}	Shear force acting on a control volume
$\mathbf{F}(\mathbf{U})$	vector with the flux of conserved variables
g	acceleration of gravity
h_c	distance between the free surface and the centroid of the flow cross section (limited to $D/2$)

h_s surcharge head

h_{air} extra head due to entrapped air pocket pressurization

H_{res} reservoir water level

K elasticity modulus of the material

K_{eq} overall local loss coefficient in the inlet

M_{air} mass of air within the pocket

$M_{air\,out}$ air mass that escapes through the ventilation orifice

MOC Method of characteristics

n time step index

P_{wet} water flow wet perimeter

Q water flow rate

Q^* normalized flow rate $Q/\sqrt{gD^5}$

Q_{rec} water flow rate which is admitted into the reservoir from the recirculation system

Q_{in} water flow rate which enters the upstream end of the pipe

$\mathbf{S}$ vector of source terms

S_1 source term for a continuity equation

S_2 source term for a momentum equation

$S_{disp,i}$ source term that accounts for air displacement

S_f source term that accounts for shear stress between air and pipe walls

t time

u flow velocity

$\mathbf{U}$ vector of the conserved variables

$\check{\mathbf{U}}$ vector conserved variables prior to air displacement correction

UAPH Uniform air pressure head

V_p air pocket volume

w_{depth} local water depth

wet_i boolean variable that is true if the cell is considered wet and false is considered dry bed. Being dry implies that the flow in the cell will not be calculated

x x axis direction

y y axis direction

z z axis direction or pipe elevation relative to the datum

τ_0 shear tension between water and the pipe walls

α celerity of the acoustic waves in the air

Δx control volume's length

γ water specific weight

ρ specific mass of water

ρ_{air} specific mass of air

ϕ correction factor for air displacement source terms

θ angle formed by free surface flow width and the pipe centerline or between the channel bottom the a horizontal line

Chapter 1

Introduction

Water mains are important components of the urban infrastructure designed to operate in pressurized flow mode, but under abnormal operational conditions air phase may be present within the conduits. Such conditions are commonly observed during the filling and emptying of water mains, but may also occur following accidental water main ruptures. Those conditions can also happen when water demand exceeds supply, in which case the pipes act as reservoirs. In the process of filling, the air phase present in the pipeline may become entrapped between masses of water, creating air pockets, which should be eliminated by air valves located at selected points along the pipeline. The appearance of these entrapped air pockets in pipelines is well documented in several experimental investigations, such as [Falvey, 1980], [Zhou et al., 2002b], [Vasconcelos et al., 2006].

Entrapped air pockets can cause loss of pipe cross-section, localized head losses, high transient pressures, and other problems if not properly expelled. Yet, even with air valves, the refilling process is often performed cautiously. The reason for this are the potentially damaging surges that may occur due to the air-water interactions during the pipe filling and to ensure that no air pocket remains in the pipe. Because of these uncertainties, the filling is generally performed slowly, and the restoring of normal pipeline conditions may take several hours, or even days, depending on the event that caused disruption of the distribution system. Because this flow interruption has major impacts in water consumers, the ability to quickly and safely restore operational conditions in water mains is highly desirable. Therefore, it is important to understand how to predict the appearance of an air pocket and how to mitigate their effects.

Numerical models represent a feasible way to minimize the uncertainties related to the air-water interactions during the filling process. Three dimensional, CFD packages are a possible solution, but considering some characteristics of the problem, these solutions are not practical. Some of those characteristics are the length of the pipeline systems, the complex geometry of some pipeline elements (e.g. partially closed valves), the flow unsteadiness, and the time scale of the filling events (up to several hours of unsteady flow conditions). One dimensional, unsteady flow models would be an alternative, but they also have limitations. Unsteady flow models in use by water work authorities, usually applied to assess waterhammer effects and closed pipe surges, assume homogeneous, single-phase flow conditions. By contrast, the refilling process is characterized by two-phase, stratified flow conditions, invalidating the assumed hypothesis in such single phase models, as demonstrated by [Vasconcelos, 2008]. Therefore, engineers still lack a model which can simulate air pockets in a precise and realistic way. Progress in the area still have not resulted in a tool to help engineers to simulate pipeline priming, particularly considering the effects of entrapped air.

Similarly to other events that involve the transition between pressurized and free surface flows (also referred to as mixed flows), there are certain characteristics on water pipeline filling events that are challenging to numerical models:

1. Even though there are a variety of models which are able to handle flow regime transition, such models have limitations and difficulties which include the complexity of the model itself, post-shock oscillations, limitation on the interaction between bores, and others;

2. This is a two-phase (air/water) problem, and models handling the two separate phases need to be appropriately linked. The handling of the interface between air and water is particularly challenging;

3. Due to the formation of bores and the differences in the celerity magnitudes among different portions/phases of the flow, non-linear numerical schemes should be used.

This is required to account for both free-surface and water pressurized at the same time limiting issues related to diffusion and oscillations at bores and shocks;

4. At certain regions of the flow, particularly at the vicinity of curved air-water interfaces, shallow water assumptions are not applicable due to strong vertical acceleration, and the problem is intrinsically three-dimensional [Benjamin, 1968];

5. Several different mechanisms may result in the entrapment of air pockets during filling events, and conditions leading to such entrapments still not fully understood, thus cannot be numerically predicted.

1.1 Different types of flows and their classification

Water flows can occur in several different applications in engineering. However, the characteristics of those flows change from application to application. All of them are strictly three dimensional in space and also varies with time, even if this variation is very gradual. Also, they can have different phases, mildly variable specific mass according to the pressure, can be a free surface or pressurized, and turbulent or laminar.

However, it's very difficult to take all relevant characteristics of water flows into consideration when a study is required on a particular case. As one attempts to create a predictive model of a flow in particular conditions, hypothesis are introduced to minimize the complexity of the analysis and are related to how the model handles some of the aforementioned characteristics. For instance, regarding the time dependency, flows can be considered steady or transient. The later are more difficult to model, many times requiring the solution of a set of partial differential equations (PDE) such as the Saint-Venant equations showed in [Cunge et al., 1980], [Sturm, 2001] and [Chaudhry, 2008]. In other applications, when the temporal variation is negligible, flows are assumed to be steady, which eliminates time from analysis, making it much simpler.

A flow with phases that do not mix completely is named a multi-phase flow. For those cases, each flow may be analyzed using a different set of coupled partial differential equations. This increases the problem difficulty due to the increased number and complexity of those equations that needs to be solved. However, in some cases the properties of both phases can averaged for a certain volume of flow, as in the work presented by [Issa and Kempf, 2003], simplifying the model solution.

Another important factor is whether the flow is opened to the atmosphere or not. In the case of rivers, channels, lakes and other flows in that are not confined, the flow is referred to as free-surface flow. The biggest challenge when modeling this type of flow appears when dealing with the water surface variation in a one, two or three-dimensional transient analysis, so that very sophisticated numerical techniques such as finite volumes or volume of fluid (VOF) must be applied. On the other hand, in case of pressurized water pipes, confined aquifers, drainage pipes, and other flows, the flow is referred to as pressurized flow. Those have known cross section, and techniques to simulate them are more consolidated up to date, such as the Method of Characteristics for closed pipes. There is still the case in which both free-surface and pressurized flow regimes coexist in the same flow, such as in drainage systems, water main filling events, gas/oil transmission lines, and others.

1.2 Mathematical models for 1-D water

The model presented in subsection 1.2.1 is used to simulate unsteady flows in closed conduits, while the model presented in subsection 1.2.2 is used for unsteady free-surface flows. The methods for the solution of these equations are presented in section 1.4.

1.2.1 Derivation of unsteady fully pressurized flows equations

In this section, the equations for mass and momentum conservation in pressurized flows are presented. Those equations are the basis for the unsteady flows in pipe models.

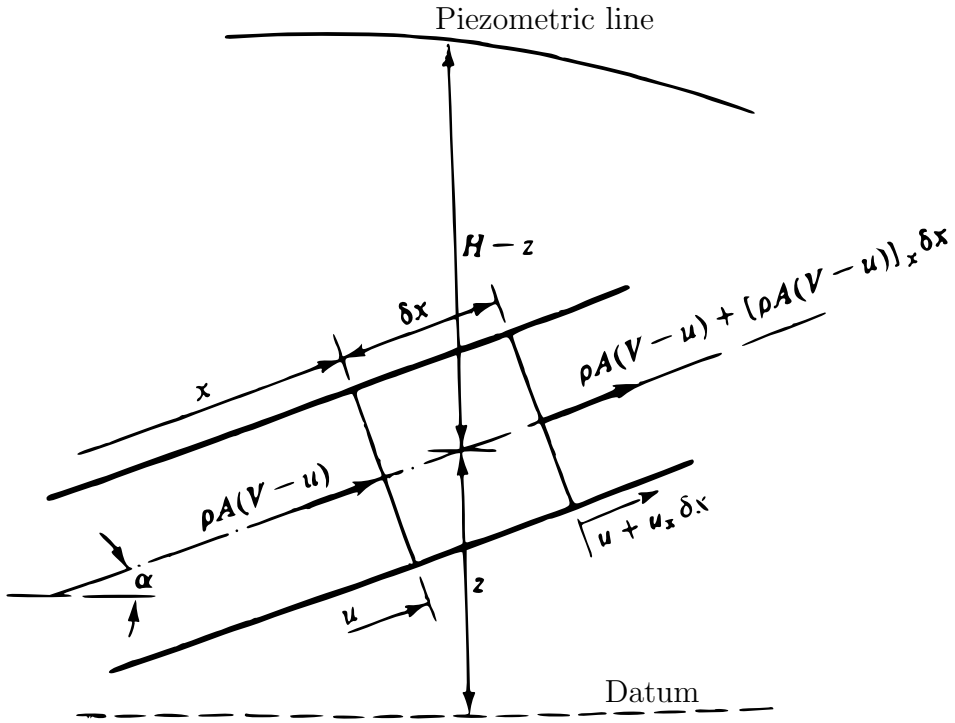

Figure 1.1: Control volume for continuity equation derivation. Adapted from [Wylie and Streeter, 1993]

Continuity Equation

Figure 1.1 shows a control volume inside a pipe where water would enter from the left. It is possible to have some amount of water stored inside this control volume due to an stretch of the pipe cross-section or length or the to compression of the water mass. Applying the mass continuity the control volume of figure 1.1 yields:

$$\rho A u - \left[\rho A u + \frac{\partial}{\partial x}(\rho A u)\Delta x\right] = -\frac{\partial}{\partial t}\rho A \Delta x \tag{1.1}$$

$$A u \frac{\partial \rho}{\partial x} + \rho\left(u\frac{\partial A}{\partial x} + A\frac{\partial u}{\partial x}\right) = -A\frac{\partial \rho}{\partial t} - \rho\frac{\partial A}{\partial t} \tag{1.2}$$

where A is the pipe's cross-section area, p is the local pressure, Δx is the control volume's length, ρ is the water specific mass, t is the time, u is the flow velocity. Dividing both sides by ρA yields:

$$\frac{1}{\rho}\frac{\partial \rho}{\partial t} + \frac{1}{\rho}\frac{\partial \rho}{\partial x}u + \frac{1}{A}\frac{\partial A}{\partial t} + \frac{1}{A}\frac{\partial A}{\partial x}u + \frac{\partial u}{\partial x} = 0 \tag{1.3}$$

$$\frac{1}{\rho}\frac{d\rho}{dt} + \frac{1}{A}\frac{dA}{dt} + \frac{\partial u}{\partial x} = 0 \tag{1.4}$$

For convenience, the first term of Equation 1.4, which represent the compressibility effects, should be rewritten in terms of pressure. For this, the bulk modulus of elasticity concept described in equation 1.5 is used :

$$\frac{1}{\rho}\frac{d\rho}{dt} = \frac{1}{K}\frac{dp}{dt} \tag{1.5}$$

in which K is the elasticity modulus of the material. This concept assumes negligibility of the thermodynamic effects, which is a good hypothesis due to the low compressibility of water [Vasconcelos, 2007].

For a prismatic pipe, which is the case in most practical applications [Wylie and Streeter, 1993], the gradient $\frac{\partial A}{\partial x}$ is equal to 0. Hence, the variation of the pipe cross-section area is related only to the variation of the pressure, as in equation 1.6

$$\frac{dA}{dt} = \frac{\partial A}{\partial p}\frac{dp}{dt} \tag{1.6}$$

Replacing the two first terms in equation 1.4 by equations 1.5 and 1.6:

$$\frac{1}{K}\frac{dp}{dt} + \frac{1}{A}\frac{dA}{dp}\frac{dp}{dt} + \frac{\partial u}{\partial x} = 0 \tag{1.7}$$

$$\frac{1}{K}\frac{dp}{dt}\left(1 + \frac{K}{A}\frac{dA}{dp}\right) + \frac{\partial u}{\partial x} = 0 \tag{1.8}$$

According to [Wylie and Streeter, 1993], the wave propagation velocity (celerity of the acoustic wave) in a pressurized pipe is given by the expression:

$$a^2 = \frac{K/\rho}{1 + (K/A)(dA/dp)} \tag{1.9}$$

which can be written as:

$$\frac{K}{A}\frac{dA}{dp} = \frac{K}{a^2\rho} - 1 \tag{1.10}$$

and then inserted in equation 1.8 yielding:

$$\frac{dp}{dt}\frac{1}{a^2\rho} + \frac{\partial u}{\partial x} = 0 \tag{1.11}$$

$$\frac{\partial p}{\partial t}\frac{1}{a^2\rho} + \frac{\partial p}{\partial x}\frac{u}{a^2\rho} + \frac{\partial u}{\partial x} = 0 \tag{1.12}$$

According to [Wylie and Streeter, 1993], for low Mach numbers ($u \ll a$) $u/a^2 \approx 0$. With this approximation the second term of equation 1.12 can be dropped, yielding:

$$\frac{\partial p}{\partial t}\frac{1}{a^2\rho} + \frac{\partial u}{\partial x} = 0 \tag{1.13}$$

The pressure in the pipe is related to the piezometric head H according to the expression:

$$p = \rho g(H - z) \tag{1.14}$$

in which z is the pipe elevation relative to the datum. Applying this expression in equation 1.13, multiplying both sides by a^2 and dividing by g, and considering that $\frac{\partial z}{\partial t} = 0$ yields:

$$\frac{\partial H}{\partial t} + \frac{a^2}{g}\frac{\partial u}{\partial x} = 0 \tag{1.15}$$

Note that in case of lateral in/outflow considered in the control volume of figure 1.1, the mass conservation equation 1.15 would show a third term (source term), as shown in [McInnis and Karney, 1995] and [Wylie and Streeter, 1993]:

$$\frac{\partial H}{\partial t} + \frac{a^2}{g}\frac{\partial u}{\partial x} + \frac{a^2}{gA}q = 0 \tag{1.16}$$

in which q is the volume of water gained/lost per length per time.

Momentum Equation

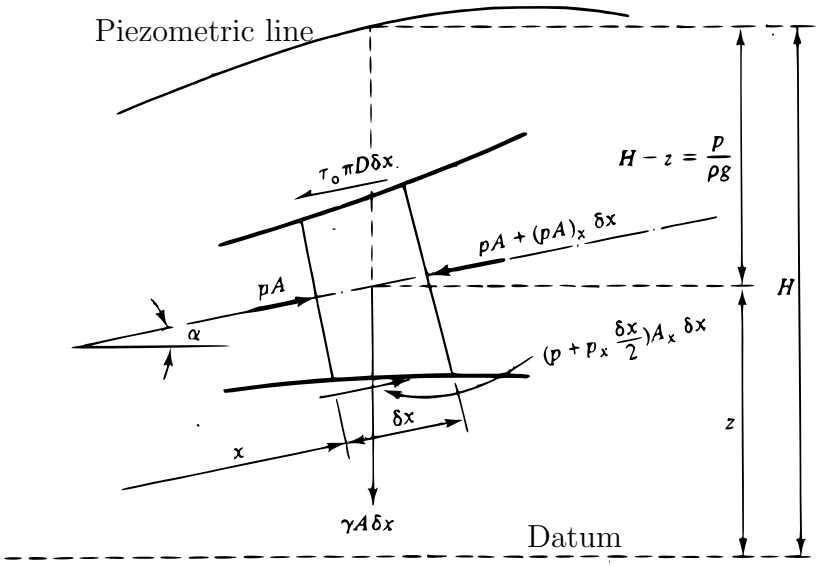

Figure 1.2: Control volume for momentum equation derivation. Adapted from [Wylie and Streeter, 1993]

The application of Newton's second law to the control volume in figure 1.2, where the summation of all the external forces applied to the control volume is equal to the variation of momentum, yields:

$$pA - \left(pA + \frac{\partial}{\partial x}pA\Delta x\right) + p\frac{\partial A}{\partial x}\Delta x - \gamma A \Delta x sin\alpha - \tau_0 \pi D \Delta x = \rho A \frac{du}{dt}\Delta x \tag{1.17}$$

in which γ is the water specific weight, τ_0 is the shear tension between water and the pipe walls, D is the pipe diameter, and α is the pipe slope. Expanding the derivative of pA, dividing both sides by Δx and canceling terms yields:

$$- A\frac{\partial p}{\partial x} - p\frac{\partial A}{\partial x} + p\frac{\partial A}{\partial x} - \gamma A sin\alpha - \tau_0 \pi D = \rho A \frac{du}{dt} \tag{1.18}$$

which leads to:

$$- A\frac{\partial p}{\partial x} + \gamma A sin\alpha - \tau_0 \pi D = \rho A \frac{\partial u}{\partial t} \tag{1.19}$$

Knowing that $\frac{\partial z}{\partial x} \approx sin\alpha$ and using the hydrostatic hypothesis represented by equation 1.14, equation 1.19 can be rewritten as:

$$- \rho g A \left(\frac{\partial H}{\partial x} - sin\alpha \right) - \rho g A sin\alpha - \tau_0 \pi D = \rho A \frac{\partial u}{\partial t} \tag{1.20}$$

Canceling terms and dividing both sides by ρA yields:

$$- g\frac{\partial H}{\partial x} - \frac{4\tau_0}{\rho D} - \frac{\partial u}{\partial t} = 0 \tag{1.21}$$

According to [Wylie and Streeter, 1993] the shear stress in pipe flows τ_0 can be written as:

$$\tau_0 = \rho f \frac{u^2}{8} \tag{1.22}$$

with f as the friction factor. Writing u^2 as $u|u|$, in order to avoid gain of energy in case of a negative discharge, the momentum equation is obtained:

$$g\frac{\partial H}{\partial x} + \frac{\partial u}{\partial t} + f\frac{u|u|}{2D} = 0 \tag{1.23}$$

With this, the set of PDEs that describe unsteady, pressurized flow in pipes becomes:

$$\begin{cases} \dfrac{\partial H}{\partial t} + \dfrac{a^2}{g}\dfrac{\partial u}{\partial x} = 0 \\ g\dfrac{\partial H}{\partial x} + \dfrac{\partial u}{\partial t} + f\dfrac{u|u|}{2D} = 0 \end{cases} \tag{1.24}$$

1.2.2 Free surface flows equations: the Saint-Venant equations

The Saint-Venant equations are also a mathematical model to express mass and momentum conservations, but unlike the previous case, the Saint-Venant equations were derived for one-dimensional free-surface flows such as rivers and channels. The hypothesis assumed in the derivation are discussed in [Sturm, 2001], [Vasconcelos, 2007], and others, and are:

- The flow is unidimensional, resulting in a hydrostatic pressure distribution along the vertical axis of the channel cross-section hydrostatic;
- The slope is small, thus $sin(\theta) = \theta$;
- The fluid (water) is incompressible, thus ρ is constant;
- The water depth is small when compared to the wave length;
- The channel's bed is stable (e.g. no movable bed conditions);
- The shear tensions are constant and do not depend on the transient nature of the flow.

Mass conservation equation

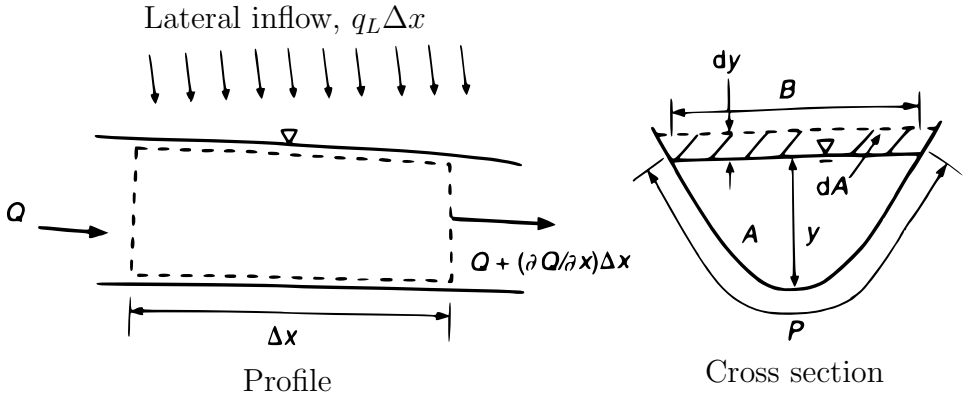

Figure 1.3: Control volume for momentum equation derivation. Adapted from [Sturm, 2001]

Mass balance on figure 1.2.2 yields:

$$Q - \left(Q + \frac{\partial Q}{\partial x}\Delta x \Delta t\right) + q_L \Delta x \Delta t = \frac{\partial A}{\partial t}\Delta x \Delta t \tag{1.25}$$

Which when simplified yields:

$$\frac{\partial A}{\partial t} + \frac{\partial Q}{\partial x} = q_L \tag{1.26}$$

Momentum conservation

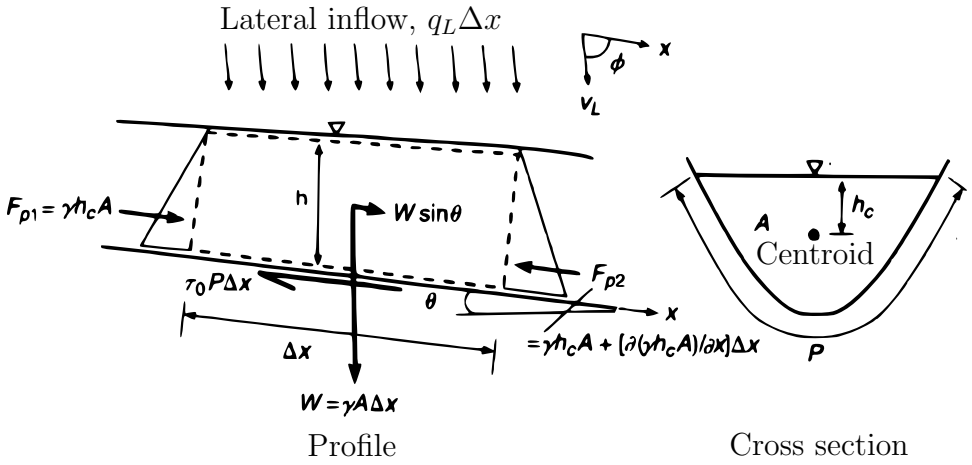

Figure 1.4: Control volume for momentum equation derivation. Adapted from [Sturm, 2001]

To derive the momentum equation, second Newton's law is applied to the system in the figure 1.4. The net momentum flux and external forces balance is:

$$\frac{\partial(\rho A \Delta x \cdot u)}{\partial t} + \frac{\partial(\rho A \Delta x u \cdot u)}{\partial x} = \gamma h_c A - (\gamma h_c A + \frac{\partial(\gamma h_c A)}{\partial x}\Delta x) + F_g - F_{shear} \tag{1.27}$$

where

$$F_g = \gamma A \Delta x sin(\theta) \approx \gamma A \Delta x S_0 \tag{1.28}$$

$$F_{shear} = \tau_0 P_{wet} \Delta x \tag{1.29}$$

With further mathematical development and combining the equations, one obtains:

$$\frac{\partial(\rho A \cdot u)}{\partial t} + \frac{\partial(\gamma h_c A)}{\partial x} + \frac{\partial(\rho A u \cdot u)}{\partial x} = \gamma A S_0 - \tau_0 P_{wet} \tag{1.30}$$

where h_c is the distance from the water surface to the centroid of the flow cross-section, θ is the channel slope in degrees, S_0 is the channel slope in percentage and P_{wet} is the wet perimeter. Assuming that $Au = Q$, ρ is constant, S_f is the friction slope (boundary friction force for each unit weight of water per Δx), so that $S_f = \frac{\tau_0 P_{wet}}{\gamma A}$, the channel is prismatic, and there is no lateral inflow, ρ is canceled in both sides yielding:

$$\frac{\partial Q}{\partial t} + \frac{\partial}{\partial x}\left(\frac{Q^2}{A} + g h_c A\right) = g A (S_0 - S_f) \tag{1.31}$$

Therefore, the final set of equations which are called the Saint-Venant equations is:

$$\begin{cases} \dfrac{\partial A}{\partial t} + \dfrac{\partial Q}{\partial x} = q_L \\ \dfrac{\partial Q}{\partial t} + \dfrac{\partial}{\partial x}\left(\dfrac{Q^2}{A} + g h_c A\right) = g A (S_0 - S_f) \end{cases} \tag{1.32}$$

which can also be written in conservative format:

$$(\mathbf{U})_t + \mathbf{F}_x(\mathbf{U}) = \mathbf{S}(\mathbf{U}) \tag{1.33}$$

where

$$\mathbf{U} = \begin{bmatrix} A \\ Q \end{bmatrix},\ \mathbf{F}(\mathbf{U}) = \begin{bmatrix} Q \\ \frac{Q^2}{A} + g A h_c \end{bmatrix},\ \mathbf{S}(\mathbf{U}) = \begin{bmatrix} 0 \\ g A (S_0 - S_f) \end{bmatrix} \tag{1.34}$$

1.3 Mathematical models for air phase flows

This section presents the background for the two alternatives of air-phase modeling implemented in this work. For the discretized alternative, the largely documented Euler

equations were chosen. A simpler implementation of the ideal gas law was chosen as the non-discretized air model because of its simplicity, easiness to implement, and low computational requirements. For the air flow in the air pockets, the following hypothesis were considered:

- Viscosity is negligible: shear forces due to viscosity are negligible when compared to the impelling forces caused by the air-water interaction;
- The flow is uni-dimensional (1-D): the length of the pocket is much bigger than its lateral dimensions;
- Isothermal flow: The temperature variation of the air flow during is small.

1.3.1 Euler equations

The most complete set of equations for the study of flows is the Navier-Stokes equation, which can be found in [Potter, 2004] and other books. However, they are still very difficult to solve, so that simplification hypothesis are of great advantage. With the no shear hypothesis, the viscosity terms of the Navier-Stokes equations disapear and it turns into the Euler equations (equation 1.35), which can be found in [LeVeque, 1992], [Toro, 2009] and other books.

$$(\mathbf{U})_t + \mathbf{F}_x(\mathbf{U}) + \mathbf{G}_y(\mathbf{U}) + \mathbf{H}_z(\mathbf{U}) = \mathbf{S}(\mathbf{U}) \tag{1.35}$$

$$\left.\begin{aligned} \mathbf{U} = \begin{bmatrix} \rho \\ \rho u \\ \rho v \\ \rho w \\ E \end{bmatrix}, \quad \mathbf{F}(\mathbf{U}) = \begin{bmatrix} \rho u \\ \rho u^2 + p \\ \rho uv \\ \rho uw \\ u(E+p) \end{bmatrix}, \mathbf{G}(\mathbf{U}) = \begin{bmatrix} \rho v \\ \rho uv \\ \rho v^2 + p \\ \rho vw \\ v(E+p) \end{bmatrix}, \\ \mathbf{H}(\mathbf{U}) = \begin{bmatrix} \rho w \\ \rho uw \\ \rho vw \\ \rho w^2 + p \\ w(E+p) \end{bmatrix}, \mathbf{S}(\mathbf{U}) = \begin{bmatrix} S_1 \\ S_2 \\ S_3 \\ S_4 \\ S_5 \end{bmatrix} \end{aligned}\right\} \tag{1.36}$$

where ρ is the fluid specific mass, u, v and w are the fluid velocity in the x, y an z axis, p is the pressure, and E is the total energy per unit volume. The source terms S_n can represent several features of the flow, such as shear stresses and flow area variations, and will be discussed later.

The full version of the Euler equations is a three-dimensional, hyperbolic and non-linear conservative set of partial differential equations, relatively complex and costly to solve. With the application of the second hypothesis (1-D flow), the equations are simplified to equation 1.37:

$$(\mathbf{U})_t + \mathbf{F}_x(\mathbf{U}) = \mathbf{S}(\mathbf{U}) \tag{1.37}$$

where

$$\mathbf{U} = \begin{bmatrix} \rho \\ \rho u \\ E \end{bmatrix}, \ \mathbf{F}(\mathbf{U}) = \begin{bmatrix} \rho u \\ \rho u^2 + p \\ u(E+p) \end{bmatrix}, \ \mathbf{S}(\mathbf{U}) = \begin{bmatrix} S_1 \\ S_2 \\ S_3 \end{bmatrix} \tag{1.38}$$

Further, according to [LeVeque, 1992], for a isothermal problem the energy is constant, making the energy derivatives equal to zero. This leads to equation 1.39:

$$\mathbf{U} = \begin{bmatrix} \rho \\ \rho u \end{bmatrix}, \ \mathbf{F}(\mathbf{U}) = \begin{bmatrix} \rho u \\ \rho u^2 + p \end{bmatrix}, \ \mathbf{S}(\mathbf{U}) = \begin{bmatrix} S_1 \\ S_2 \end{bmatrix} \tag{1.39}$$

with

$$p = \rho a^2 \tag{1.40}$$

where a is the sound speed in the air. Since, according to [Tran, 2011], the flow condition in pipeline fillings may be approximated to isothermal conditions, equation 1.39 is the set of equations used in the discretized model.

1.3.2 Ideal gas law

The ideal gas law, which was first presented in [Krönig, 1856], states that the state of a mass of a gas depends on its pressure, volume, temperature, the ideal gas constant, and the amount of gas in the studied volume. The relation is:

$$PV = nRT \tag{1.41}$$

where P is the pressure, V is the volume, n is the amount of gas (in moles), R is the ideal gas constant, and T is the temperature.

Since for the studied case it was assumed that the event happens under isothermal conditions, the right side of equation 1.41 becomes constant:

$$P_i V_i = P_f V_f \tag{1.42}$$

where the the subindexes i and f denotes initial and final values. This mathematical model is usually supplemented with an orifice-type equation to relate air pressure with discharge in presence of ventilation orifices.

1.4 Traditional solution methods for pressurized pipe model

In this section, two methods for solving the fully pressurized pipe model derived in section 1.2.1 are presented. The first one is the method of characteristics (also referred to as MOC), which consists in finding two ODEs for head flow rate that are valid along characteristic lines. The second one assumes certain simplifications which simplify the system of PDEs showed in equation 1.24 to a single ODE, making it easier to implement and compute, but with more restrict applicability.

1.4.1 Characteristics form of unsteady equations for closed pipes and its numerical solution

A popular way to model transient flows in water mains is the method of characteristics. Among the advantages of this method are the simple implementation and computational efficiency. The limitation is the fact that it assumes that the flow is homogeneous and single phase, which is not true for pipe filling problems.

The idea of the method is to apply a characteristic transformation on the mass and momentum equations for pressurized flows and integrate them. Therefore, the goal is to find a constant λ that renders the linear combination of the PDE system as an ODE system, as described below:

$$\begin{cases} \dfrac{\partial H}{\partial t} + \dfrac{a^2}{g}\dfrac{\partial u}{\partial x} + \dfrac{a^2}{g}\dfrac{q}{A} = L_1 \\ \dfrac{\partial u}{\partial t} + g\dfrac{\partial H}{\partial x} + f\dfrac{u|u|}{2D} = L_2 \end{cases} \tag{1.43}$$

$$L_2 + \lambda L_1 = 0 \tag{1.44}$$

or

$$\frac{\partial u}{\partial t} + g\frac{\partial H}{\partial x} + f\frac{u|u|}{2D} + \lambda\left(\frac{\partial H}{\partial t} + \frac{a^2}{g}\frac{\partial u}{\partial x} + \frac{a^2}{g}\frac{q}{A}\right) = 0 \tag{1.45}$$

As it can be seen in [Wylie and Streeter, 1993], the λ that satisfies equation 1.45 is:

$$\lambda = \pm\frac{g}{a} \tag{1.46}$$

Substituting λ in equations 1.44 by the expression in equation 1.46 and multiplying everything by A yields the following characteristic form of mass and momentum conservation equations:

$$\begin{cases} \dfrac{\partial Q}{\partial t} + A\dfrac{g}{a}\dfrac{\partial H}{\partial t} + f\dfrac{Q|Q|}{2DA} = 0 \\ \dfrac{dx}{dt} = a \\ \dfrac{\partial Q}{\partial t} - A\dfrac{g}{a}\dfrac{\partial H}{\partial t} + f\dfrac{Q|Q|}{2DA} = 0 \\ \dfrac{dx}{dt} = -a \end{cases} \tag{1.47}$$

The next step towards a numerical solution of equation 1.24 is to integrate this set of equations in order to find analytic expressions for both pairs of equations (positive and negative signs of a). The steps of the integration can be seen in [Wylie and Streeter, 1993] and result in:

$$\begin{cases} H_P = H_A - B(Q_P - Q_A) - R|Q_A|Q_P \\ H_P = H_B + B(Q_P - Q_B) + R|Q_B|Q_P \end{cases} \tag{1.48}$$

Some constants are defined in order to simplify the previous equations:

$$\begin{aligned} C_P &= H_{i-1}^{n-1} + BQ_{i-1}^{n-1} \\ C_M &= H_{i+1}^{n-1} - BQ_{i+1}^{n-1} \\ B_P &= B + R|Q_{i-1}^{n-1}| \\ B_M &= B + R|Q_{i+1}^{n-1}| \end{aligned} \tag{1.49}$$

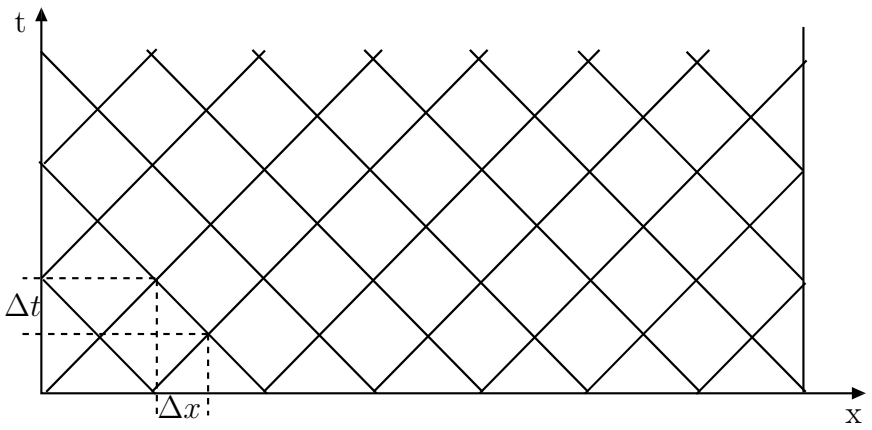

Figure 1.5: Example of a typical flow characteristic grid

With this, equations 1.48 turn to be:

$$\begin{cases} H_i = C_P - B_P Q_i \\ H_i = C_M + B_M Q_i \end{cases} \tag{1.50}$$

which are valid for the intersection between the characteristic lines, as in figure 1.5:

$$\frac{dx}{dt} = \pm a \tag{1.51}$$

Equations 1.50 are the final version of the numerical integration of characteristics form of mass and momentum equation. This form is the one present computational codes, such as Hammer [Bentley, 2010] and Pipe2011 [KYPipe, 2010].

1.4.2 Lumped Inertia

Lumped inertial model is a class of models with assumes that the whole water mass can be treated as a rigid column. This simplification is made in order to transform equations 1.24 into a single ordinary differential equation. The hypothesis for the lumped inertia approach are:

- The water phase is incompressible ($\frac{d\rho}{dt} = 0$);

- The pipe walls are perfectly rigid (this combined with the first hypothesis implies that $\frac{dH}{dx} = const$);

Considering those hypothesis, the calculation for the water phase can be reduced from a system of two PDEs (equation 1.24) into one ODE. Considering this control volume and applying the hypothesis' to equation 1.23 with localized head loses, it follows that:

$$g\frac{\partial H}{\partial x} + \frac{\partial u}{\partial t} + \left(f + K_{eq}\frac{D}{L}\right)\frac{u|u|}{2D} = 0 \tag{1.52}$$

Isolating $\frac{\partial u}{\partial t}$ yields:

$$\frac{\partial u}{\partial t} = -g\frac{\partial H}{\partial x} - f\frac{u|u|}{2D} - K_{eq}\frac{u^2}{2L} \tag{1.53}$$

Knowing that $\frac{dH}{dx}$ is constant over the pipe length (second hypothesis), the final form of the equation becomes:

$$\frac{\partial u}{\partial t} = -\frac{H - H_0}{L} - f\frac{u|u|}{2D} - K_{eq}\frac{u^2}{2L} \tag{1.54}$$

According to [Vasconcelos, 2007], this equation can be solved analytically, with the solution as follows:

$$u(t) = \sqrt{\frac{2g(H_u - H_d)}{R}}tanh\left(\frac{t}{2L}\sqrt{2g(H_u - H_d)R}\right) \tag{1.55}$$

in which $R = f\frac{L}{D} + 1$ and the subindexes u and d mean upstream and downstream. Another option is to solve the equation numerically for each point using Runge-Kutta or Forward Euler methods [Press, 1989].

[Martin, 1976], [Liou and Hunt, 1996], [Zhou et al., 2002a] and [Fuertes et al., 2000] applied lumped inertia models to mixed flows in pipes. Their models in addition to using the hypothesis of the lumped inertia, assumed that the contact interface between air and water

is well-defined and perpendicular to the pipe walls. This second hypothesis is illustrated in figure 1.6.

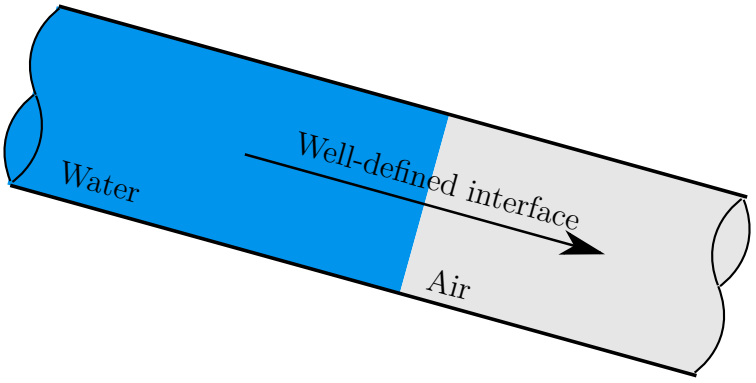

Figure 1.6: Control volume for lumped inertia models. Adapted from [Zhou et al., 2002a]

Chapter 2

Literature Review

This section presents a summary of the current body of knowledge on flow regime transition modeling, two phase flows, and some numerical schemes. It starts by presenting interface-tracking and shock-capturing models for flow regime transition with perfect ventilation, followed later by studies in which the effect air alongside water flow is accounted for. This chapter complements the theoretical basis of the present work, showing more recent ideas that were applied in the model proposed in this dissertation, and similar alternatives that have been proposed along the past few decades.

2.1 Flow Regime Transition Modeling

Flow regime transition is a type of liquid flow in which there is the transition from free-surface to pressurized flow and vice-versa, so that the existence of both regimes need to be taken into account by the model. Some of the inherently difficulties with this problem are:

- No single set of equations is able to account for both regimes;
- Wave celerities may be up to three orders of magnitude different between two flow regimes;
- Difficulties on how to handle the interface between both regimes.

In this section, two different modeling approaches for handling flow regime transition are presented. One is the *interface tracking approach*, which tracks the position of the interface between both phases and divides the flow into two different domains (pressurized

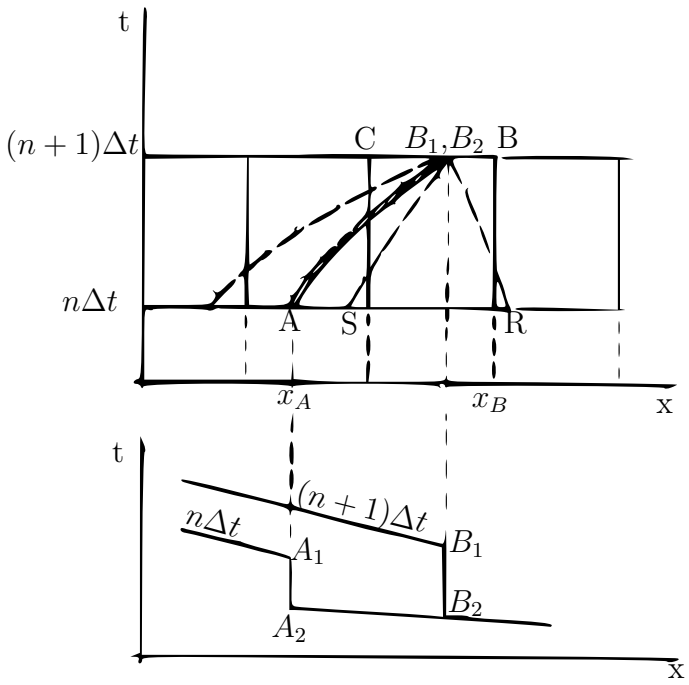

Figure 2.1: Scheme of shock fitting for free-surface flows presented in [Cunge et al., 1980]

and the free-surface). The other approach is the *shock-capturing*, which uses a single set of equations to calculate both portions by introducint a conceptual model, eliminating the need of tracking the interface position.

2.1.1 Interface-tracking Models

Basic concept of Shock-Fitting

A general concept behind interface-tracking is the Shock-Fitting technique, described in [Cunge et al., 1980]. In this approach, a discontinuity in the solution in the form of a hydraulic jump or a pipe-filling front (pressurizing bore) is tracked explicitly over time. This tracking represent the calculation of the discontinuity position and velocity and other relevant flow variables. Those variables are both depths and discharges (up and downstream), the position and the velocity of the discontinuity. In the shock fitting method presented in [Cunge et al., 1980] for river flow, the bore motion is solved by means of the Method of Characteristics applied to the Saint-Venant equations, as presented in figure 2.1.

Therefore, the system of equations to solve the flow in both sides of the discontinuity are the characteristic equations for both sides of the discontinuity. The usage of the method of characteristics adds three more unknowns for the problem, which are the origin points of the characteristic lines upstream and downstream the bore, as shown in figure 2.1. Note that the supercritical side provides only one characteristic line. Also, mass and momentum equations across the bore are necessary to solve the problem.

Hence, according to [Cunge et al., 1980], the four characteristic equations for the subcritical (downstream) side are:

$$x_{B_2} - x_S = (t_{B_2} - t_L)\left(\frac{(Q/A)_{B_2} + c_{B_2}}{2} + \frac{(Q/A)_S + c_S}{2}\right) \tag{2.1}$$

$$(Q/A)_{B_2} + 2c_{B_2} = (Q/A)_S + 2c_S + g(t_{B_2} - t_S)\left(\frac{S_{0B_2} + S_{fB_2}}{2} + \frac{S_{0S} + S_{fS}}{2}\right) \tag{2.2}$$

$$x_{B_2} - x_R = (t_{B_2} - t_R)\left(\frac{(Q/A)_{B_2} - c_{B_2}}{2} + \frac{(Q/A)_R - c_R}{2}\right) \tag{2.3}$$

$$(Q/A)_{B_2} - 2c_{B_2} = (Q/A)_R - 2c_R + g(t_{B_2} - t_L)\left(\frac{S_{0B_2} + S_{fB_2}}{2} + \frac{S_{0R} + S_{fR}}{2}\right) \tag{2.4}$$

where the subindexes represent the positions in figure 2.1.

Also, according to [Cunge et al., 1980], the characteristic equations for the supercritical side (upstream) are:

$$x_{B_1} - x_L = (t_{B_1} - t_L)\left(\frac{(Q/A)_{B_1} + c_{B_1}}{2} + \frac{(Q/A)_L + c_L}{2}\right) \tag{2.5}$$

$$(Q/A)_{B_1} + 2c_{B_1} = (Q/A)_L + 2c_L + g(t_{B_1} - t_L)\left(\frac{S_{0B_1} + S_{fB_1}}{2} + \frac{S_{0L} + S_{fL}}{2}\right) \tag{2.6}$$

Another two equations are the ones required to find the velocity of the shock.

$$S = \frac{A_{B1}(u_{B1} - u_{B2})}{A_{B1} - A_{B2}} + u_{B2} \tag{2.7}$$

$$u_{B1} - u_{B2} = \pm\left[g\frac{A_{B1} - A_{B2}}{A_{B1}A_{B2}}(A_{B1}h_{cB1} - A_{B2}h_{cB2})\right] \tag{2.8}$$

The last equations and also the simplest one, it the differential expression of the bore front velocity:

$$\frac{dx}{dt} = S \tag{2.9}$$

Also, according to figure 2.1, $x_{B1} = x_{B2} = x_B$ The system behind the track of bores has nine equations (equations 2.1 to 2.9) for nine unknowns (x_L, x_S, x_R, x, S, Q_A, A_A, Q_B and A_B). It is also important to notice, as shown in figure 2.1, that the interface between the two regimes (the bore) is considered to be perfectly defined and vertical.

Models based on Shock-Fitting theory

This idea of applying shock fitting to simulate flow regime transitions was first used by [Wiggert, 1972]. This model solves the free surface flow using the method of characteristics (similar to the development in 1.4.1) for equation 1.34 and calculates the front parameters as presented above. On the other hand, a lumped inertia approach as the discussed in subsection 1.4.2 for the pressurized portion of the flow was used. To validate the model, it was used a relatively long channel (30 meters long) with rectangular cross-section and an intermediate portion partially covered forming a rectangular pipe, having a still water level as initial

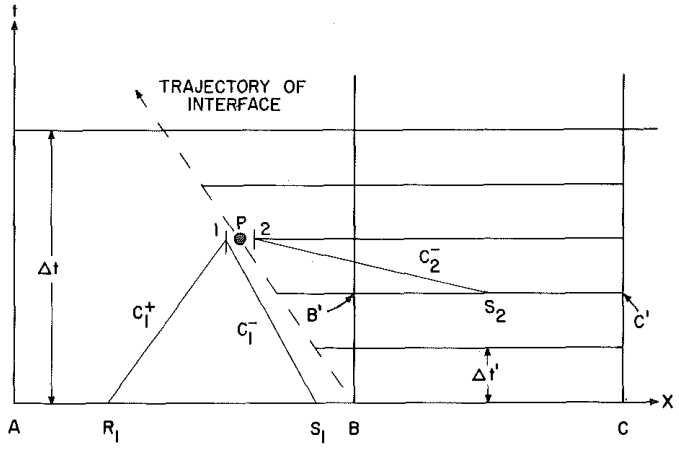

Figure 2.2: Characteristic grid x-t near the flow regime transition. Adapted from [Song et al., 1983]

conditon. As boundary conditions the apparatus had a downstream weir, and a upstream reservoir with a gate which would be opened to generate a flow that would pressurize the channel. The inflow front attained its maximum speed in a short amount of time after the gate opening, decelerating later along the channel and then slowly reaccelerating again when close to the weir and becoming steeper along the whole path. The main goal of those experiments was to calibrate and validate the proposed model.

[Song et al., 1983] proposed a model that would use the method of characteristics also for both portions of the flow. The practical problem of this alternative is the discrepancy of the time steps between both portions. In order to overcome this problem, the model calculates several time steps of the pressurized portion for each time step of the free surface portion. The resulting characteristic grid for the vicinity of the bore would be as show in figure 2.2. Other examples of models that use MOC are [Fuamba, 2002], [Gómez and Achiaga, 2001].

Even though those models can simulate relatively complex interactions between the free surface flow and the pressurizing bore, they have certain limitations. One of them comes from the MOC for the free surface flow, which incurs in a inability to simulate non-pressurizing bores, which are common in practical applications. Another limitation is the handling of the interface between free surface and pressurized flow, which is considered to be always

in the form of a bore. The model presented by [Politano et al., 2007] addressed the last limitation allowing gradual flow regime transition, calculating mass and momentum balance for a control volume comprising the last pressurized and the first free-surface nodes.

A model that partially overcomes some of those limitations is presented in [León et al., 2008]. The authors used the finite volume non-linear scheme (Riemann solver) HLL to a circular geometry developed in [León et al., 2006] in order to solve the Saint-Venant equations for the free surface portion of the flow in a shock capturing fashion, which makes the predictions of non pressurizing bores very precise without needing to track them (figure 2.3c). For the pressurized portion of the flow a compressible water hammer formulation which is able to handle distributed cavitation was used, which is also solved with the HLL solver. The model agrees well with experimental data for systems with small ventilation, however, some of the inconveniences of the other shock-fitting approaches still persists. One of them is the complexity of the model, which in this case comes from the calculations of the air water interface and also from the variation of the HLL scheme that was used.

Also, a common difficulty for all the Shock-Fitting models is the tracking of multiple pressurizing fronts, which happens often in practical applications, and the interactions between them, and other flow features.

Other interface tracking models

The interface-tracking model present in [Liou and Hunt, 1996] proposes a solution for the flow regime transition problem in a water main filling event without going through the complexity of the shock-fitting theory. This model use the lumped inertia approach assuming a vertical interface between air and water and a very rapid flow so that as the water reaches a pipe cross-section this cross-section goes instantaneously from wet bed to fully pressurized without the occurrence of a free-surface flow, which makes this model not to be formally a flow regime transition model, but still dealing with flow regime transition problems. This model solves equation 1.54 for each pipe, as shown in figure 2.4 with a Runge-Kutta method

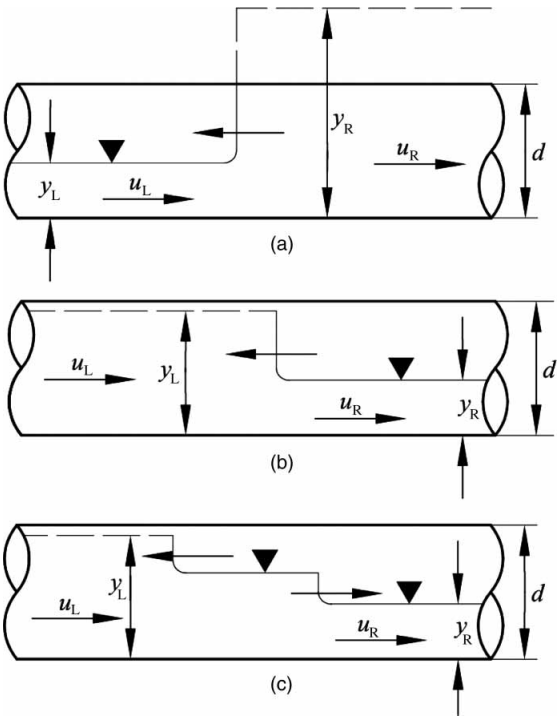

Figure 2.3: Bores in the model by [León et al., 2010]

with adaptive step size, showed in [Press, 1989]. One important limitation of the model is that air intrusion is not considered, otherwise free-surface flow would occur and the lumped inertia hypothesis become invalid. The model was used to simulate the filling of a theoretical water main with variable slope and of a laboratory experimental apparatus, which had good agreement with the model. Also, the experimental data was used to validate the model only at the early stages of the flow, when the velocity of the front is still very high, not representative of the typical velocities at the rest of the event.

Another lumped inertia model was proposed by [Li and McCorquodale, 1999]. This model considers the water portion of each flow regime as a rigid column, calculated with the lumped inertia approach, as seen in figure 2.5. The two rigid columns (pressurized and free-surface) are simulated with data from the moving bore by using the following continuity and momentum relations:

$$(V_1 + V_{bore})\, A_1 = (V_2 + V_{bore})\, A_2 \tag{2.10}$$

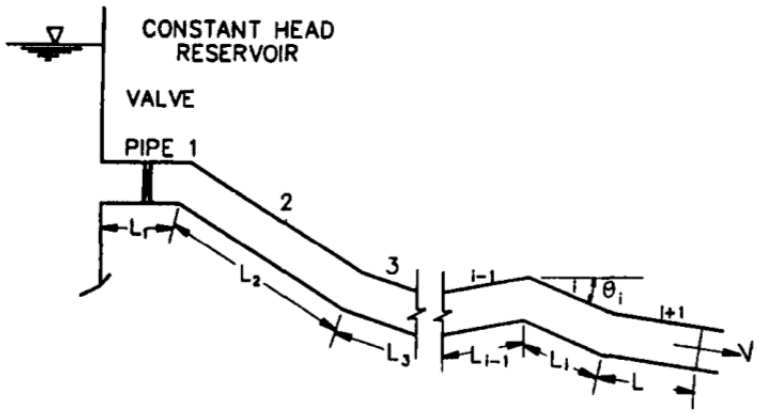

Figure 2.4: Model conceptualization. Adapted from [Liou and Hunt, 1996]

and

$$\gamma_w(y_1A_1) + pA_2 - (\gamma_w y_2 A_2 + \gamma_w Z A_2) = \rho_w A_1(V_1 + V_{bore})(V_2 - V_1) \tag{2.11}$$

where γ_w is the specific weight of water and Z is the pressure head on the surcharge side of the hydraulic jump. Air effects are also considered in this model as it will be explained later, as this approach have similarities with the model proposed in this work.

[Malekpour et al., 2011] simulated the rapid filling of water mains with the method of Characteristics for a full dynamic model showing good agreement with experimental data. However, the applicability of the approach is limited considering that the rapid filling of water mains is not desired this may damage the pipe.

As it was shown, currently there are different options of interface-tracking models for flow regime transition with varying degrees of complexity and able of simulating relevant flow features. However, this class of models still needs to overcome some limitations, such as the difficulty in simulating flows in more complex systems with several pressurizing bores and depression waves which may interact with each other. Another drawback of such models is the complexity of the calculations for the interface between free-surface and pressurized flows that exceeds the alternative provided by shock capturing models.

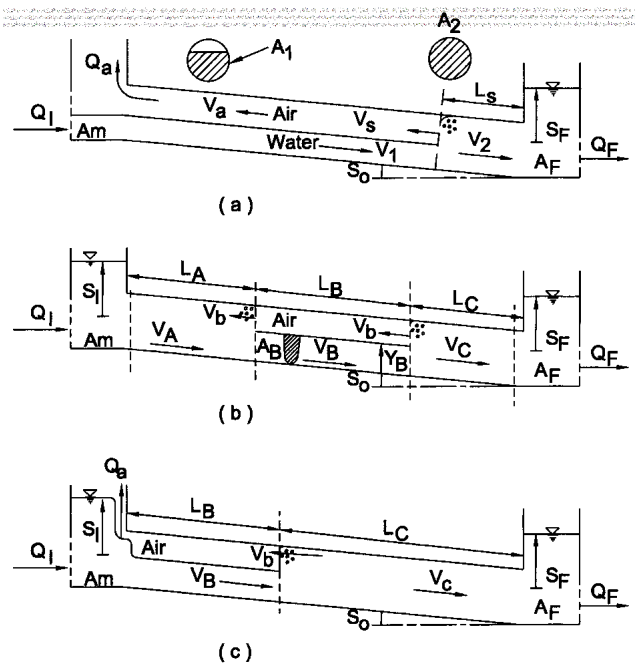

Figure 2.5: Model conceptualization. Adapted from [Li and McCorquodale, 1999]

2.1.2 Shock-Capturing models

Another family of flow regime transition models is called *shock-capturing*. The name is due to the fact that those models don't need to explicitly track a moving bore. This is accomplished by using a single set of equations and an appropriate choice of conserved variables (e.q. Q and A instead of y and u) for both flow regimes, which eliminates the need of changing the way the flow is calculated before upstream and downstream the pressurizing bore.

Preissmann Slot models

The first Shock-Capturing model handling flow regime transition was presented by [Cunge and Wegner, 1964] using an idea presented in [Preissmann, 1961] named the Preissmann Slot. This model assumes the existence of a fictitious slot on the crown of the pipe which simulates a pressurized flow as a free surface flow with the water filling the slot, as shown in figure 2.6, so that it can be calculated with the Saint-Venant equations (equation

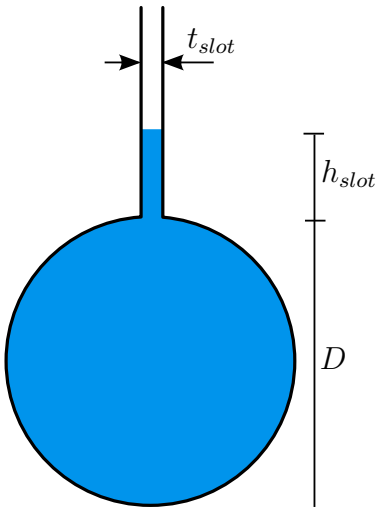

Figure 2.6: Preissmann slot representation

1.34). In figure 2.6 D represents the pipe diameter, t_f the width of the slot and h_{slot} the water level inside the slot (from the crown of the pipe until the surface).

The key of this strategy is to set two different ways to calculate the static momentum of the geometric cross-section ($A \cdot h_c$) in the Saint-Venant momentum equation, one for free-surface flow and the other for a pressurized flow. For the free-surface flow this static momentum for a circular cross-section is calculated using the formula shown in [Akan, 2006]:

$$\begin{cases} \dfrac{D^3}{24}[3sin(\theta) - sin^3(\theta) - 3\theta cos(\theta)] \\ \theta = \pi - arccos[(y - D/2)(D/2)] \end{cases} \tag{2.12}$$

where D is the pipe diameter, θ is the angle formed by free surface flow width and the pipe centerline, and y is the water level (which is smaller than D), while for the pressurized portion of the flow the static momentum is calculated by:

$$Ah_c = t_{slot}\frac{h_{slot}^2}{2} + \frac{\pi D^2}{4}\left(h_{slot} + \frac{D}{2}\right) \tag{2.13}$$

To consider the desired celerity of the pipe when a pressurized flow is present in the simulations the slot width must be properly chosen. For this, equation 2.14 is used:

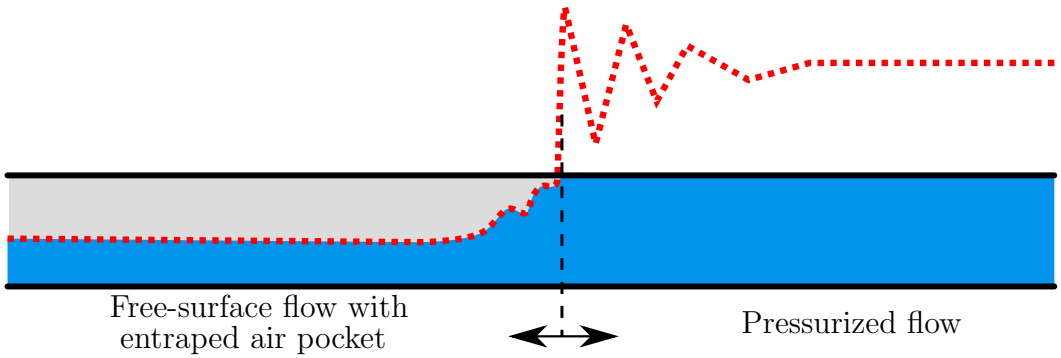

Figure 2.7: Post shock oscillations (red dotted line).

$$t_{slot} = \frac{gA_{pipe}^2}{a^2} \tag{2.14}$$

Because of the use of a single set of equations to solve both flow regimes, this model is significantly simpler than interface-tracking models. However, the Preissmann slot model has two disadvantages. The first one is shown in [Cunge and Wegner, 1964] and is about negative pressure flows. In the Preissmann slot model, if the pressure, which is seen as the water level, drops bellow the crown of the pipe for any portion inside the pressurized flow zone the free surface flow will be restored for this low pressure zone, which means an unrealistic assumption of perfect ventilation along the whole pipeline. The second limitation is regarding spurious post-shock oscillations, which will always happen in the pressurized portion of the flow right next to the pressurizing bore, as shown in figure 2.7.

Those oscillations can lead to peaks which are more than one order of magnitude higher than the actual pressure, distorting the results and making a computational code crash. These oscillations happen due to the difference in celerity between both portions of the flow, and are discussed in more details by [Vasconcelos et al., 2009a]. To overcome this limitation, a common strategy is to use an artificially low celerity values in between 50 to 200 m/s (as in [Trajkovic et al., 1999] and [Vasconcelos et al., 2006]) instead of using the real pipe celerity given by equation 1.9.

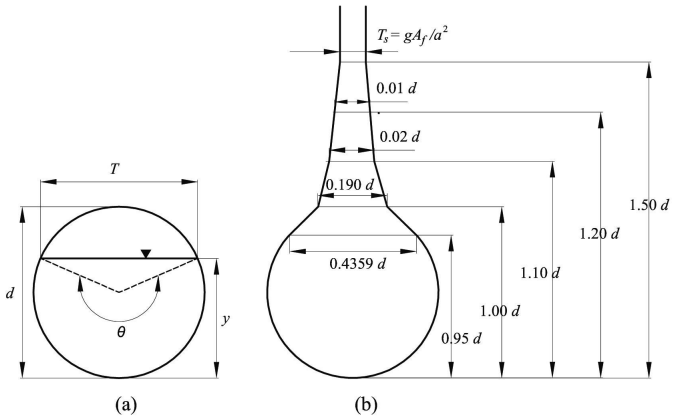

Figure 2.8: Modified Preissmann slot geometry. Extracted from [León et al., 2009]

However, when very low celerity are adopted (e.q less than 50 m/s) this can lead to other problems. When high pressures happen in the flow, significant continuity errors can happen due to the accumulation of water in the slot, which is not physical. With this, artificially low pressure peaks [Vasconcelos et al., 2006] and wave propagation velocity can be anticipated by the model.

In order to avoid the use of a low celerity for the whole pipe, [Sjöberg and CTH., 1982] proposed a modification in Preissmann slot model in which the width of the slot varies with the flow head and the pipe diameter according to equation 2.15, so that it would avoid a sudden transition between a low celerity to a high celerity in the moment the flow touches the crown of the pipe.

$$T_s = D\left(10^{-6} + 0.05423e^{-(h/D)^{24}}\right) \text{ when } h \geq 0.9999D \tag{2.15}$$

The model presented by [León et al., 2009] applied a similar idea but instead of using a equation such as equation 2.15 a criteria based on the head and diameter with linear approximation between each combination of head and a percentage of the diameter was used, as shown in figure 2.8.

Another improvement in the Preissmann slot was made by [Kerger et al., 2011]. This model considers a slot with negative depth for a pressure drop to a negative value in the pressurized portion of the flow instead of restoring a free-surface flow. However, this model still suffers from the limitation of the artificially low pipe celerity to avoid the post shock oscillations. Also, the hypothesis of the negative depth of the slot is not at first intuitive, making it difficult to understand its physical behavior and formulate other hypothesis for improvements in the model.

Other works which use the Preissmann slot model are [Capart et al., 1997], and [Trajkovic et al., 1999]. The latter performed experiments to calibrate and successfully validate the model with an apparatus consisting of a 10 m long pipe with 10 cm of inner diameter, eight ventilation pipes to eliminate the effects of air compression, a upstream reservoir two gates being one in the end and the other 1.5 m away from the tank. This experimental set up was adapted for the experiments performed in this dissertation. A detailed explanation about the Preissmann Slot can be found in [Cunge et al., 1980].

Two-component Pressure Approach (TPA)

In order to face the limitation of negative pressure of the Preissmann Slot model and the difficulty of handling a large number of pressurizing bores and their interactions with the shock-fitting models, [Vasconcelos et al., 2006] proposed the TPA model. This model makes use of the similarities between equations 1.24 and 1.34, with hypothesis on how the celerity is adjusted for both flow regimes add on a surcharge term enabling both coexisting flow regimes to be modeled with a single set of equations.

As shown in [Vasconcelos, 2005], assuming $sin\alpha \approx S_0$ and $\frac{f}{D}\frac{u|u|}{2g} = S_f$, equation 1.24 can be written with some manipulation as:

$$\begin{aligned} \frac{\partial A}{\partial t} + \frac{\partial Q}{\partial x} &= 0 \\ \frac{\partial Q}{\partial t} + \frac{\partial}{\partial x}\left(Q^2/A + gAh_c\right) &= gA(S_0 - S_f) \end{aligned} \tag{2.16}$$

If rewritten in quasi-linear form by adding ghA_x to both sides of the equation, the above equation becomes:

$$\begin{gathered}\mathbf{U}_t + \underset{\sim}{\mathcal{A}}\mathbf{U}_x = \mathbf{S} \\ \underset{\sim}{\mathcal{A}} = \begin{bmatrix} 0 & 1 \\ -\frac{Q^2}{A^2} + \frac{A}{\rho}\frac{\partial P}{\partial A} & 2\frac{Q}{A} \end{bmatrix}\end{gathered} \tag{2.17}$$

Equation 1.34 (Saint Venant equations) expressed in terms of total pressure and written in quasi-linear form yields exactly the same expression as equation 2.17. With this similarity observed, the only difference between both equations in the interpretation of the term $(A/\rho)(\partial p/\partial A)$. For open channel flows, this term is described as the square of celerity, as shown in equation 2.18

$$\begin{aligned} A(h) &= \int_0^h T_s(y)dy \\ \partial A(h) &= T_s(h)\partial h \text{ , and couped with } \partial p = \rho g \partial h \\ \frac{A}{\rho}\frac{\partial p}{\partial A} &= g\frac{A(h)}{T_s(h)} = c^2 \end{aligned} \tag{2.18}$$

where c is the flow celerity, y is the depth for the integration and h is the actual flow depth.

For a incompressible pressurized flow, assuming a elastic behavior for the pipe walls, $(A/\rho)(\partial P/\partial A)$ represents the acoustic wave speed, which is the equivalent of the celerity of the free surface flow for pressurized flows. With this, one has:

$$\frac{A}{\rho}\frac{\partial P}{\partial A} = c^2 = a^2 = \frac{\frac{\Delta P}{\rho}}{\frac{\Delta A}{A} + \frac{\Delta \rho}{\rho}} \text{ with } \Delta\rho = 0 \quad \rightarrow \quad a^2 = \frac{A}{\rho}\frac{\Delta P}{\Delta A} \tag{2.19}$$

Considering that $\Delta P = \rho g \Delta h$ as this ΔP is the extra pressure due to the flow pressurization, equation 2.19 can be modified so that it yields:

$$h_s = \frac{a^2}{g}\frac{\Delta A}{A_{pipe}} \tag{2.20}$$

where h_s is the extra head due to the pressurization and ΔA is the flow area the exceeded the original cross-section area of the pipe, making this original cross-section stretched or contracted. This term is then inserted in the Saint-Venant equations (equation 1.34) as a head that is added to the free-surface head which goes beyond the centroid of the cross-section in pressurized flows (h_c). This yields the final format of the Saint Venant equations modified by the TPA model:

$$\mathbf{U} = \begin{bmatrix} A \\ Q \end{bmatrix}, \ \mathbf{F}(\mathbf{U}) = \begin{bmatrix} Q \\ \frac{Q^2}{A} + gA(h_c + h_s) \end{bmatrix}, \ \mathbf{S}(\mathbf{U}) = \begin{bmatrix} 0 \\ gA(S_0 - S_f) \end{bmatrix} \tag{2.21}$$

$$h_s = \begin{cases} 0 & \rightarrow \text{free-surface flow} \\ \dfrac{a^2}{g}\dfrac{\Delta A}{A_{pipe}} & \rightarrow \text{pressurized flow} \end{cases} \tag{2.22}$$

$$h_c = \begin{cases} \dfrac{D}{3}\dfrac{3sin(\theta) - sin^3(\theta) - 3\theta cos(\theta)}{2\theta - sin(2\theta)} & \rightarrow \text{free-surface flow} \\ \text{where } \theta = \pi - arccos[(y - D/2)(D/2)] & \\ \dfrac{D}{2} & \rightarrow \text{pressurized flow} \end{cases} \tag{2.23}$$

where $\theta = \pi - arccos[(y - D/2)(D/2)]$. In the case where the flow is pressurized and the pressure is negative ΔA in equation 2.21 becomes negative instead of regenerating the free-surface flow. This gives a negative value of h_s. Equation 2.21 is also reached if a surcharge pressure is considered in the derivation of equation 1.34. Unlike Preissmann slot, h_c is limited by the value $D/2$.

With this, the TPA model overcame the inability of the conventional Preissmann slot model to simulate pressurized flows with negative pressure. Since its introduction, other shock-capturing models have also overcome the limitation of the traditional Preissmann slot model. A work by [Bourdarias and Gerbi, 2007] describes a model which is very similar

to the TPA. However, as described in [Vasconcelos et al., 2009a], all those models shock-capturing models based on the Saint-Venant equations still suffer from the limitation of the occurrence of post-shock oscillations, leading to errors due to a artificially low celerity as described for the Preissmann slot models. Alternatives to mitigate those oscillations based on numerical filtering and a new flux function called hybrid flux are described in [Vasconcelos et al., 2009a].

2.2 Two-phase flow studies

Air in water mains and slug flows are a concern for engineers that has been studied both numerically and experimentally by several researchers. Air in water mains is characterized by entrapped air, normally during the filling process, which engineers want to eliminate by means of air valves, drag forces caused by water, among others. Another related subject, according to [Fabre and Liné, 1992], are slug flows, which are a flow pattern with sequences of long air pockets almost filling the pipe, followed by liquid slugs which may contain small bubbles. Those flows are observed in systems with steady injections of liquid/gas phase and occur for a range of flow rates in gas/water flows, as described in [Falvey, 1980]. An important difference between slug flows and problems on air present in water main is that in the slug flow the gas portion of the flow is forced into the conduits and are transported along the pipe with the liquid phase, such as in oil/natural gas pipelines. With water mains, air is initially present and is gradually expelled by means of filling. Regarding the numerical approach to solve each case, a feasible way of trying to model the problem of air and water flow in pipes is by coupling flow regime transition models presented in the last section with air phase models whereas for slug flow a statistical approach is one alternative to describe flow characteristics on both phases.

As presented in this subsection, several researchers have conducted experiments about entrapped air in water flows. While some of those experiment were performed with experimental focus, several others were performed to assess the application and/or calibrate

numerical models. Many of those works about entrapped air were done focusing on the dragging of air pockets and bubbles. However, since this work focus on ventilation of air pockets those other works will not be detailed here.

2.2.1 Numerical models and experiments considering the effects of entrapped air in closed conduits

Studies about entrapped air in water pipe lines started as early as [Kalinske and Bliss, 1943], when the authors performed experiments on dragging of air pockets by air flows and developed equation 2.24 to determine the air flow rate given a water flow rate based on the experimental data. The proposed expression is valid as long as the water flow rate is high enough drag forces remove the air, even when buoyancy forces oppose the air motion. The work presented [Pothof and Clemens, 2010] and [Pozos et al., 2010] tackled the same problem, presenting expressions that relate air discharge to water discharge obtained by correlation of experimental data and conservation laws.

$$\left(\frac{Q_a}{Q_w}\right)_{max} = 0.0066(Fr-1)^{1.4} \tag{2.24}$$

Until the beginning of the last decade, most one-dimensional two-phase flow models were of the interface-tracking type. Possibly, the first such work was [Martin, 1976], which presented a lumped inertia model, assuming a well defined interface between air and water that advances over the dry portion of the pipe expelling the air through a orifice modeled with a simple head discharge relation. However, the well defined interface hypothesis is unrealistic for water main filling events.

An important technical report presented by [Falvey, 1980] has a chapter focusing on air-water interactions in closed pipe flows. In the first section on pipe flows, a comprehensive compilation of previous works is presented, including results, charts, and design criteria for air valves. An air-water flow classification is presented in terms of the air/water interaction pattern (small bubbles, big pockets, etc) based on the relative flow rates of both phases. After

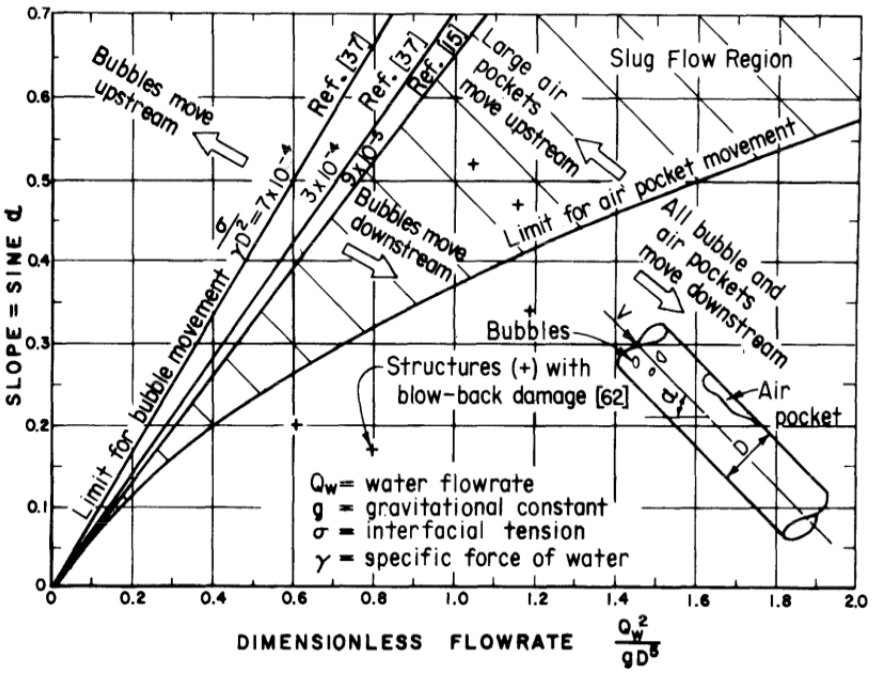

Figure 2.9: Bubble and air pockets motion in closed pipe flows. Extracted from [Falvey, 1980]

presenting air/water flow classification, a discussion is presented on flows in partially filled conduits, which is basically an open channel flow inside a pipe with a moving air layer on the top. The focus of that section is to present several models that try to predict the amount of air that would be transported along the pipe from upstream driven by the drag forces in between the two phases. The third section of that chapter presents a discussion about flows having a hydraulic jump that fills the conduit, which includes a review on several works that established empirical relations for the air pockets and bubbles drag, such as [Kalinske and Bliss, 1943] and [WISNER and Bucarest, 1967]. A chart presents the conditions anticipated for air pockets and bubbles to be dragged (hydraulic removal of air) according to pipe geometric characteristics and water flow rate. Air ventilation in conduits is also discussed in the report, with suggested criteria for location of ventilations valves, precautions against freeze, cavitation, and harm to personal in the vicinity. In the sixth and seventh sections, design criteria for the ventilation in pipelines and pump systems are presented, along with several types of ventilation valves, charts and head *vs*. discharge relations are presented.

The work presented by [Hamam and McCorquodale, 1982] aimed to study mechanisms for air pocket formation using a apparatus with rectangular and circular cross-section pipes. The studied mechanism was the formation of waves in the water surface caused by the relative air-water motion that eventually touch the crown of the pipe. This requires a certain amount of shear stress between air and water, which was accomplished by blocking downstream the free surface flow in the pipe. This blockage creates a pressurizing bore that the air ahead of it with a velocity in the opposite direction of the water flow, creating a high relative velocity between phases. With their results they concluded that the flow regime transition associated with those pockets can cause significant pressure peaks associated with the air expelling. The model presented in [McCorquodale and Hamam, 1983] is based in the lumped inertia approach for the water phase a simple compressible flow theory for the air phase. The model presented in [Li and McCorquodale, 1999] is a refinement of [Hamam and McCorquodale, 1982] in the sense that the first one considers the movement of the air pockets.

A similar model was presented in [Zhou et al., 2002a], in the sense that this model also used a lumped inertia approach with a moving, well defined vertical interface which expels the air ahead of it. A difference from the model presented in [Martin, 1976] is the orifice formulation, which considers a chocked orifice. The focus of this work was to measure maximum surges under different inflow/ventilation configurations. The model was compared to experimental results which showed good agreement except for the oscillation pattern for substantial air release. Regarding the experimental part, the apparatus consisted of a reservoir linked to a horizontal pipe with a control valve separating the initially filled and empty portions of the pipe; and interchangeable nozzles with different diameters providing ventilation on the other end of the pipe. Three typical outcomes were noticed: negligible water hammer effect, in which the air pocket "absorbs" the water hammer effect; mitigated water hammer effect, in which a the water hammer effect is again absorbed but a high pressure peak is observed and the end of the filling event when the water hits the ventilation

orifice; and water hammer dominant, in which the air content is rapidly expelled and the water slams the ventilation orifice generating a pressure peak almost four times higher as the mitigated one. They found that the ratio between the ventilation orifice and pipe diameter is determinant to the intensity of the transient pressures and oscillations pattern. However, the very rapid filling nature of the experimental conditions as well as the extreme high pressures when compared to the pipe diameter do not represent actual water main filling conditions. [De Martino et al., 2008] also studied those pressure peaks due to the expel of air pockets through ventilation orifices in a purely experimental fashion, deriving an expression for the maximum expected pressure peak. Other models dealing with lumped inertia-type approach for water phase are [Kabiri Samani et al., 2006] and [Izquierdo et al., 1999], this last one proposing a model for the filling of whole sloping water pipe lines with air pockets. The model was tested with experimental data in [Fuertes et al., 2000] in order to validate the model again under extreme conditions.

[Chaiko and Brinckman, 2002] presented a comparative study of three models to simulate air/water interactions in a pipe filling problem. The first model presented was a full dynamic approach with both phases being solved by the method of characteristics, so that water characteristic lines need to be interpolated to match the grid; the second was the same full dynamic for water and lumped for air; and the third applied lumped inertia approach for air MOC for water phase, however calculating only the unperturbed portion of the water flow so that the characteristic lines have constant slope and match the grid without the need of interpolation. The author runs tests for a vertical set up which consisted of a a cylinder with a air pocket on the upper part which is compressed by the water phase due to a increase in the water pressure at the bottom of the cylinder. The authors showed that the second model (full dynamic for water and lumped for air) capture all the relevant events as well as the first model, even though the second didn't capture small oscillations due to the reflection of the pressure wave in the air, which has no practical importance. However, the problem that

was proposed by the authors is too idealized, given the experimental set up and given the well defined interface between phases.

[Zhou et al., 2011] developed a model based on the method characteristics for the water phase and a variation of the ideal gas law with a polytropic coefficient of 1.4 instead of 1.0 for the air phase, with simple mass and momentum conservations in the interface between phases for the interface tracking. Also, a series of experiments were performed to show the effect of small air pockets (0% to 8.02% of void fraction in the pipe) in the pressure peak and validate the model. The authors concluded that instead of having "the maximum peak pressure of air pocket increases with the decrease of the initial void fraction of air pocket" as it was stated in their previous works (such as [Zhou et al., 2002a]), the maximum peak happened for a void fraction of 6.18%.

A recent work with the interface-tracking approach is presented in [León et al., 2010] as a enhancement of the model proposed in [León et al., 2008]. The model presented in the work handles the water phase using the HLL Riemann solver for the Saint-Venant equations (free surface flow) and for the compressible water hammer formulation presented first in [Guinot, 2003] (pressurized flow). For the air phase the approach was the same presented in [Martin, 1976] and [Zhou et al., 2002a]. Two conditions were considered for the air phase: with and without air release. For both of them, the model matched well with the experimental data from [Vasconcelos et al., 2006] and [Zhou, 2000].

On the shock-capturing front, [Arai and Yamamoto, 2003] developed a model based on the Preissmann slot which assume the existence of a cap over the slot to avoid ventilation. A modified version of the Saint-Venant equations was used for the water phase as well as a structurally similar version of those equations were used for the air-phase. This particular set of equations was used in order to apply the four-point Preissmann implicit scheme presented in [Cunge et al., 1980] to solve the equations. In order to calibrate a model, their experimental studies were made with a scale model of an underground drainage system with 122.08 meters of pipe, being one of the longest reported in literature. With their experiments they showed

that the existence of entrapped air affects the time for the flow regime transition to happen, suppresses inertial oscillation, and rises the maximum observed pressure in the system, also increasing the pressure variation in the inlet. Their two-phase full dynamic flow model showed good agreement with the experimental data.

Another shock capturing model was developed by [Vasconcelos and Wright, 2009] as a enhancement of the TPA model presented in [Vasconcelos et al., 2006]. In this model, a term to account for air pressure is added to the momentum equation of the TPA model, changing the vector **F** in equation 2.21 for the one in equation 2.25.

$$\mathbf{F}(\mathbf{U}) = \begin{bmatrix} Q \\ \frac{Q^2}{A} + gA(h_c + h_s) + gA_{pipe}h_{air} \end{bmatrix} \tag{2.25}$$

where h_{air} is the term that accounts for the air pressure, making part of the link between both phases. While the air flow rate through the ventilation orifice is given by the expression presented in [Zhou et al., 2002a], the air head is calculated by the continuity of the air phase, which leads to the following expression:

$$h_{air} = \frac{1}{2g}\frac{\rho_a}{\rho_w}\left[\frac{u_S(A_{pipe} - A_{fs})}{C_d A_{orif} Y}\right] \tag{2.26}$$

where u_S is the velocity of the moving bore, A_{fs} is the area of the free-surface flow, and Y is an expansion factor showed in [Zhou et al., 2002a].

The work by [Tran, 2011] presented a lumped model for bubbly flows which accounts for the effects of liquid compressibility, pipe elasticity and temperature rise across a pressure wave. The author found that below a certain air content the effects of pipe elasticity and liquid compressibility are significant, while for a bubbly flow with a reasonably high amount of air (above 10% or 20%) the transient flow may be considered isothermal in part due to the high thermal capacity of water.

In [Fabre and Liné, 1992] the authors presented a model for slug flow. The problem of long pockets as well as small bubbles generated by slug flow is dealt with in a statistical fashion given the virtually random behavior and intermittency of the details of this type of flow. Also on slug flows, the model presented in [Issa and Kempf, 2003] is a shock-capturing technique coupled with a formulation that accounts for the Kelvin-Helmholtz instabilities which form a slug flow, as described in [Falvey, 1980]. However, the focus of this work was to only predict the frequency and the occurrence of slug flow due to the Kelvin-Helmholtz instabilities, not calculating the effects of the air pressure of the entrapped air in the slug flow. Since slug flows is outside the scope of this work, this subject will not be further discussed here.

2.3 Numerical schemes to solve hyperbolic PDEs

There are basically two types of numerical schemes for hyperbolic PDEs (such as Saint-Venant equations) solution, which are *linear* and the *non-linear* numerical schemes. The linear schemes, as the name indicates, use a linear combination of the previous time step values to calculate the fluxes of conserved variables, while the non-linear schemes are based on the Riemann problem.

Some linear schemes and its characteristics are [Toro, 2001]:

- Lax-Friedrichs (LxF): this first order accurate (takes into consideration until the second derivative in a Taylor expansion) scheme is easy to implement, fast to calculate, and stable, however it is notorious for the high amount of numerical diffusion in case of a discontinuity in the solution of the equations, such as in a supersonic air flow or a moving bore in a open channel flow. The algebraic expression for this scheme in finite volume is:

$$\begin{cases} \vec{F}_i^{n+1} = \dfrac{1}{2}[\vec{F}_{i-1}^{n} + \vec{F}_{i+1}^{n}] + \dfrac{1}{2}\dfrac{\Delta t}{\Delta x}(\vec{U}_{i+1}^{n} - \vec{U}_{i-1}^{n}) \\ \vec{U}_i^{n+1} = \dfrac{1}{2}[\vec{U}_{i+1}^{n} + \vec{U}_{i-1}^{n}] + \dfrac{1}{2}\dfrac{\Delta t}{\Delta x}(\vec{F}_{i-1}^{n} - \vec{F}_{i+1}^{n}) + \Delta t S_i^n \end{cases} \tag{2.27}$$

in which i is the node number, n is the time step number, $\vec{\mathbf{U}}$ is the vector of conserved variables and $\vec{\mathbf{F}}$ is the fluxes vector.

- Lax-Wendroff (LxW): this scheme has second order accuracy (depends on the two last time steps values) and is more complex to calculate than the Lax-Fridriechs scheme because of the second order precision, being still considerably fast to calculate and easy to implement. A problem with LxF is the occurrence of very strong spurious oscillations on the vicinity of discontinuities in the solution (bores), which may easily make the code crash by making the water depth goes negative. In order to overcome this problem some researchers make use of flux limiters such as the TVD methods (Total Variation Diminishing) to mitigate those oscillations, as shown in [Toro, 2001]. The algebraic expression for McCormack variation of the LxW scheme (without TVD) is divided into two steps, being the first the predictor and the second the corrector:

$$\begin{aligned} &\text{(Predictor step)} \begin{cases} \vec{F}_{i+\frac{1}{2}}^{n+\frac{1}{2}} = \frac{1}{2}[\vec{F}_{i+1}^{n} + \vec{F}_i^{n}] + \frac{1}{2}\frac{\Delta x}{\Delta t}(\vec{U}_i^{n} - \vec{U}_{i+1}^{n}) + \frac{1}{2}\Delta t S_i^n \\ \vec{U}_{i+\frac{1}{2}}^{n+\frac{1}{2}} = \frac{1}{2}[\vec{U}_{i+1}^{n} + \vec{U}_i^{n}] + \frac{1}{2}\frac{\Delta t}{\Delta x}(\vec{F}_i^{n} - \vec{F}_{i+1}^{n}) + \frac{1}{2}\Delta t S_i^n \end{cases} \\ &\text{(Corrector step)} \begin{cases} \vec{F}_i^{n+1} = \vec{F}_i^{n} + \frac{\Delta t}{\Delta x}(\vec{F}_{i+\frac{1}{2}}^{n+\frac{1}{2}} - \vec{F}_{i-\frac{1}{2}}^{n+\frac{1}{2}}) \\ \vec{U}_i^{n+1} = \vec{U}_{i+1/2}^{n} + \frac{\Delta t}{\Delta x}(\vec{F}_i^{n+1} - \vec{F}_{i+1}^{n+1}) + \Delta t S_i^n \end{cases} \end{aligned} \tag{2.28}$$

- FORCE: This is a hybrid scheme which, in its original form, is calculate by averaging the fluxes of Lax-Friedrichs and Lax-Wendroff:

$$F_{i+\frac{1}{2}}^{FORCE} = (1+\theta)\frac{1}{2}(F^{LxF} + \theta F_{i+\frac{1}{2}}^{LxW}) \tag{2.29}$$

with $\theta = 0.5$. This scheme is less diffuse than Lax-Friedrichs and presents no oscillations, however it demands a high computing effort when compared to the other two alternatives due to the fact that it calculates both Lax-Friedrichs and Lax-Wendroff for then calculate the actual fluxes.

For linear schemes as the ones presented, the degree of numerical diffusion and spurious oscillations in the results, as well as the stability, are controlled by a non-dimansional parameter named the Courant number, defined by equation 2.30 [Sturm, 2001]. This condition related the propagation velocity of a flow feature predicted by a numerical scheme with the discretization-based velocity $\Delta x/\Delta t$. Explicit schemes require a Courant number below the unity for stability.

$$Cr = \frac{|u| + c}{\Delta x/\Delta t} \tag{2.30}$$

where Cr is the Courant number. The open channel celerity c is substituted by the acoustic wave speed a a pipe flow and by the sound speed the the gas for a gas flow.

According to [Godunov, 1959], the Godunov's theorem states that when Courant number is below unity, linear schemes results present either numerical diffusion (first order schemes) or oscillations (higher order schemes) at the vicinity of bores. Those problems are worsened as the Courant number becomes smaller then unity, rendering the use of those linear schemes particularly problematic for problems containing several discontinuities, where part of the flow have a lower Courant number smaller than unity, considering that $Cr \leq 1$ must be enforced in the whole solution domain.

In the model proposed in this dissertation, the air and both free-surface and pressurized water flows must be calculated together for every time step, which creates the necessity of using the same time step for both the phases. This may lead to a low Courant number for the free surface water flow because the air speed of sound and the acoustic wave speed in pressurized flows can be two three orders of magnitude higher than the open channel

celerity c. As mentioned, Godunov's theorem states that the air flow would suffer from very high diffusivity or very high spurious oscillations (sometimes even with a TVD method implemented) at the vicinity of bores/shocks if calculated with a linear scheme, however shocks are not anticipated in air flows in this work.

In order to overcome the anticipated limitations of linear schemes in the simulation of hyperbolic partial differential equations, non-linear schemes were developed. The first one was by Godunov and solves the problem's discontinuities not by performing a linear combination, buy instead by solving exactly the initial value problem proposed by Riemann. This solution is generally iterative and time-consuming, which lead to the development of several other non-linear schemes performing an approximate solution for the Riemann problem with the objective to derive alternative expressions for Finite Volume fluxes across cell interfaces. Among such schemes one includes HLL [Harten et al., 1983], HLLC [Toro et al., 1994] and Roe's scheme [Roe, 1981].

Both Roe and HLL first order accurate schemes would be good options for implementation in the proposed model. The HLL scheme is generally simpler than Roe scheme, however its fluxes formulation is highly dependent on the flow cross-section geometry, which makes it cumbersome to be implemented for the case of a circular pipe. Since the cross-section geometry to be studied with in the present work is circular and Roe scheme does not depend on the cross-section geometry on the calculation of inter-cell fluxes, the implementation of Roe scheme suggested by [Macchione and Morelli, 2003] was adopted. The algebraic expressions for the update of the conserved variables vector $\vec{\mathbf{U}}$ (as in equation 2.21) is:

$$\begin{aligned} \vec{U}_i^{n+1} = \vec{U}_i^n - \frac{\tau}{2} \Bigg\{ \Bigg[(\vec{\mathbf{F}}_i^n + \vec{\mathbf{F}}_{i+1}^n) - \sum_j |\bar{\lambda}^j| (\delta w^{(j)})_{i+1/2} \bar{\mathbf{r}}_{i+1/2}^{(j)} \Bigg] \\ - \Bigg[(\vec{\mathbf{F}}_{i-1}^n + \vec{\mathbf{F}}_i^n) - \sum_j |\bar{\lambda}^j| (\delta w^{(j)})_{i-1/2} \bar{\mathbf{r}}_{i1/2}^{(j)} \Bigg] \Bigg\} + \Delta t \vec{\mathbf{S}}_i^n \end{aligned} \tag{2.31}$$

where $\tau = \Delta t / \Delta x$ and $\mathbf{F}$ is the fluxes vector. This equation was derived from the implementation of Roe scheme in a 1-D Finite Volume framework. Also as shown in [Macchione and

Morelli, 2003], for the Jacobian matrix right eigenvectors $\bar{\mathbf{r}}^{(j)}$ the following inter-cell flow averaged variables, named Roe averages, should be considered for each interface $(i, i+1)$ as:

$$\bar{A}_{i+1/2} = \sqrt{A_i A_{i+1}} \tag{2.32}$$

$$\bar{Q}_{i+1/2} = \frac{\sqrt{A_i}Q_{i+1} + \sqrt{A_{i+1}}Q_i}{\sqrt{A_i} + \sqrt{A_{i+1}}} \tag{2.33}$$

For the celerity the Roe average is:

$$\bar{c} = \sqrt{g\frac{I_{1i+1} - I_{1i}}{A_{i+1} - A_i}} \text{ when } A_{i+1} \neq A_i \tag{2.34}$$

$$\bar{c} = \sqrt{\frac{\frac{1}{2}g(A_{i+1} + A_i)}{\frac{1}{2}g(b_{i+1} + b_i)}} \text{ when } A_{i+1} = A_i \text{ or } (I_{1i+1} - I_{1i})(A_{i+1} - A_i) < 0 \tag{2.35}$$

so that the approximate eigenvalues matrix is characterized by the following eigenvalues and eigenvectors:

$$\begin{aligned} \text{eigenvalues: } \bar{\lambda}_1 &= \frac{\bar{Q}}{\bar{A}} + \bar{c} \\ \bar{\lambda}_2 &= \frac{\bar{Q}}{\bar{A}} - \bar{c} \end{aligned} \tag{2.36}$$

$$\begin{aligned} \text{eigenvectors: } \bar{\mathbf{r}}^{(1)} &= \frac{1}{2\bar{c}}[1, \bar{\lambda}_1]^T \\ \bar{\mathbf{r}}^{(2)} &= \frac{1}{2\bar{c}}[1, \bar{\lambda}_2]^T \end{aligned} \tag{2.37}$$

The variations $\delta w^{(1)(2)}$ (strength of the wave crossing the (i,i+1) interface) at the point $i + 1/2$ are expressed as follows:

$$\delta w^{(1)(2)} = \pm \left[(Q_{i+1} - Q_i) + \left(-\frac{\bar{Q}_{i+1/2}}{\bar{A}_{i+1/2}} \pm \bar{c}_{i+1/2} \right) (A_{i+1} - A_i) \right] \tag{2.38}$$

Chapter 3

Knowledge gap and objectives

The problem of the ventilation of entrapped air in water mains is a complex and relevant problem, which remains to date poorly understood. Many experimental investigations, such as [Falvey, 1980], [Benjamin, 1968], [Pothof and Clemens, 2010] and others, focused on selected features of this problem, but the current knowledge is still very limited especially with regards to numerical modeling attempts, as shown in the literature review. Therefore, more numerical research and experimental investigations on water flows with entrapped air pockets still need to be done in order to provide engineers with a more complete understanding of this phenomena.

The goal of this work is to obtain further insight on air-water interactions during water pipeline filling operations, with the overarching objective of developing a numerical model that may be used to simulate *a priori* filling operations in pipelines and detect operational issues related to the entrapment of air pockets.

To achieve this objective, a numerical model is proposed to simulate the filling of pipelines and it applies the TPA approach presented by [Vasconcelos and Wright, 2009] to describe the water phase. Air phase modeling is performed either by using a discretized framework that applies the Euler equation or by using a type of UAPH model. A secondary objective was to assess the benefits of using a discretized framework to simulate air phase.

An experimental investigation was also conducted using a scale model apparatus that includes the essential features of a water pipeline. Key parameters in the problem are systematically varied, including inflow rate, pipeline slope and ventilation degree. Experimental measurements included pressure, pressurization interface trajectories and inflow rates. Both

modeling alternatives for air phase were compared to experimental data and to the field data of an actual water main filling event presented by [Vasconcelos et al., 2009b].

Chapter 4

Methodology

This chapter describes the methodology used to accomplish the stated objectives. In order to create a model able to simulate air pressurization effects in water mains undergoing refilling operations, the model based on the TPA approach with air head described in [Vasconcelos and Wright, 2009] was coupled with two different approaches for the air phase calculation. This model aims to simulate water flows with air phase in pockets shrinking in volume due to the refilling, which means that they are not dragged and do not float. Only the strictly necessary boundary conditions (for both phases) were developed, which consists on the ones required by the assessment of the model, experimental program, and field conditions, in order to test the model.

A systematic experimental investigation was conducted for this work due to the limited published data about this problem. A set of field data about the filling process of a real water main in the city of Brasília - Brazil used for model validation. This process of validation required a calibration of the energy dissipation based on the Manning's n friction factor and on the contraction coefficient of the ventilation orifice due to the lack of information on those two parameters and to the fact that the authors needed to approximate the behavior of an actual air valve by a single orifice.

4.1 Numerical model

Certain flow features of the water main pipeline filling problem were determinant in the model's formulation so that it could describe the filling process adequately. With regards to the water phase, these features include:

- Flow regime transition: addressed by using a flow regime transition model [Vasconcelos and Wright, 2009];
- Post-shock oscillations at pipe-filling bore fronts: use of a numerical filtering scheme [Vasconcelos et al., 2009a];
- Air pocket entrapment and pressurization: used either Euler equation or uniform air pressure head (UAPH) model;
- Free-surface and pipe-filling bores: Use of the approximate Riemann solver presented by Roe [Macchione and Morelli, 2003];
- Dry water bed: assumed thin water layer (depth of 0.001 m) present in the whole dry portion of the pipe; and
- Solution stationarity: use approach presented by [Sanders et al., 2011].

Air phase in the model is represented by a well-defined air pocket that is not significantly fractured. This pockets shrinks due to compression by the water phase that gradually occupies the lowest points in the pipeline profile. Air is displaced and escapes through ventilation orifices located at selected locations. According to [Tran, 2011] for such flow conditions air compression process may be considered isothermal. This assumption is used in both models used to simulate air phase during the filling process.

The air phase is calculated as if the only outside connections (with atmosphere) occur at ventilation points, which are treated as orifices for simplicity. Ideal ventilation with negligible air phase pressure head is assumed to exist prior to the formation of an entrapped air pocket, as it will be discussed later. When a pocket forms, it is delimited by the ventilation orifice and a flow regime transition interface, either abrupt or gradual. In the proposed model, an air pocket is formed by the closure of a downstream valve or by the pressurization interface generated as water fills the lowest points of the pipeline, creating a pressurization interface.

Figure 4.2 presents a sketch of a typical application, whereas Figure 4.1 presents the overall structure of the proposed model.

4.1.1 Water phase modeling

The TPA model, used in the water phase simulation, modifies the Saint-Venant equations, enabling them to simulate both pressurized flows and free-surface flow regimes. This model has been improved in the past years and the alternative used here was presented in [Vasconcelos and Wright, 2009]. This alternative has a term that accounts for air phase pressure head, so that the modified St. Venant equations are, in divergence format:

$$(\mathbf{U})_t + \mathbf{F}_x(\mathbf{U}) = \mathbf{S}(\mathbf{U}) \tag{4.1}$$

where

$$\mathbf{U} = \begin{bmatrix} A \\ Q \end{bmatrix}, \ \mathbf{F}(\mathbf{U}) = \begin{bmatrix} Q \\ \frac{Q^2}{A} + gA(h_c + h_s) + gA_{pipe}h_{air} \end{bmatrix}, \ \mathbf{S}(\mathbf{U}) = \begin{bmatrix} 0 \\ gA(S_0 - S_f) \end{bmatrix} \tag{4.2}$$

$$h_{air} \begin{cases} = 0 \rightarrow \text{free-surface flow without entrapped air pocket / Pressurized flow} \\ \neq 0 \rightarrow \text{free-surface flow with entrapped air pocket} \end{cases} \tag{4.3}$$

$$h_s = \begin{cases} 0 & \rightarrow \text{free-surface flow} \\ \dfrac{a^2}{g}\dfrac{\Delta A}{A_{pipe}} & \rightarrow \text{pressurized flow} \end{cases} \tag{4.4}$$

$$h_c = \begin{cases} \dfrac{D}{3}\dfrac{3sin(\theta) - sin^3(\theta) - 3\theta cos(\theta)}{2\theta - sin(2\theta)} & \rightarrow \text{free-surface flow} \\ \text{where } \theta = \pi - arccos[(y - D/2)(D/2)] & \\ \dfrac{D}{2} & \rightarrow \text{pressurized flow} \end{cases} \tag{4.5}$$

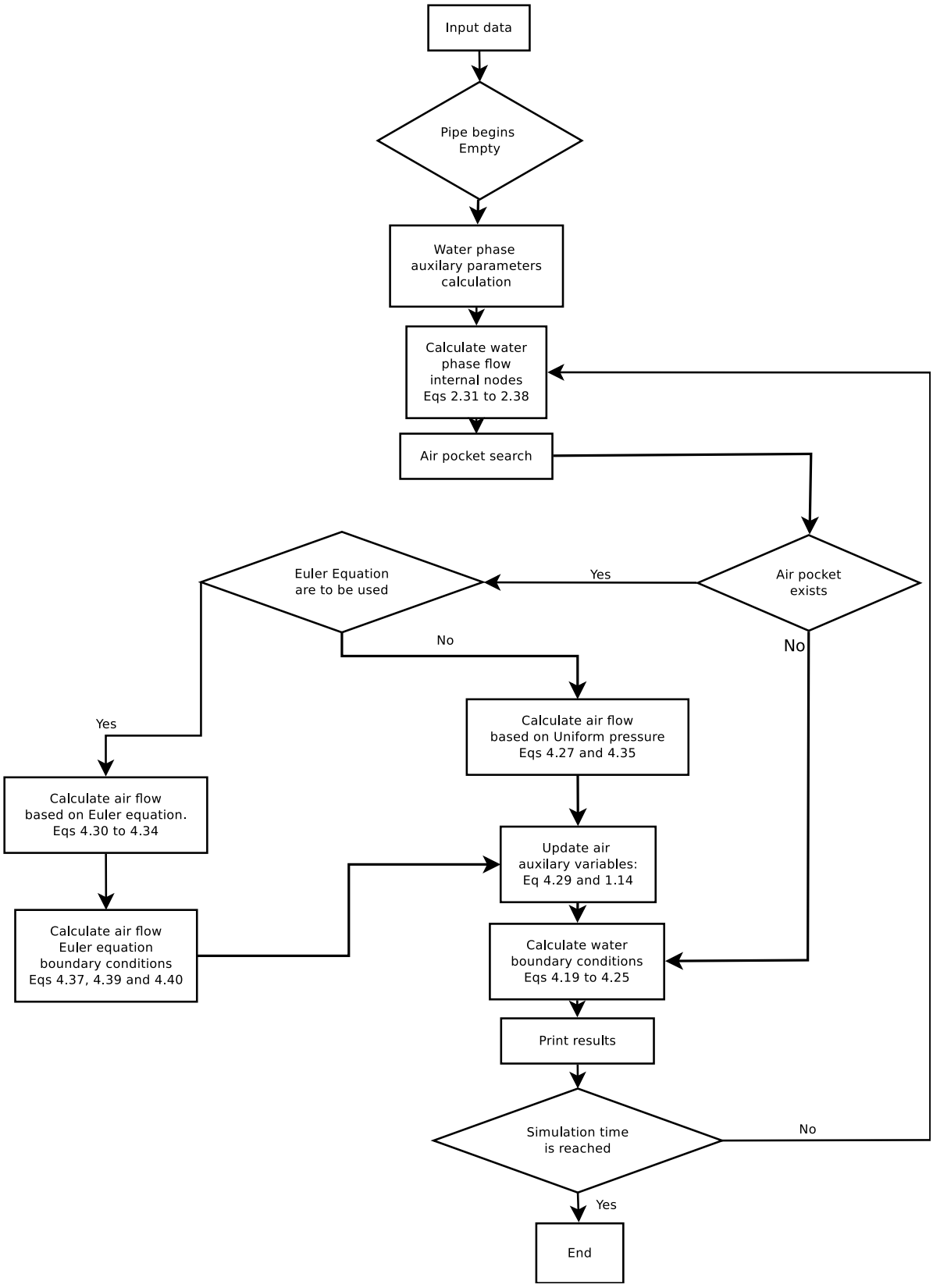

Figure 4.1: Flow chart for the model calculation procedures

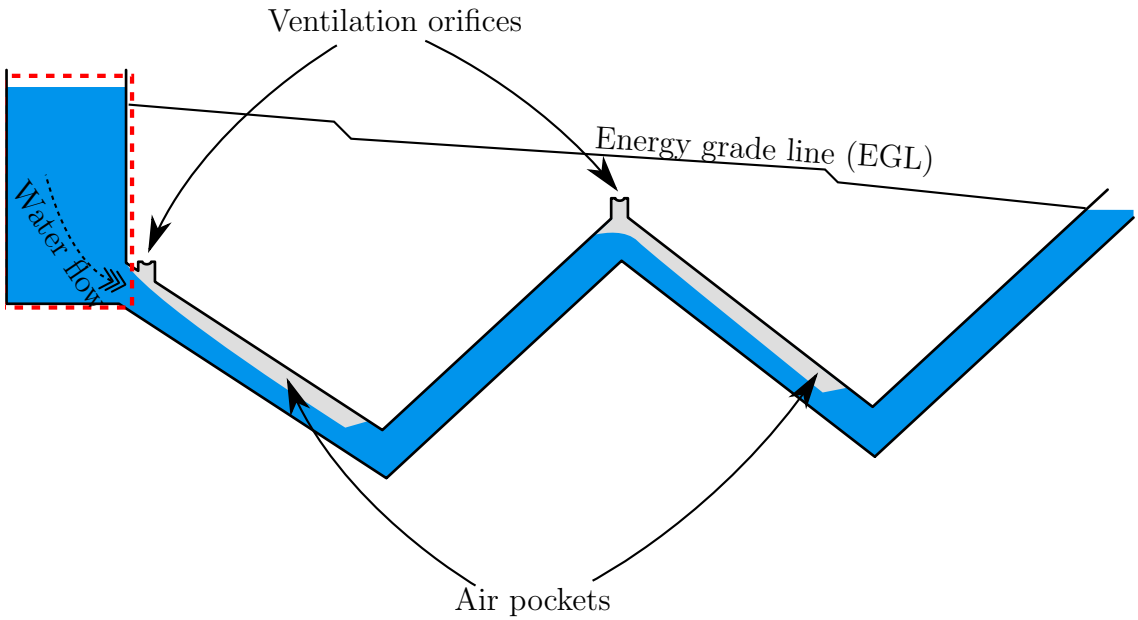

Figure 4.2: Model physical scheme

where $\mathbf{U} = [A, Q]^T$ is the vector of the conserved variables, A is the flow cross sectional area, Q is the flow rate, $\mathbf{F}(\mathbf{U})$ is the vector with the flux of conserved variables, g is the acceleration of gravity, h_c is the distance between the free surface and the centroid of the flow cross section (limited to $D/2$), h_s is the surcharge head, h_{air} is the extra head due to entrapped air pocket pressurization, θ is the angle formed by free surface flow width and the pipe centerline, D is the pipeline diameter, and a is the celerity the acoustic waves in the pressurized flow.

The numerical scheme used in the implementation of the water phase model used the Finite Volume Method and the approximate Riemann solver of Roe, as presented in [Macchione and Morelli, 2003]. This choice was motivated by the significant discrepancy in the celerity values between the free-surface and pressurized flows, and between air and water flows. This discrepancy may be in the order of 2 or 3 orders of magnitude and yields an extremely low Courant number for the free-surface water flow, as shown in figure 4.3 and equation 4.6.

$$Cr = \frac{|u| + c}{\Delta x / \Delta t} \tag{4.6}$$

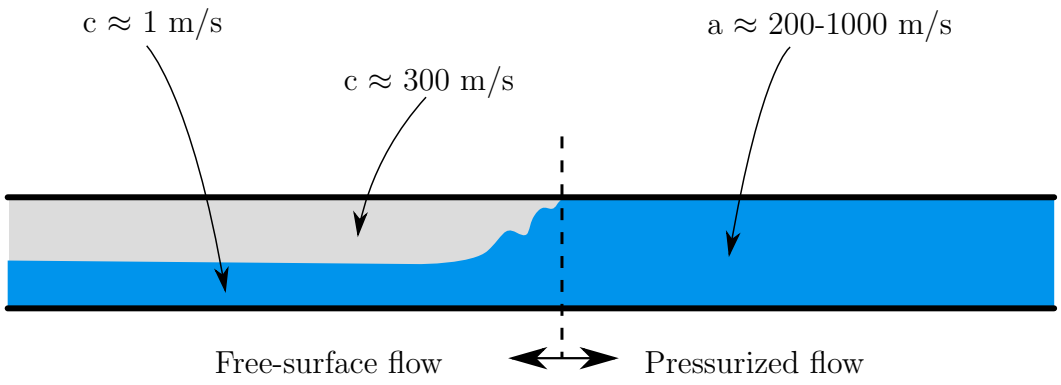

Figure 4.3: Average Courant number for different portions of the flow when entrapped air pocket is present.

In such conditions, free surface bores could be simulated under extremely low Courant numbers with no significant diffusion oscillations. The mathematical formulation for the Roe scheme is presented in [Macchione and Morelli, 2003] and can be seen in equations 2.31 to 2.38.

For dry bed regions of the flow, it was assumed that the flow depth would start as a minimum water depth of 1 mm. In such cases, the model would then predict the existence of a non-physical flow of this thin layer down the pipeline slope. To deal with this problem it was used the approach presented in [Sanders et al., 2011]. In this formulation, in order keep a minimum water layer with no motion and at the same time keep the stationarity of the solution, two criteria were followed in order to calculate the flow at a certain finite volume cell: one is based on the ratio between friction forces and the other based on the minimum submerged area of the cell. After computing these criteria to all cells in the domain, only the cells in which at least one of the two criteria is met have the flow calculated. The first criteria is $s > s^*$ where s^* was chosen to be 0.1 as suggested in [Sanders et al., 2011] and is based on the following equations:

$$s = \frac{c_D u^2}{g R_h |dz/dx|} \tag{4.7}$$

where R_h is the hydraulic radius and:

$$c_D = gn^2 {R_h}^{-1/3} \tag{4.8}$$

The second criteria follows the same logic, in which the flow is calculated if $A > A^*$, with A^* defined in equation 4.9:

$$A_i^* = \frac{D^3}{96|\Delta z_i|}\left[9sin\left(\frac{\theta^*}{2}\right) - 6cos\left(\frac{\theta^*}{2}\right)\theta^* + sin\left(\frac{3\theta^*}{2}\right)\right] \tag{4.9}$$

where

$$\theta^* = 2cos^{-1}(1 - 2|\Delta z_i|/D) \tag{4.10}$$

and Δz_i is the vertical elevation difference between both cell sides.

With this, the criteria to consider if a cell is a dry bed ($wet_i = false$) or is wet is:

$$\begin{cases} wet_i = true, & \text{if } A_i > A_i^* \text{ and } s_i > s_i^* \\ wet_i = false, & \text{otherwise} \end{cases} \tag{4.11}$$

where wet_i is a boolean variable used to synthesize those two criterion in a single variable. The momentum equation 2.31 is solved for Q_i^{n+1} only if $wet_i = true$, with $Q_i^{n+1} = 0$ otherwise.

4.1.2 Water phase source terms

Two source terms were considered for the water phase modeling, one accounting for pipe walls friction and another one accounting for pipe slope, both presented in [Sanders et al., 2011]. For the pipe walls friction source term, a semi-implicit formulation based on the Manning's equation was used, while for the pipe slope a formulation which preserves stationarity of the solution was used.

The source term for gravity forces in a sloped pipe presented in [Sanders et al., 2011] follows the formulation presented in [Capart et al., 2003], which preserves stationarity of the solution, avoiding non-physical oscillations. In this formulation, two variables Δh_s and Δw_{level} represent the linear change of h_s and w_{level} in the cell. These are computed as:

If $v_i = false$ then $\Delta w_{level} = 0$ and:

$$\Delta h_{si} = \begin{cases} 0 & \text{if } s_i \geq s^* \\ -\dfrac{\Delta z_i}{2}[1 + cos(\pi s_i / s^*)] & \text{if } s_i < s^* \end{cases} \tag{4.12}$$

If $v_i = true$ and $wet_i = true$ then $\Delta h_{si} = 0$ and:

$$\Delta w_{level} = \begin{cases} 0 & \text{if } s_i \geq s^* \\ -\dfrac{\Delta z_i}{2}[1 + cos(\pi s_i / s^*)] & \text{if } s_i < s^* \end{cases} \tag{4.13}$$

If $v_i = true$ and $wet_i = false$ then:

$$\Delta w_{level} = \Delta z_i,\ \Delta h_{si} = 0 \tag{4.14}$$

With Δh_s and Δw_{level} calculated, the bed slope source is calculated as follows:

$$S_{0i} = -\frac{1}{\Delta x_i}\left[I\left(w_{level i} + \frac{1}{2}\Delta w_{level i}, h_{si} + \frac{1}{2}\Delta h_{si}\right) - I\left(w_{level i} - \frac{1}{2}\Delta w_{level i}, h_{si} - \frac{1}{2}\Delta h_{si}\right)\right] \tag{4.15}$$

where $I(w_{level i}, h_{si}) = A(h_c + h_s)$ represented in equation 2.21.

For the friction between water and the pipe, a formulation for the source terms based on the Manning equation was used in a semi-implicit fashion, as shown in equation 4.16:

$$(S_f)_i^{n+1} = (c_D)_i^n \frac{P_i^n Q_i^{n+1} |Q_i^n|}{(A_i^n)^2} \tag{4.16}$$

which is linear in Q_i^{n+1} to avoid iteration and c_D is defined in equation 4.8. Considering that the effects of friction added to a Q^* which is an estimate of Q_i^{n+1} without friction considered would cause decrease Q_i^{n+1}, one have that:

$$Q_i^* - Q_i^{n+1} = \Delta t (c_D)_i^n \frac{P_i^n |Q_i^n|}{(A_i^n)^2} Q_i^{n+1} \tag{4.17}$$

which leads to:

$$Q_i^{n+1} = \frac{Q_i^*}{1 + \Delta t (c_D)_i^n \frac{P_i^n |Q_i^n|}{(A_i^n)^2}} \tag{4.18}$$

The sequence for the calculation is then:

1. Calculation of the flow rate considering the gravity force but not the friction losses source term (Q^*);

2. Calculation of the corrected (final value) flow rate based on Q^* and equation 4.18.

4.1.3 Water phase boundary conditions

The upstream boundary condition for water phase refers to all which is inside the red dashed box in figure 4.2. It is based on an iterative solution that ensures that local continuity and linear momentum at the pipeline inlet are satisfied, regardless of the flow regime at that location. The local continuity equation for the reservoir is:

$$\frac{dH_{res}}{dt} = Q_{rec} - Q_{in} \tag{4.19}$$

where H_{res} is the reservoir water level, Q_{rec} is the flow rate which is admitted into the reservoir from the recirculation system and Q_{in} is the flow rate which enters the upstream end of the pipe. The calculation of the updated flow velocity at the upstream boundary cell (u_1^{n+1}) uses an ordinary differential equation representing the linear momentum conservation,

which in turn is derived from a lumped inertia approach:

$$u_1^{n+1} = u_1^n + \Delta t \left\{ \left[\frac{g}{\Delta x} \left(H_{res}^n - K_{eq} \frac{u_2^n |u_2^n|}{2g} \right) - (w_{depth_2} + max(0, {h_{s2}}^n + {h_{air2}}^n)) \right] - f \frac{u_2^n |u_2^n|}{2\Delta x} - \frac{{u_2^n}^2}{2\Delta x} \right\} \tag{4.20}$$

where w_{depth} is the local water depth, n is the time step index, K_{eq} is the overall local loss coefficient in the inlet and f is the friction head loss in the short pipe portion inside the boundary condition right after the inlet.

After the velocity in the cell is obtained, Froude number is calculated with the current w_{depth_1} in order to assess if the flow is subcritical. If this is the case, ${w_{depth}}_1^{n+1}$ is updated according to the M.O.C. Hartree for free-surface flows as shown in [Sturm, 2001]:

$$\begin{cases} r = dt/dx \\ u_s = \dfrac{u_1^n + r(u_2^n c_1^n - u_1^n c_2^n)}{1 + r(-u_1^n + u_2^n + c_1^n - c_2^n)} \\ c_s = \dfrac{c_1^n + r u_s (c_1^n - c_2^n)}{1 + r(c_1^n - c_2^n)} \\ y_s = {w_{level}}_1^n + r|u_s - c_s| \cdot ({w_{level}}_2^n - {w_{level}}_1^n) \end{cases} \tag{4.21}$$

and finally

$${w_{level}}_1^{n+1} = {w_{level}}_i^n + (u_1^n - u_s)\frac{c_s}{g} \tag{4.22}$$

where u_s, c_s and y_s are the interpolated velocity, celerity and water depth in between the first and the second cells. If flow depth at inlet is less than the pipe diameter D then the surcharge head h_s is set to zero. On the other hand, if ${w_{level}}_1^{n+1} > D$, flow at inlet is pressurized, h_{air} is set to zero and h_s is recalculated to match the piezometric head at the upstream end, calculated with the energy equation. With the depth and the pressure head updated, the flow area A_1^{n+1} is updated and a new flow rate is then calculated with u_1^{n+1} and A_1^{n+1}.

The downstream boundary condition can be a fully opened or closed valve. For the case in which the valve is fully opened, the approach called transmissive condition presented in [Toro, 2001] is used:

$$\begin{cases} {w_{level}}_{No}^{n} = {w_{level}}_{No-1}^{n} \\ {h_s}_{No}^{n} = {h_s}_{No-1}^{n} \\ u_{No}^{n} = u_{No-1}^{n} \end{cases} \tag{4.23}$$

where the subindex No means the number of nodes used in the discretization. For the case in which the downstream boundary condition is a closed valve the boundary condition is calculated enforcing the relevant characteristic equation and zero velocity at the downstream end. The MOC Hartree is then used as:

$$\begin{cases} u_r = \dfrac{u_{No}^{n} + r(-u_{No}^{n} c_{No-1}^{n} + c_{No}^{n} u_{No-1}^{n})}{1 + r(u_{No}^{n} - u_{No-1}^{n} + c_{No}^{n} - c_{No-1}^{n})} \\ c_r = \dfrac{c_{No}^{n} + r u_r (c_{No-1}^{n} - c_{No}^{n})}{1 + r(c_{No}^{n} - c_{No-1}^{n})} \\ S_{f_r} = n^2 \dfrac{u_r |u_r|}{(R h_{No}^{n})^{1.333}} \\ K_r = u_r + g\dfrac{y_r}{c_r} - g(S_{f_r} - S_{0No})\Delta t; \end{cases} \tag{4.24}$$

and finally, with the velocity u_{No}^{n} set to zero:

$${w_{level}}_{No}^{n+1} = \frac{c_r}{g}(K_r) \tag{4.25}$$

where u_r, c_r, S_{f_r} and K_r are the interpolated velocity, celerity, friction slope, and a constant accounting for the interpolated previous time step values in between the last and the second last cells. If ${w_{level}}_{1}^{n+1} > D$, the flow depth at the downstream end becomes pressurized. In such case, ${w_{level}}_{1}^{n+1}$ is set to the value of the pipe diameter and h_s is set as the extra head of the cross section minus D, and $h_a ir$ is set to zero.

4.1.4 Air phase modeling

In the proposed model, air is initially considered as a continuous layer over the water layer (stratified water in free-surface flow mode). During the simulation, air is handled in one of two following manners:

1. At the first stages of the filling, when the air within a given pipe reach consists in an entire layer that is connected to atmosphere at the ventilation orifice and at its lowest point within the pipe (ideal ventilation), it is assumed that the air pressure in the entire layer is approximately atmospheric, and air velocity is assumed negligible. This condition persists until a pocket is formed at the lowest point during the filling process.

2. At the second stage, once an air pocket is formed, the connection to the atmosphere at its lowest point is lost, and air phase pressure is expected to be varying above atmospheric values, requiring calculations with either one of the two presented air phase models to determine its pressure and influence in the water flow.

An algorithm was developed to track air pocket volume, start and end nodes as it shrinks in order to simulate its behavior with any of the two models. For this, the mechanism considered for air pocket formation is the isolation of an air mass due to the development of a flow regime transition interface or a closed downstream valve. As mentioned, it is assumed that during a pipeline filling event this air pocket will be delimited by a ventilation orifice and a flow regime transition interface (or alternatively a closed valve). This interface will move mainly towards the air pocket ventilation point, compressing the air pocket and forcing its elimination through the ventilation orifice, as it is sketched in Figure 4.2.

The first step for tracking the air pocket is to check if the air mass has contact from down or upstream with sources of perfect ventilation. For this, a routine scans the pipe twice, leaving from the first cell (upstream) towards the last cell (downstream) and from last towards the first, to check the availability of ideal ventilation from the left and/or from

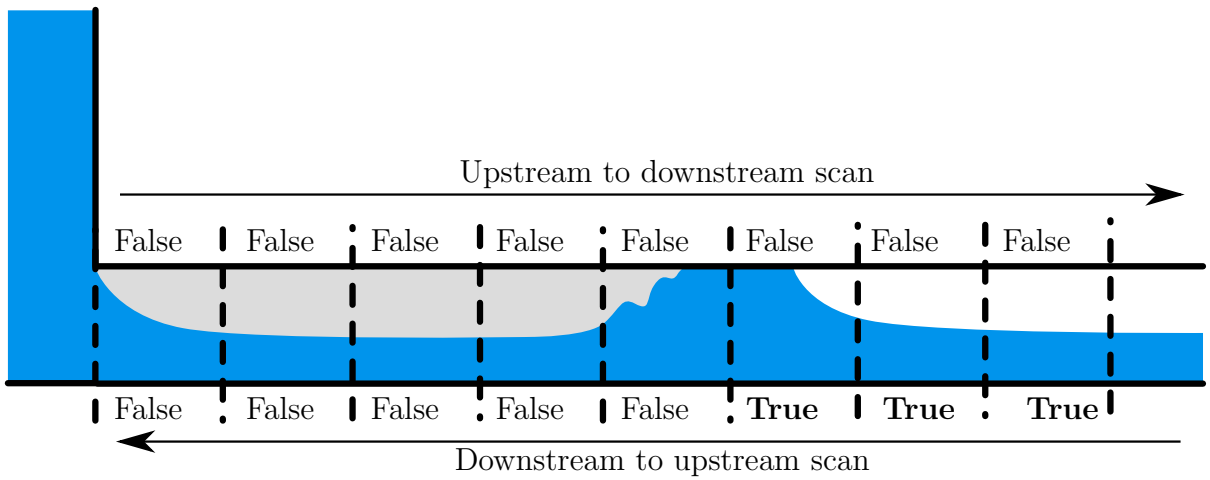

Figure 4.4: Pocket find graphical example

the right sides of the air masses. Figure 4.4 shows both scans and their return *true* or *false* for different cells in the pipe. The scan from upstream to downstream will set all the nodes of the pipe since its beginning as false for contact with ideal ventilation sources from the upstream until it reaches a source of perfect ventilation, which means until the downstream end of the pipe. On the other hand, the scan routine which starts from the last node (downstream) will set all the pipe nodes as true for contact with perfect ventilation sources from the downstream sides until it finds a cell which has water touching the crown of the pipe, so that from this point the contact with the downstream source of perfect ventilation is blocked.

After the pipe is scanned from both sides, the cells with contact to ideal ventilation sources from both sides set to false and water level w_{depth} below the crown of the pipe will be set as true for air pocket presence. Those cells will require the calculation of the air phase for them, having a non-atmospheric pressure associated with them in each time step.

Another important part of the algorithm is to determine the ventilation status of the cell. A ventilated cell means that it has direct contact with air, being this air mass is a air pocket or not. Therefore, the variable for ventilation v_i is set to true as long as $w_{depth_i} < d$, $w_{depth_{i+1}} < d$ or $w_{depth_{i-1}} < d$, so that if a negative pressure pressurized flow tries to form in the cell the cell will return to be a free-surface water flow.

4.2 Air phase modeling - Uniform Air Pressure Head (UAPH) approach

The model alternative that uses UAPH model assumes: a) uniform pressure in the whole air phase; 2) the validity of the ideal gas law; and 3) isothermal air flow. This model may be expressed either as:

$$\rho^n V_p^n = \rho^{n+1} V_p^{n+1} \qquad \rightarrow \qquad M_{air}^n = M_{air}^{n+1} \tag{4.26}$$

where M_{air} is the mass of air within the pocket with volume V_p, and ρ is the specific mass of air. In order to consider the air escape or admission an extra term was added to equation 4.26, yielding:

$$\rho^n V_p^n = \rho^{n+1} V_p^{n+1} + {M_{air}}_{out}^{n+1} \tag{4.27}$$

where $M_{air\,out}$ is the air mass that escapes through the ventilation orifice in that instant, calculated as presented in equation 4.35 presented ahead.

4.3 Air phase modeling - Euler equations approach

The second alternative to model the air phase uses a discretized framework, applying an one-dimensional, isothermal form of the Euler equation:

$$\mathbf{U} = \begin{bmatrix} \rho \\ \rho u \end{bmatrix}, \ \mathbf{F}(\mathbf{U}) = \begin{bmatrix} \rho u \\ \rho u^2 + p \end{bmatrix}, \ \mathbf{S}(\mathbf{U}) = \begin{bmatrix} S_1 \\ S_2 \end{bmatrix} \tag{4.28}$$

with

$$p = \rho \alpha^2 \tag{4.29}$$

where $\mathbf{U}$ is the vector of conserved variables, $\mathbf{F}$ is the fluxes vector, $\mathbf{S}$ is the vector of source terms, α is the celerity of the acoustic waves in the air, and S_1 and S_2 are source terms for the continuity and momentum equations, respectively, as explained ahead.

Applying the Lax-Friedrichs scheme - LxF - as presented in [Toro, 2001] to equation 4.28, one has the following expressions to update the conserved variables:

$$\begin{aligned}\rho_i^{n+1} &= \frac{\rho_{i+1}^n + \rho_{i-1}^n}{2} - \frac{\Delta t}{2\Delta x}\left[(\rho u)_{i+1}^n - (\rho u)_{i-1}^n\right] + \Delta t S_{disp,i} \\ (\rho u)_i^{n+1} &= \frac{(\rho u)_{i+1}^n + (\rho u)_{i-1}^n}{2} - \frac{\Delta t}{2\Delta x}\left\{\left[(\rho u)_{i+1}^n - (\rho u)_{i-1}^n\right]\frac{u_{i+1}^n + u_{i-1}^n}{2}\right. \\ &\qquad \left. + \alpha^2 \frac{\rho_{i+1}^n - \rho_{i-1}^n}{2\Delta x}\right\} + \Delta t(S_{disp,i} + S_{f_a})\end{aligned} \tag{4.30}$$

where $S_{disp,i}$ and S_f are source terms. The choice for LxF scheme was based on its simplicity and the lack of shocks in the air phase flow.

4.3.1 Air phase source terms

In pipeline filling problems, the mechanism causing the motion of the air phase is the displacement of air in the cross section caused by changes in the water flow depth underneath the air pocket. This effect is accounted for in the source terms S_{disp}, as presented in [Toro, 2009]:

$$\mathbf{S_{disp}} = \frac{1}{A}\left(\frac{\partial A_{air}}{\partial t} + \frac{\partial A_{air}}{\partial x} u_{air}\right)\begin{bmatrix}\rho \\ \rho u\end{bmatrix} \tag{4.31}$$

where $A_{air} = (\pi/4)D^2 - A$, and is calculated only in free surface flow cells. An explicit implementation of source terms S_{disp} led to instability of the numerical solution, so a semi-implicit approach was applied here. The air phase is first calculated without considering changes in A_{air} returning a preliminary solution $\check{\mathbf{U}} = [\check{\rho}, \check{\rho u}]$, which then needs to be adjusted with a correction factor ϕ so that a definitive solution is achieved. The definitive solution and correction factor ϕ are represented by:

$$\mathbf{U} = \begin{bmatrix}\rho \\ \rho u\end{bmatrix} = \phi \begin{bmatrix}\check{\rho} \\ \check{\rho u}\end{bmatrix} \tag{4.32}$$

with

$$\phi = \left[\frac{1}{1 + \frac{1}{A_i^n} \left(\frac{{A_{air}}_i^{n+1} - {A_{air}}_i^n}{\Delta t} + \frac{{A_{air}}_{i+1}^{n+1} - {A_{air}}_{i-1}^{n+1}}{2\Delta x} u_i^{n*} \right)} \right] \tag{4.33}$$

The solution of these source terms presented some oscillations at the region of the strongest free surface flow gradients, at the vicinity of the pressurization front. Two approaches were used together to minimize these oscillations. The first one was to limit ϕ to the range $\phi = [1.005 : 0.995]$. The second was the application of an oscillation filter in the air phase internal nodes, following [Vasconcelos et al., 2009a] with $\epsilon = 0.05$. This approach resulted in a good balance between pressure accuracy, and presented continuity error to the air phase modeling limited to an average of 7% for the tested cases.

Another source term added to the simulation of the air phase flows was the friction between the air phase and the pipe walls, as described in [Arai and Yamamoto, 2003]:

$$S_{f_a} = \frac{f_a P_a u_a |u_a|}{8 g A_{air}} \tag{4.34}$$

where P_a is the perimeter of the air flow.

4.3.2 Air phase boundary conditions

For the UAPH model, the boundary condition used at the uppermost point in the pipeline reach (where the ventilation valve was located) was a discharging orifice. The orifice is represented by an equation similar to one presented in [Zhou et al., 2002a]:

$${M_{air}}_{out}^{n+1} = \Delta t C_d A_{orif} \rho^{n+1} \sqrt{2 \frac{\rho^{n+1} - \rho_{atm}}{\rho_{atm}} \alpha^2} \tag{4.35}$$

where C_d is the discharge coefficient that is assumed as $C_d = 0.65$, and A_{orif} is the orifice area. Equation 4.35 was coupled with equation 4.27 to yield:

$$\rho^n V_p^n = \rho^{n+1} V_p^{n+1} + \Delta t C_d A_{orif} \rho^{n+1} \sqrt{2 \frac{\rho^{n+1} - \rho_{atm}}{\rho_{atm}} \alpha^2} \tag{4.36}$$

For the Euler equation model, two boundary conditions are required. At the lower point of the pipe, where water pressurization front is displacing the air, the reflexive boundary condition in equation 4.37 presented in [Toro, 2001] was used:

$$\begin{cases} \rho^n_{No_{air}} = \rho^n_{No_{air}-1} \\ {u_{air}}^n_{No_{air}} = -{u_{air}}^n_{No_{air}-1} + 2 b_{vel} \end{cases} \tag{4.37}$$

where b_{vel} is the pressurizing front velocity and No_{air} is the number of cells in the air pocket. This boundary condition accounts for the pressurizing front velocity, so that when it moves from a cell to another the loss of air due to the shrinking of the pocket was previously compensated. However, since the source terms which account for the cross-section area shrinking already accounts for the movement of this mass, both cannot be used simultaneously or else the air present in the last cell would be counted twice.

If the area variation source terms are used, b_{vel} equals zero. On the other hand, if the wall movement is considered in the boundary condition, the mentioned source terms are not used and b_{vel} needs to be calculated. For this case, two formulations were considered:

$$b_{vel} = \frac{(uA)_{i-1-k} - (uA)_{i+k}}{A_{i-1-k} - A_{i+k}} \tag{4.38a}$$

$$b_{vel} = \Delta x \frac{i^m - i^{m_{last}}}{\delta t} \tag{4.38b}$$

where i is the cell number of the pressurization front, k is the number of cells before and after the pressurizing front to be considered in the control volume surrounding the pressurizing front, m is the last time step when the pocket's last cell moved from one cell to another, m_{last}

is the time step when the pressurizing front moved considered for the last b_{vel} calculation, and δt is time interval between both instants. For instance, one can choose to recalculate the pressurizing front velocity when the front moves two cells, to that m would be the current time step and m_{last} would equal $m-2$. It is important to notice that the first formulation in equation 4.38 can be used for the whole simulation time while the second one needs a velocity to start with since no previous values exist then. For that, the first formulation is used until the pressurizing front moves a certain distance and from then on the second formulation can be used.

At the uppermost point, the ventilation orifice boundary condition for the Euler equation approach is similar to the UAPH model in the sense that both apply a continuity equation along with the orifice equation. The continuity equation for this boundary condition is:

$$\Delta t A_{air}^{n+1} \rho_1^{n+1} u_1^{n+1} = A_{air}^{n+1} \Delta x (\rho_1^{n+1} - \rho_1^n) + M_{air_{out}}^{n+1} \tag{4.39}$$

where $M_{air\,out}$ is the air mass discharged through the ventilation orifice, calculated using equation 4.35. Equation 4.39 is solved for u_1^{n+1} using the Riemann invariants for the isothermal, one-dimensional, primitive version of the Euler equation [Pulliam, 1994]:

$$u_{air\,1} = u_{air2} - \alpha(log_{10}\rho_2 - log_{10}\rho_1) \tag{4.40}$$

4.4 Experimental program

An experimental investigation was conducted to gather insights on the characteristics of the pipeline filling problem, and also to validate the proposed numerical model. The experimental apparatus was set up and works started in May, lasting until late June, 2011. The current apparatus was inspired in the one presented in [Trajkovic et al., 1999].

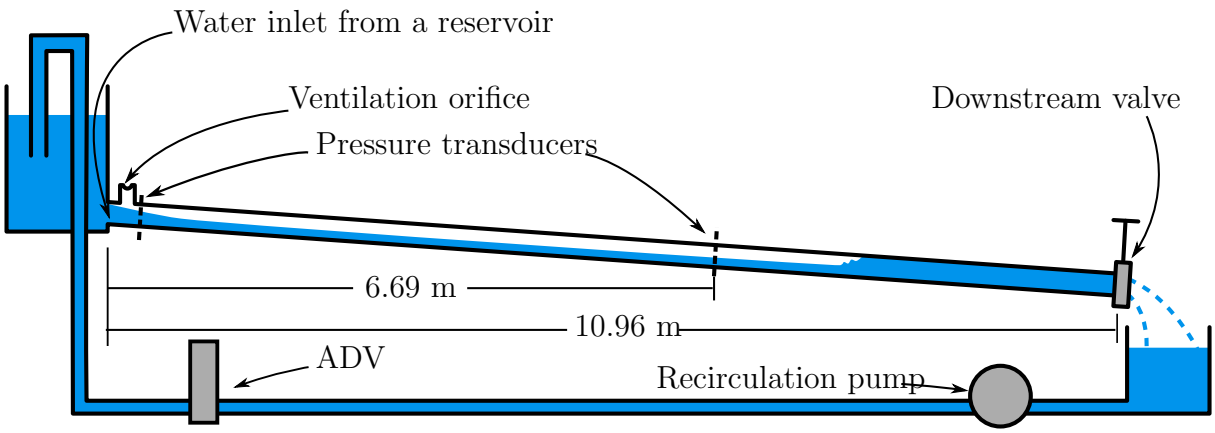

Figure 4.5: Test representation

4.4.1 Experimental apparatus setup

A sketch of the experimental apparatus is presented in Figure 4.5. The experimental apparatus was a 10.96-m long, 101.6-mm diameter clear PVC pipeline with adjustable slope. At the upstream end, a 0.66 m^3 capacity water reservoir supplied flow to the pipeline through a 50 mm ball valve; at the downstream end flow discharged freely through a 101.6 mm knife gate valve into a 0.62 m^3 reservoir, and flow was subsequently recirculated with pumps. Right after the inlet control valve, a T junction was installed in the pipe so that different caps with ventilation orifices could be installed. Initial, steady flow conditions were such that free surface flows exist at the whole pipeline, as the downstream gate was fully opened. A sudden closure maneuver (within 0.3 seconds) of the knife gate valve at the downstream end of the pipeline blocked the downstream ventilation, triggered a backward-moving pressurizing interface, and resulted in the entrapment of an air pocket. These air pockets became pressurized as water accumulated at downstream end of the pipe pushed the air mass through the ventilation orifice in the beginning of the pipe. Two pressure transducers MEGGIT-ENDEVCO 8510B-5 were installed at selected locations along the pipe (upstream end and 39% of the pipeline length from the knife gate valve). Transducer results were calibrated each experimental run with the aid of four digital manometers, with of 3.5-m H_20 maximum pressure head and 0.3% accuracy. Flow rates were measured with a MicroADV

positioned in the recirculation system, and confirmed by a paddle-wheel flow meter. The presented apparatus was inspired in the one presented in work by [Trajkovic et al., 1999]; among the main modifications was the absence of intermediate ventilation points.

4.4.2 Experimental procedure

1. With the desired slope set in the pipeline, the pumps were started; valves near the pump were opened enough to provide selected steady flow rate to the system;

2. The desired ventilation orifice was installed;

3. When water level at upstream reservoir attained steady level, it was performed readings at all manometers, as well the upstream reservoir head;

4. The data logging was started for the pressure transducers, for the flow rate measured with the MicroADV, and for the head at the upstream reservoir measured with the manometer;

5. The downstream knife gate valve was rapidly maneuvered and closed entrapping an air pocket and creating a backward-moving pressurization front;

6. Digital cameras (30 FPS) recorded the whole pipe filling process, one of them tracking the bore and another one tracking the pressurization interface;

7. When the pressurization interface approached the ventilation orifice, the ventilation orifice was shut to avoid water leakage;

8. Pump was shut down and control valves closed so that pressure could attain a static level;

9. Manometers were read and data collection with logging software stopped;

The use of two cameras to track the inflow/pressurization front was particularly necessary in the case when interface breakdown [Vasconcelos and Wright, 2005] was noticed. Otherwise, just one camera tracking the pipe-filling bore front was used. The described experimental program varied systematically flow rates, ventilation orifice diameters and pipeline slopes. Table 4.1 presents the ranges of the tested experiment variables, with a total of 36 conditions tested. A minimum of two repetitions were performed to ensure consistency of the data collected.

Variables	**Tested values**	**Normalized values**
Flow rate	2.53, 3.79 and 5.05 l/s	0.245, 0.368 and 0.490
Slope	0.5, 1 and 2%	N/A
Ventilation orifice diameter	0.63, 0.95, 1.27, and 5.06 cm	0.0625, 0.09375, 0.125, 0.5

Table 4.1: Experimental variables. Flow rate was normalized as $Q^* = Q/\sqrt{gD^5}$ and ventilation diameter as $d^* = d_{orif}/D$ where D is the pipe diameter

Chapter 5

Results and analysis

In this chapter, a set of numerical and experimental results were presented. It starts with a discussion focused on the experimental results. This discussion will focus on quantitative results, such as pressure and pressurization front trajectories, and also in the flow features, such as interface breakdown and depression waves.

Later, comparisons between the modeling alternative for air phase and between models and experimental/field data are presented and discussed. The tests were created with three main purposes:

1. Evaluate the feasibility of running parallel discretized models for both air and water phases;

2. compare the different model approaches to simulate air phase during pipeline filling events; and

3. validate the model with experimental and field data.

The development of the model in its current version led to the creation of intermediate functional versions were tested, a process by which the strengths and weaknesses of different proposed ideas are evaluated. In the following two sections, intermediate and final versions of the model are presented with a evaluation of each version. Only the final version of the numerical model was compared with experimental and fields results.

5.1 Experimental results

Figure 5.1 shows the pressure history close to the ventilation orifice for all tested cases in the experimental program with normalized orifice diameter $d^*_{orif} = d_{orif}/D$ smaller or

equal to 0.125. The transducer at that station was located at the pipe crown, so it measured air phase pressures for most of the filling processes. As anticipated, higher pressurization levels were observed for smaller ventilation orifices and that the filling time was smaller for higher flow rates.

Air phase pressure head results were not significantly different for varying pipeline slopes. On the other hand, there was a slight difference in the filling time between different pipeline slopes for a given ventilation orifice and flow rate. This difference is attributed to the different initial water levels in the apparatus prior to the closing of the knife gate valve at the downstream end. Also in Figure 5.1, it can be noticed that for the smallest ventilation the air phase pressure head kept increasing during the filling process, indicating steady flow for these cases was not attained.

Figure 5.2 presents the pressure head histories for a point $x^* = x/L = 0.39$ (measured from the knife gate valve) for experimental runs with $d^*_{orif} \leq 0.125$ with $d^*_{orif} = \frac{d_{orif}}{D}$. These pressures were also measured at the pipeline crown. A sudden step up in the pressure values the moment in which the flow regime transition interface reached the transducer. As in the case of pressure measurements at the ventilation orifice, these pressures kept increasing due to the increase in the air pressure for the smallest ventilation case. The magnitude of the jump in the pressure readings was an indication of the strength of the pipe-filling bore front, and it increased for larger inflow rates and ventilation orifices. The absence of this discontinuity was a sign of either gradual pressurization interface and/or the occurrence of interface breakdown feature due to the interaction of the inflow front and the depression wave generated at the inlet caused by air pressurization. The relevance of this flow feature is that its occurrence may pose difficulties to pipeline filling models that use well-defined inflow interfaces as a modeling hypothesis, such as the models by [Liou and Hunt, 1996] and [Izquierdo et al., 1999].

To further illustrate the impact of the interface breakdown feature, Figure 5.3 presents two set of trajectories of moving pressurization interfaces for normalized flow rates of $Q^* =$

$Q/\sqrt{gD^5} = 0.245$ and 0.490 and 2% slope, measured for all tested ventilation diameters. All these interfaces start as pipe-filling bore fronts at $x^* = 0$ as the gate valve is closed, and such bores lasted until $x^* \approx 0.28$. For both flow rates interface breakdown was noticed when the smallest ventilation orifice was used. Upon occurrence of interface breakdown, the pipe-filling bore becomes an open-channel bore that moves more slowly toward the ventilation orifice, leaving an air intrusion on its top. Interestingly, as the backward-moving bores approached the ventilation orifice there seems to be an acceleration on their motion. The cause for this change in bore velocity is not determined at this point.

When interface breakdown occurred, interface measurements included both the position of the open-channel bore and the pressurization front. The latter was a gradual transition, and immediately following the interface breakdown it was noticed that the pressurization front retreated. Soon afterwards, the pressurization front resumed the motion toward the ventilation orifice, trailing the open-channel bore. Figure 5.4 presents the trajectories for the condition $Q^* = 0.245$ and 1% slope, for all four tested d^*_{orif}. The largest one ($d^*_{orif} = 0.50$) has not generated any sign of air pressurization, and the pipe-filling bore kept its shape as it propagated toward the ventilation point. However, for smaller ventilation orifices there was the occurrence of interface breakdown, and the the trajectory of the pressurization fronts (thin lines) are plotted along the trajectories of the pressurization bores. For the cases when $d^*_{orif} = 0.125$ and $d^*_{orif} = 0.0938$ the trajectory of the pressurization front was approximately parallel to the backward moving bore, which was moderately slowed by the interface breakdown. For the smallest ventilation ($d^*_{orif} = 0.0625$), on the other hand, the velocity of the pressurization bore was significantly reduced, with a much larger separation between the pressurization front and interface breakdown.

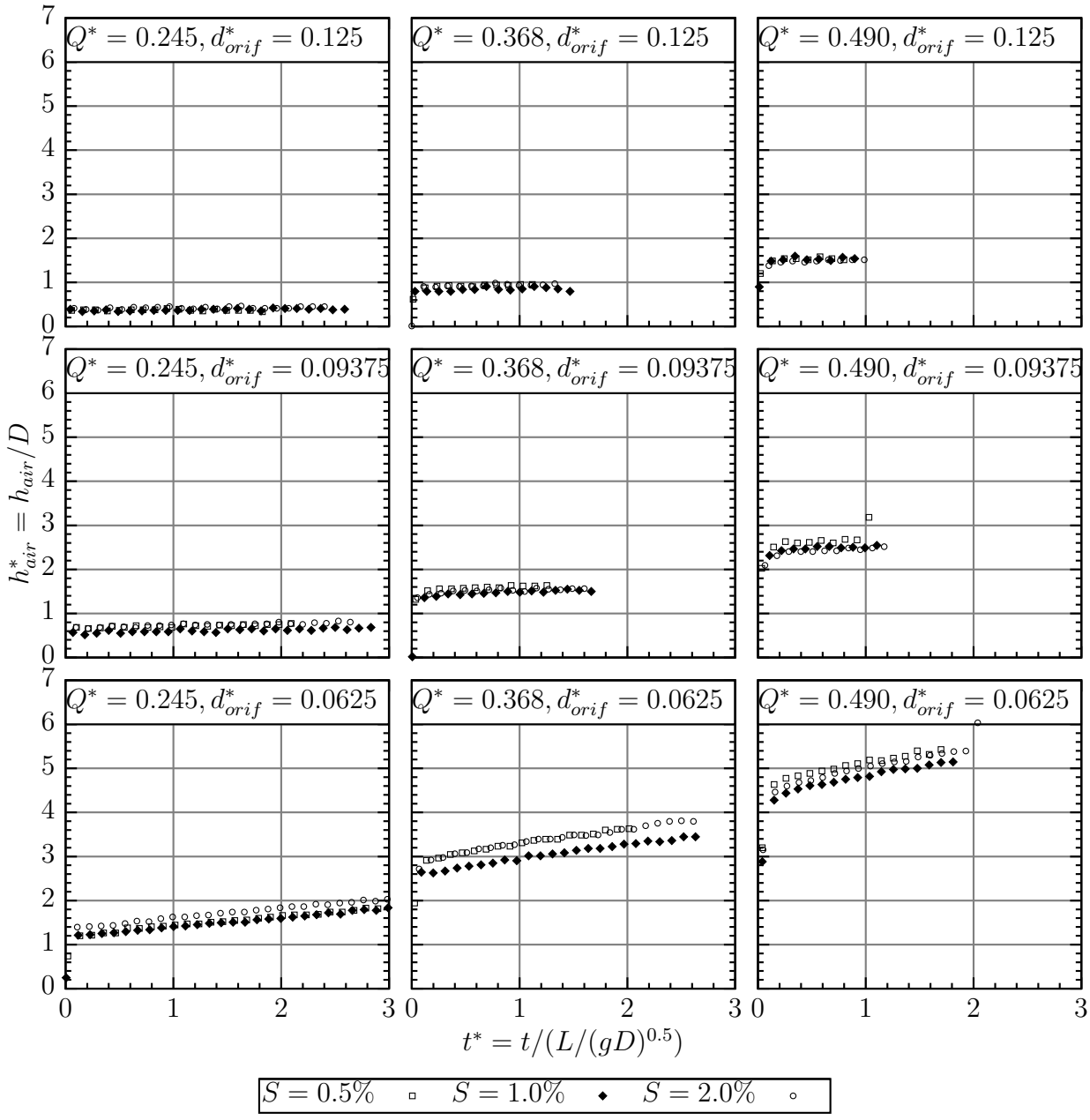

Figure 5.1: Air phase heads close to the ventilation orifice for all tested conditions.

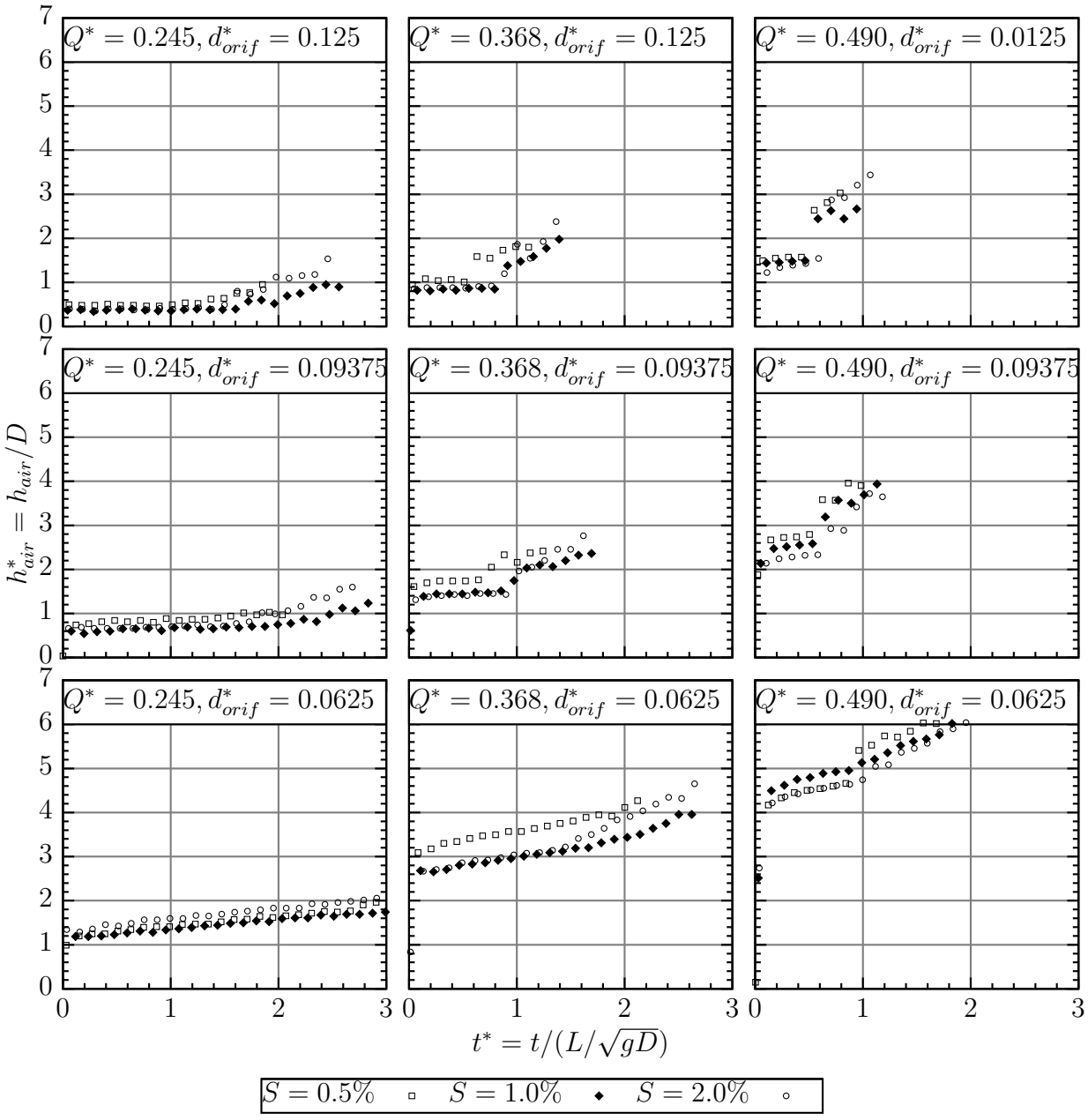

Figure 5.2: Air phase heads close to the ventilation orifice for all tested conditions.

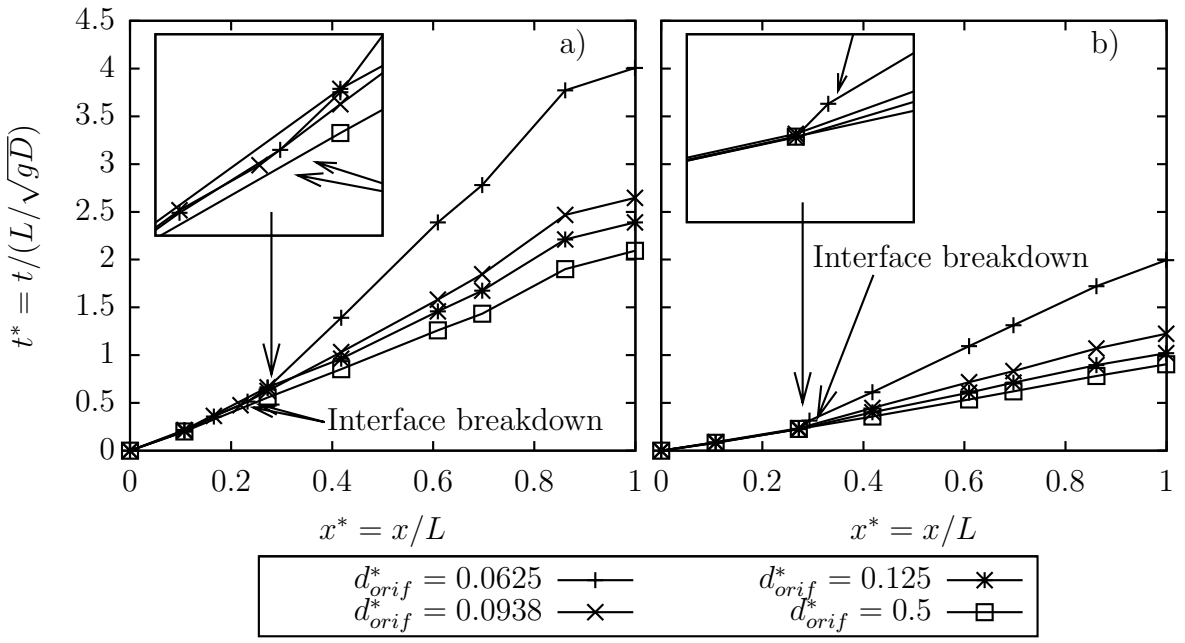

Figure 5.3: Trajectories of moving bore for recirculation flow rates of 2.53 l/s (a) and 5.05 l/s (b) and slope of 2%

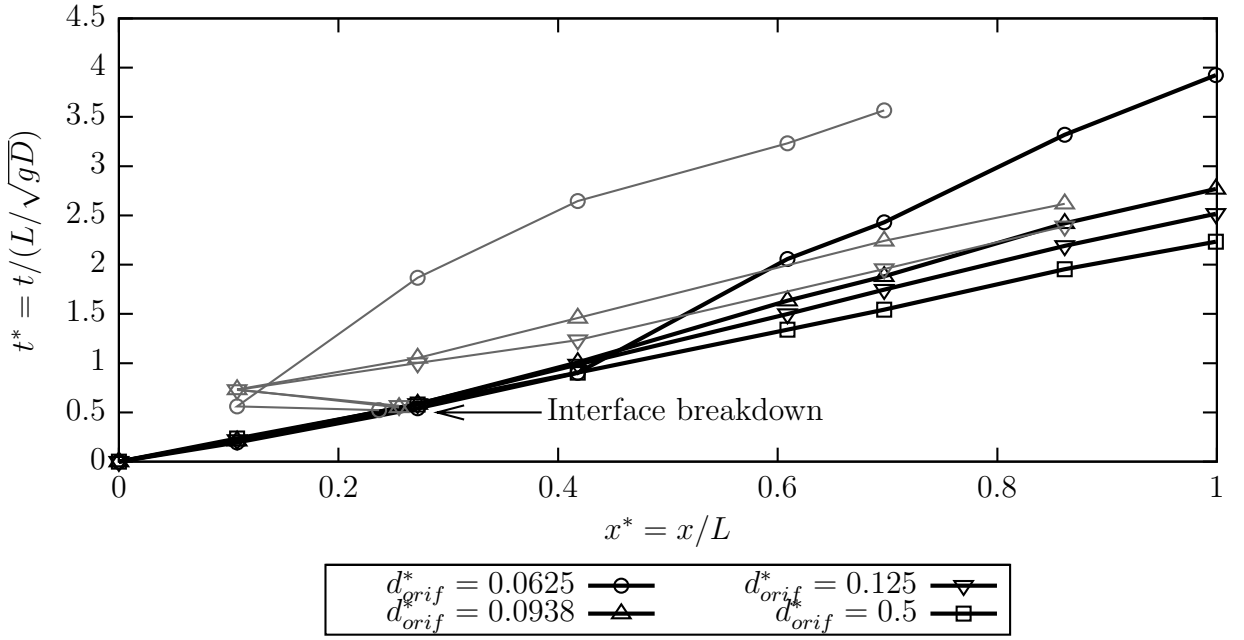

Figure 5.4: Trajectories of moving bore (thick line) and pressurization interface (thin line) for recirculation flow rate of 2.53 l/s and slope of 1%

5.2 First version of TPAir

5.2.1 Assessment of the Euler equation approach

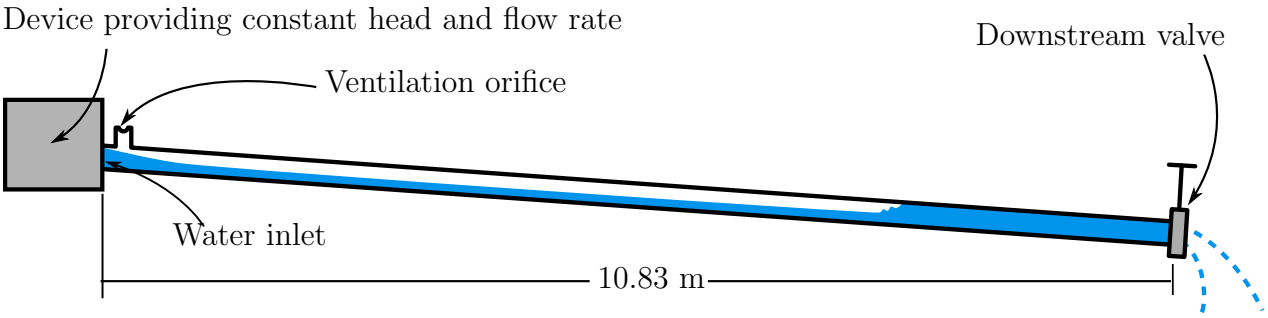

Figure 5.5: Model's first version layout.

The first test presented in [Trindade and Vasconcelos, 2011] was thought as a means to assess the idea of running parallel models for both phases, which means the coupling of the Euler equations for air phase with the Saint Venant equations for the water phase. The test case for this first model was comprised by a 10 cm diameter, 8.3 m-long pipeline slope was 2.7% downward with the flow, and free discharge conditions existed at the downstream end. At the upstream end flow rate and depth were kept constant due to the supercritical flow condition at that location. The general layout is presented in 5.5. In this first stage, the first functional version of the model with Euler equations approach was developed, using:

- Water source terms presented in [Sanders et al., 2011];
- Single phase Euler equation test model for air phase in order to develop the boundary conditions;
- Upstream ventilation orifice air boundary condition;
- Downstream moving bore (b_{vel}) calculated as in section 4.3.2 using air mass balance (equation 4.38a) for the whole calculation; and
- Air phase described by the isothermal, one-dimensional Euler equations coupled with the Saint Venant equations to model water phase.

The initial set up for the model consists in setting a flow rate and a initial depth predicted with Manning equation for the whole pipe. In order to get a better prediction for steady state, the model runs for 60 seconds with a transmissive boundary condition (equation 4.23). Unsteady flow conditions arise from abruptly closing the downstream valve at the time 60 seconds, after steady state is reached, blocking the flow and instantly generating an upstream-moving pipe filling bore, which expelled the air phase through the orifice at the upstream end. The main differences from the proposed example to the original configuration by [Trajkovic et al., 1999] are the flow rates tested (larger flows) and the fact that ventilation in the system is limited. Ideal ventilation condition is assumed to occur only at the downstream end prior to the valve closure.

The parameters varied for the test cases were the diameter of the ventilation orifice and the initial steady flow rate in the system, which resulted in varying initial water level. The choice of air orifice diameters was based on the work of [Zhou et al., 2002a] plus a larger orifice which provides near-ideal ventilation at the upstream and, yielding a total of three different ventilations. The smallest ventilation orifice corresponded to a case in which the air cushioning effects were dominant while the second larger orifice corresponds to the case in which air pressurization was minimal. Notice that albeit the imposition of Q in the pipeline is not a realistic type of boundary condition, its still useful for the model assessment that is the main goal of this research phase.

Variables	**Tested values**
Q^* Normalized flow rates ($\frac{Q}{\sqrt{gD^5}}$)	0.67 and 1.32
d^*_{orif} Normalized ventilation orifice diameter ($\frac{d_{orif}}{D}$)	0.028, 0.114 and 0.171

Table 5.1: Tested values for Euler equation approach assessment (orifice sizes based on the work by [Zhou et al., 2002a]).

Figure 5.6 shows the variation of the air pressure heads in the discharge orifice over time for both tested initial depths $y_0 = 0.5D$ and $y_0 = 0.8D$ (figures 5.6a and 5.6b, respectively). This figure indicates that the pipe filling time was smaller for $y_0 = 0.8D$, which was anticipated considering the faster motion of the upstream propagating bore upon valve closure. Since the inflow rate (and therefore uA in equation 4.38) is higher for the case when $y_0 = 0.8D$, while the area difference $A_2 - A_1$ is smaller, the bore moves much faster it larger depth. The resulting conditions for the air flow is that at the pressurizing bore the air phase pushed with a higher velocity, resulting in higher pressurization heads calculated at the air discharge cell with equation 4.35.

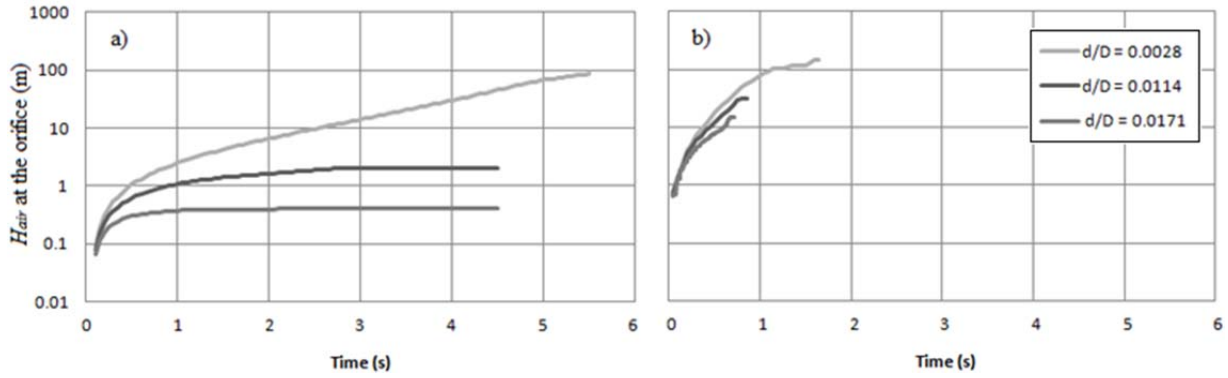

Figure 5.6: Pressures comparison at the ventilation orifice for a) initial depth of $0.5D$ and b) $0.8D$

For the two larger orifice sizes in figure 5.6a it can be noticed that the air flow reaches the steady state at about 60% of the simulation time. At this point, the air pressure gradient is uniform throughout the air phase. One notices the large difference in the final pressure values, as the smallest orifice yields a pressure head over two orders of magnitude higher than the one with the largest orifice. The discrepancy in the filling time, which should be the same because the inflow rate and pipe volume are fixed, comes from the relatively small celerity used in the computations, around 85 m/s. This situation is analogous to running simulations with a wide Preissmann slot value, as presented by [Vasconcelos and Wright, 2004] and discussed in section 2.1.2. While this version of the model is still unstable for higher celerity values (e.g. 200-300 m/s), this limitation was addressed in later versions of

the proposed model. Interestingly, the maximum air pressure predicted for higher initial flow rate conditions increased with the initial flow depth, except for the smallest orifice diameter.

For the smallest ventilation orifice case in figure 5.6a and for all cases in figure 5.6b, small pressure oscillations can be noticed. Those appear due to the air pressure waves reflecting at the edges of an smaller air cavity, which occurs in a much smaller period than the total filling time. Such an effect could not be represented in a model which considers uniform pressure along throughout air pocket. While the magnitude of these oscillations is small at this particular application, it is thought that for longer air pockets this may become a more significant issue, which could justify the use of Euler equations model in order to obtain accurate results.

Figure 5.7 presents two pairs of pressure histories illustrating the piezometric pressure evolution with time at a point close to the downstream valve ($x = 7.7m$) and another point further upstream ($x = 5.7m$), as in [Trajkovic et al., 1999], for the different tested depths. Figures 5.7a and 5.7b indicate slight differences in the pressure histories, with an abrupt pressure rise in Figure 5.7a at $t = 1.5s$ caused by the bore arrival at that point. A similar trend was also noticed for the largest initial water depth, with the bore sweeping at $x = 5.7m$ at the instant $t = 0.23s$, albeit with higher pressures and much more rapid filling.

Figure 5.8 presents the velocity history at the upstream station for both simulated flows. Generally, the proposed model predicts an increase of the velocity magnitude at the discharge point, with a value that approaches the celerity of the upstream propagating bore. As anticipated, this increase is more pronounced for larger discharge orifices. For the largest water depth, there is a final drop in the flow velocity, which is possibly due to the decrease in the upstream flow depth caused by air pressurization. Scatter in the data that appears for the smallest orifice results is due to the model difficulty in determining precisely the exact location of the bore interface at each time step, particularly for high air pressures conditions.

Figure 5.9 presents the piezometric profile at selected instants for both initial flow rates tested. One notices that the total piezometric profiles are much higher than the piezometric

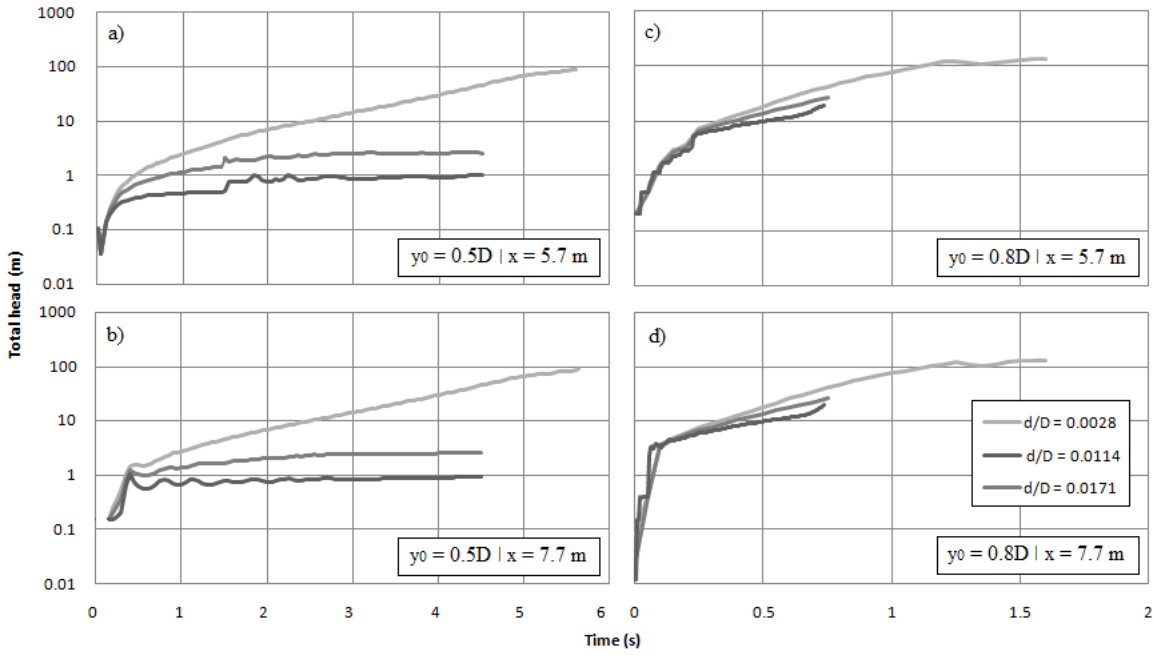

Figure 5.7: Pressure history at a) $x = 7.7m$ and $y_0 = 0.5D$, b) $x = 5.7m$ and $y_0 = 0.5D$, c) $x = 7.7m$ and $y_0 = 0.8D$, and d) $x = 5.7m$ and $y_0 = 0.8D$

profile solely due to water phase because of the strong air pressurization, and as expected this pressurization increases for smaller discharge orifices. At $t = 3s$, for the case when $y_0 = 0.5D$, one notices a fairly uniform pressure gradient for the air phase (at left) followed by a small pressure increase, which corresponds to the arrival of the bore at the location. On the other hand, for the case when $y_0 = 0.8D$, the air pressure is not uniform ahead of the bores, particularly for the two smaller orifice results. This non-uniformity will be re-evaluated in future versions of this model, after the inclusion of friction terms between air and water phases and between air and the pipe walls.

5.2.2 Comparison between both approaches

[Vasconcelos and Trindade, 2011] introduced the UAPH approach to the model framework and compared both approaches to simulate the air phase in the context of large-scale pipelines by means of a numerical investigation. To perform the comparison between both approaches, a two-reach pipeline configuration with an intermediate low point was proposed.

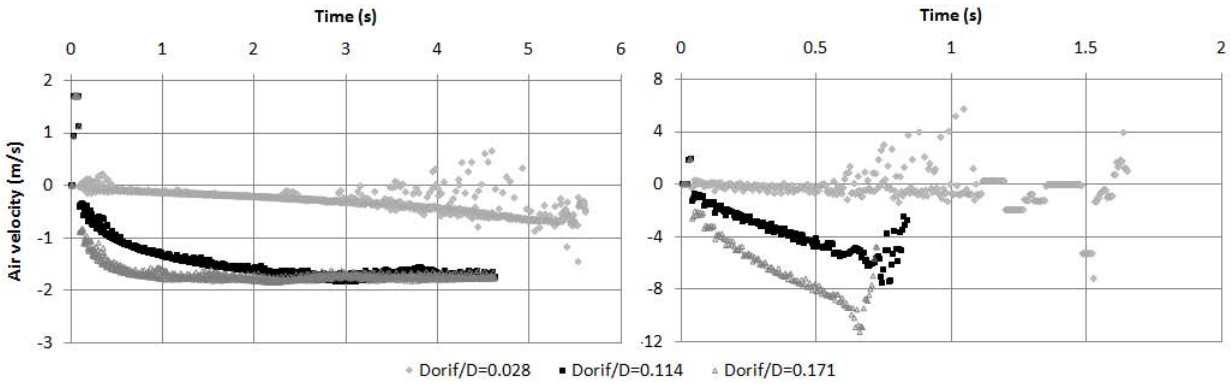

Figure 5.8: Air velocity at the upstream end of the pipe for tested flow rates

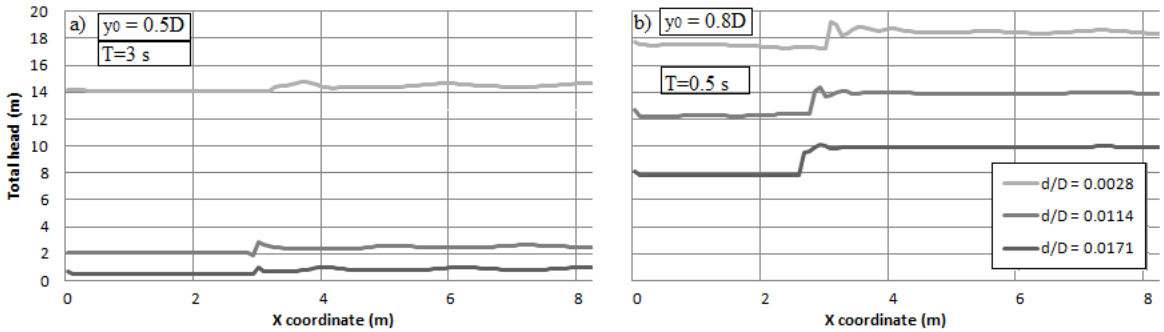

Figure 5.9: Head profiles along the pipe at selected instants

Both configurations parameters are presented in table 5.2. Friction factor for air phase calculation was based on Manning roughness values. Figure 5.10 presents a sketch of the hypothetical pipeline.

	L_1 **(m)**	L_2 **(m)**	S_1 (%)	S_2 (%)	**D (m)**	**n**
Conf. 1	1000	600	4	2	1.0	0.010
Conf. 2	4000	2000				

Table 5.2: Pipeline configurations parameters

The first reach was simulated using the TPA approach for the water phase and Euler equations or uniform pressure approach for the air phase. The second reach was treated as the downstream boundary condition of the first reach, being calculated using method of characteristics coupled with a variable depth until the whole connection is filled; afterwards the second pipe is computed using rigid column theory.

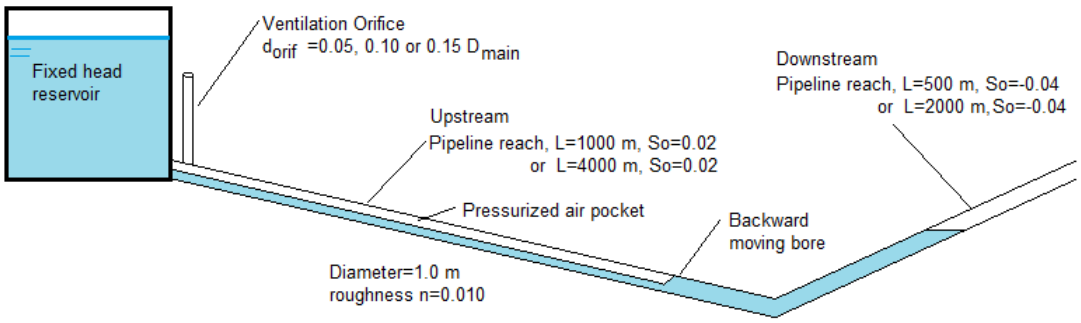

Figure 5.10: Hypothetical real sized pipeline sketch

At the upstream end a fixed head reservoir, which was calculated using equations 4.20 with fixed reservoir head and water depth and 4.21, provides water inflow (three different pairs of flow rates and heads considered) but does not allow for air escape; the air valve immediately downstream from the reservoir valve provides limited ventilation for the upstream pipe reach. Three ventilation sizes for the air valve were considered in terms of the diameter of the pipe: 5%, 10% and 15% of the pipe diameter. Overall nine conditions were tested for each one of the modeling approaches, and the variables tested with respective tested range are presented in table 5.3.

Variables	**Tested values**
Q^* Initial normalized flow rates $(\frac{Q}{\sqrt{gD^5}})$	0.125, 0.250, 0.500
d^*_{orif} Normalized ventilation orifice diameters $(\frac{d_{orif}}{D})$	0.05, 0.1, 0.15

Table 5.3: Long pipe tested values.

The qualitative behavior of the flow was generally the same for all tested cases. Some time after the flow was initialized (with a chosen constant reservoir head able to supply the specified initial flow rate), water reached the bottom of the system (connection between pipes) and started to fill this point as a pool. At this point, the system is still considered sufficiently ventilated so that the air pressure inside the upstream pipe equals the atmospheric pressure. After a certain time the whole cross-section at this bottom junction was filled and a water column formed at the downstream upward sloped pipe. When this happened a

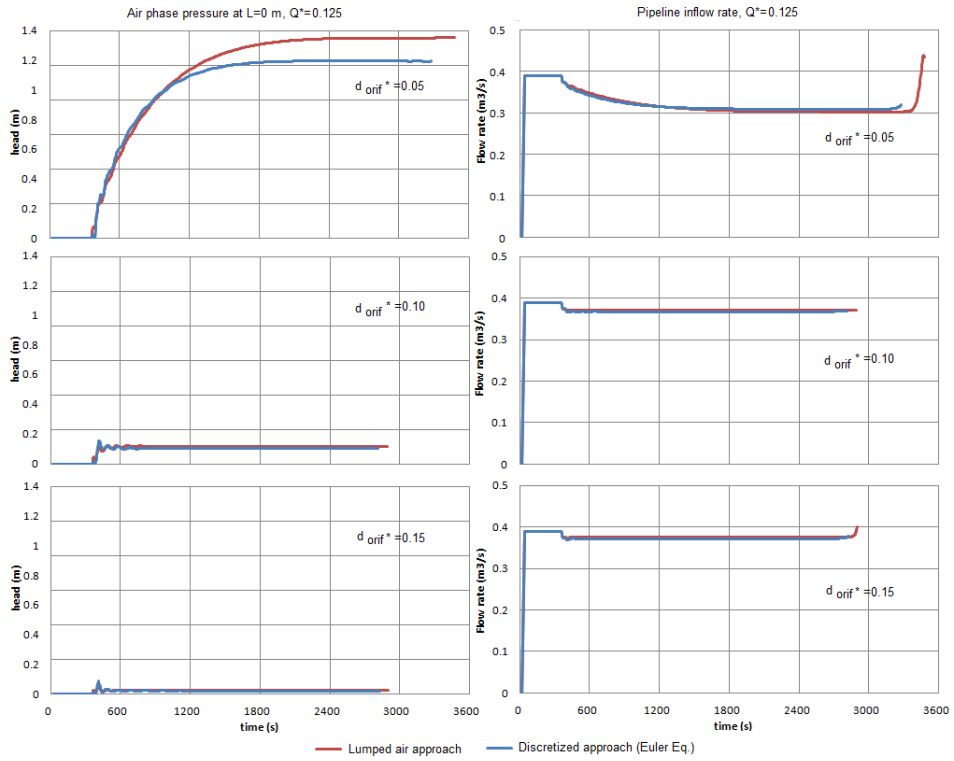

Figure 5.11: Comparison of heads at the ventilation orifice for $Q^* = 0.125$

pressurizing bore started to move upstream in the upstream pipe starting to pressurize the air, which was expelled through the ventilation orifice. The pressurized water flow in both pipes then oscillated in a way that resembles a U-pipe oscillation until the air got expelled.

Figures 5.11, 5.12 and 5.13 show head and water flow rates for the upstream end of the pipe, where the ventilation orifice and water inlet are located. It can be seen that the flow rate decreased as the pressurizing bore moves upstream while the air pressure increased. While air pressure continued to rise for the smallest ventilation tested, sometimes to significant levels, it becomes stable for orifices diameters of 10% and 15% of the water main diameter. Because flow rate decreases proportionally to the air pressure, the filling time may increase significantly (up to 25%) when compared with a condition with larger ventilation size, as it would be expected. Figures 5.11 to 5.13 also show that both models pressure predictions at the ventilation orifice were highly similar when air pressurization was low, which means below or around 1 m of water column.

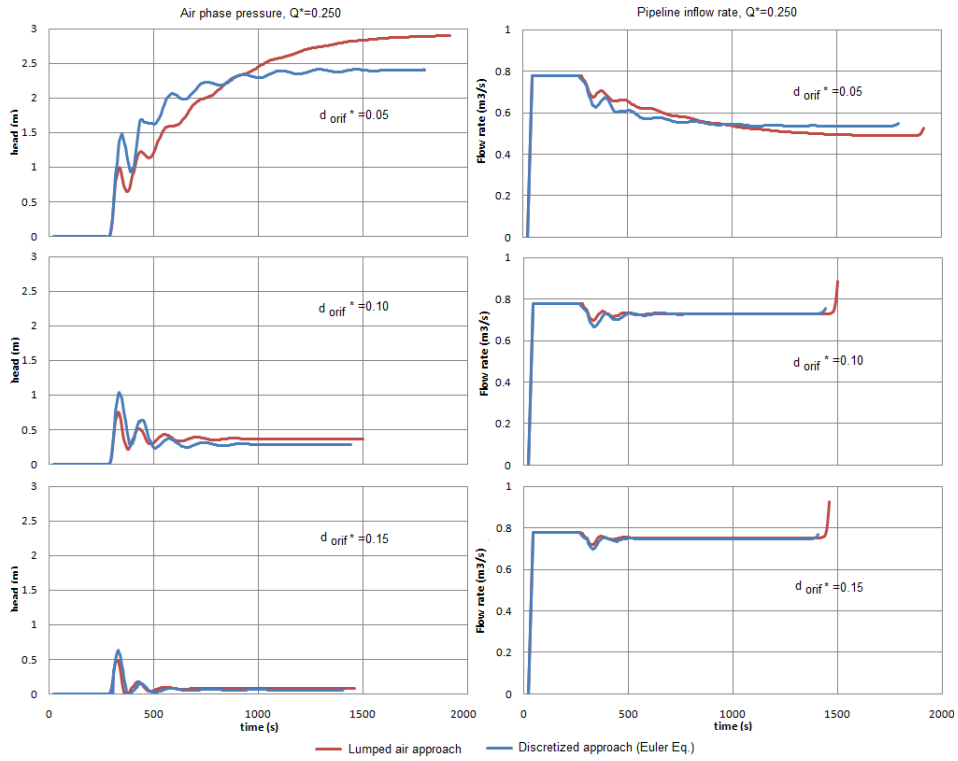

Figure 5.12: Comparison of heads at the ventilation orifice for $Q^* = 0.250$

Figure 5.14 shows the air velocity at the upstream end of the pipe (inside the pocket, not through the ventilation orifice) for all three flow rates tested and $d^*_{orif} = 0.15$. In those figures it can be noticed that for higher flow rates, and therefore higher pressures as seen in figures 5.11 to 5.13, the air velocity was higher, as it would be expected. Values in figure 5.14 are negative because of the adopted referential, which is positive in the downstream direction and negative to upstream. The magnitudes of the observed velocity oscillations seem exaggerated and are possibly caused by a limitation on how this phase is represented in the numerical code.

The pressure history at $x = 500m$ for $d^*_{orif} = 0.05$ is shown in figure 5.15. In this figure it can be seen that while the connection was not filled the pressure at that point is zero, raising to a small value after air pressurization starts (connection is filled). After that the pressure rose abruptly when the returning bore reaches that point, rising steadily later until the pipeline is filled, being this rising more pronounced for larger rates.

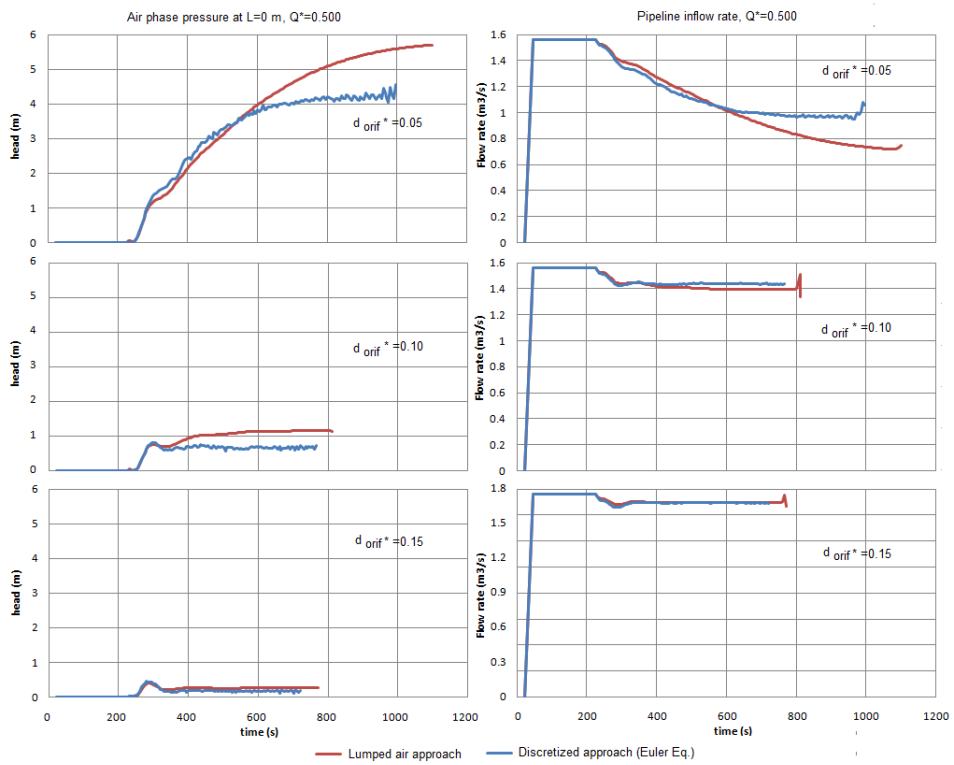

Figure 5.13: Comparison of heads at the ventilation orifice for $Q^* = 0.500$

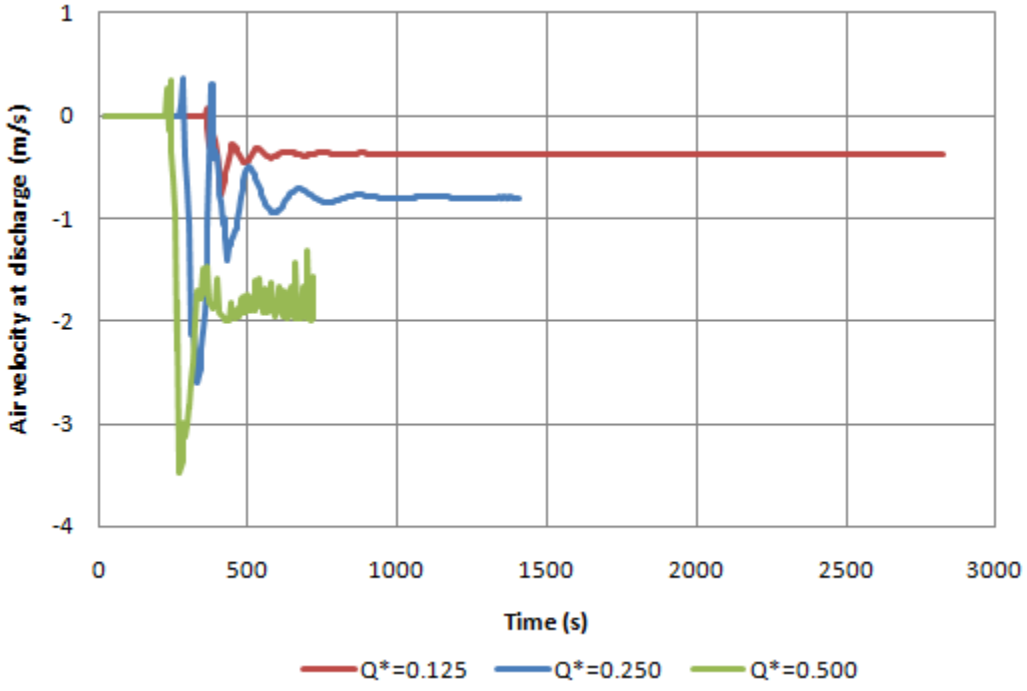

Figure 5.14: Air velocities predicted using Euler equations model for all three Q^* and $d^*_{orif} = 0.15$

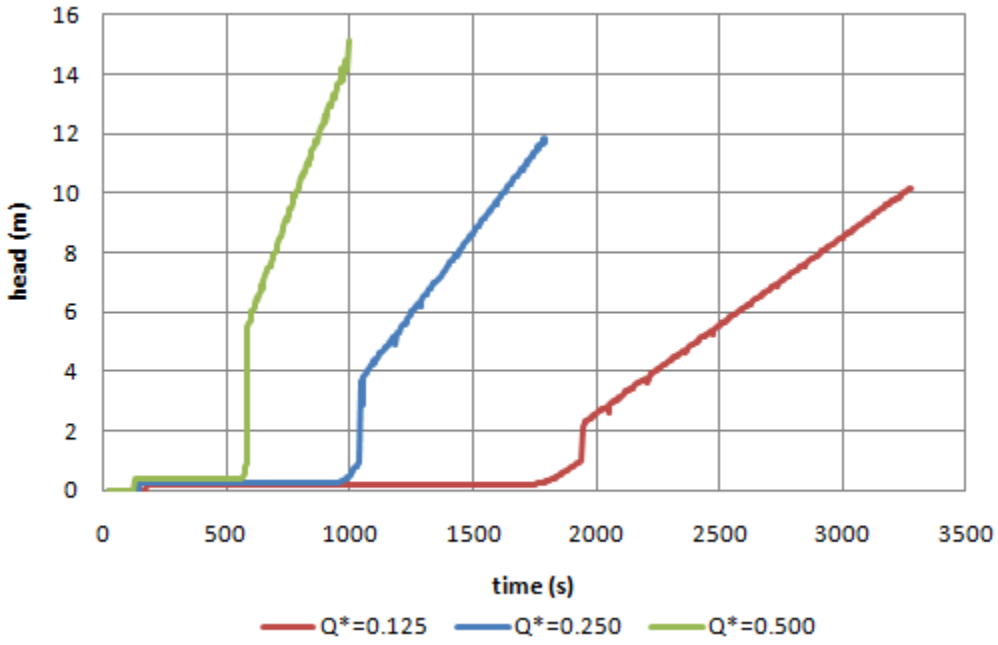

Figure 5.15: Pressure history at $x = 500m$ for $d^*_{orif} = 0.05$

5.3 Second version of TPAir

In the second and final version of the model, the calculations of the air phase downstream boundary condition in the Euler equations model are performed by assuming $b_{vel} = 0$ (section 4.3.2, equations 4.37 and 4.38) and using the source terms described in equation 4.32. With this modification the continuity errors decreased considerably and the code became more stable.

5.3.1 Comparison between experimental results and numerical model predictions

The comparison between experimental results presented in section 5.1 and corresponding numerical predictions is presented in Figures 5.16, 5.19 and 5.20. All comparison were performed assuming that the PVC pipeline Manning roughness coefficient was n=0.0085, and the wave celerity assumed for the PVC pipe was 200 m/s.

Pressure head predictions by the model for all the tested cases that resulted in air pressurization for 0.5% slope are compared with experimental results in Figure 5.16. Both Euler and UAPH approaches models showed good agreement with experimental data for most of the cases, specially for the lower flow rates ($Q^* = 0.245$ and $Q^* = 0.368$). In some of the numerical predictions there were non-physical, high-frequency oscillations on the air pressurization results as the pocket volume shrank to zero. Results obtained in the intermediate point ($x^* = 0.39$ measured from the knife gate valve) for the same slope are presented in Figure 5.19, and indicate fair agreement between numerical and experimental results. There is a tendency of the numerical model to anticipate the arrival of the pressurization front at the station, which results in the early jump in the pressure results. However, in general the predicted pressure increase over time matched what was measured by the transducers.

Another issue with the numerical predictions was linked to interface breakdown occurrences. The proposed numerical model (both air phase model implementations) was able to predict the onset of the interface breakdown as the interaction of the depression wave

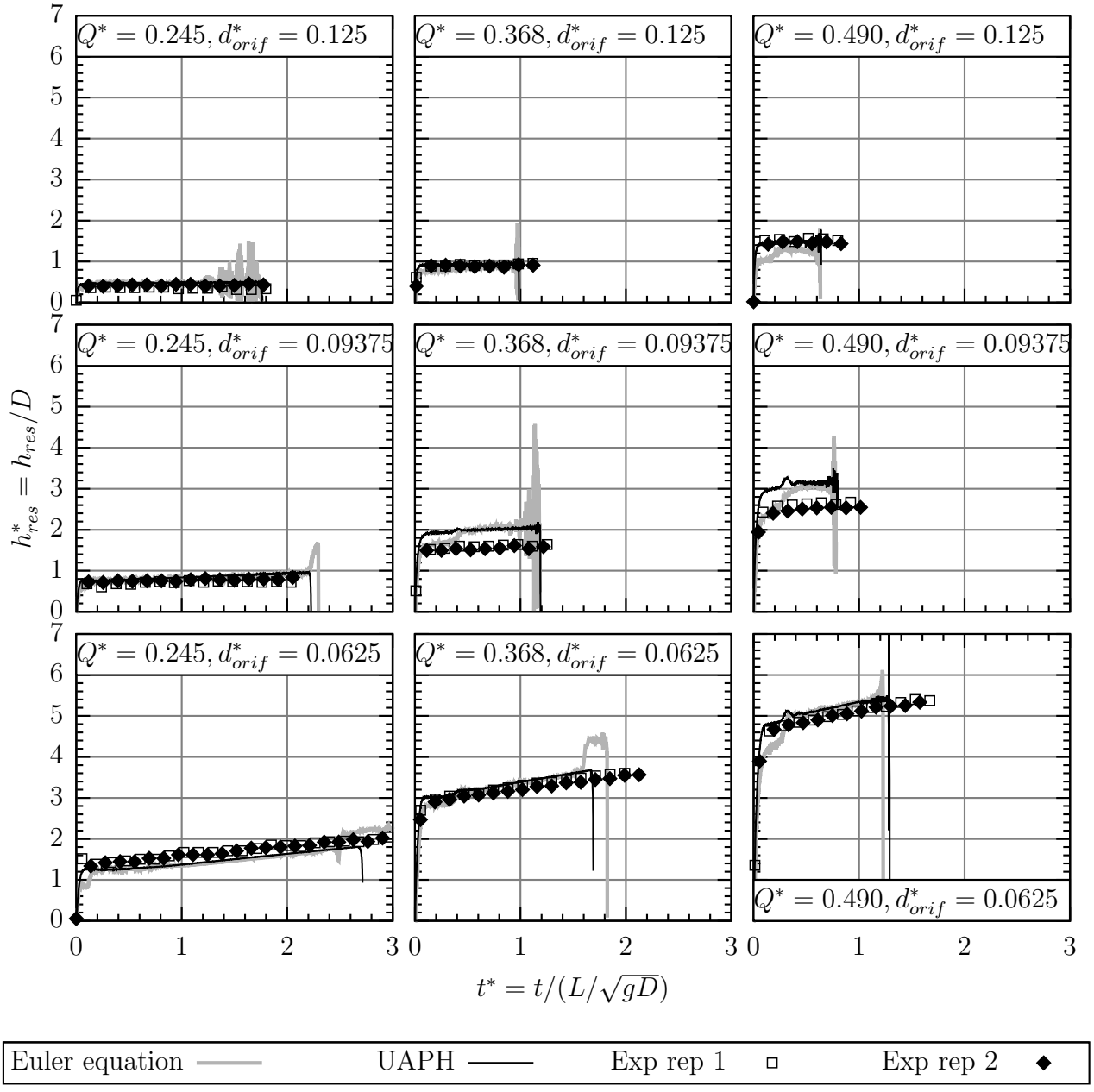

Figure 5.16: Experimental and predicted pressures at the ventilation orifice for all tested cases with slope of 0.5%

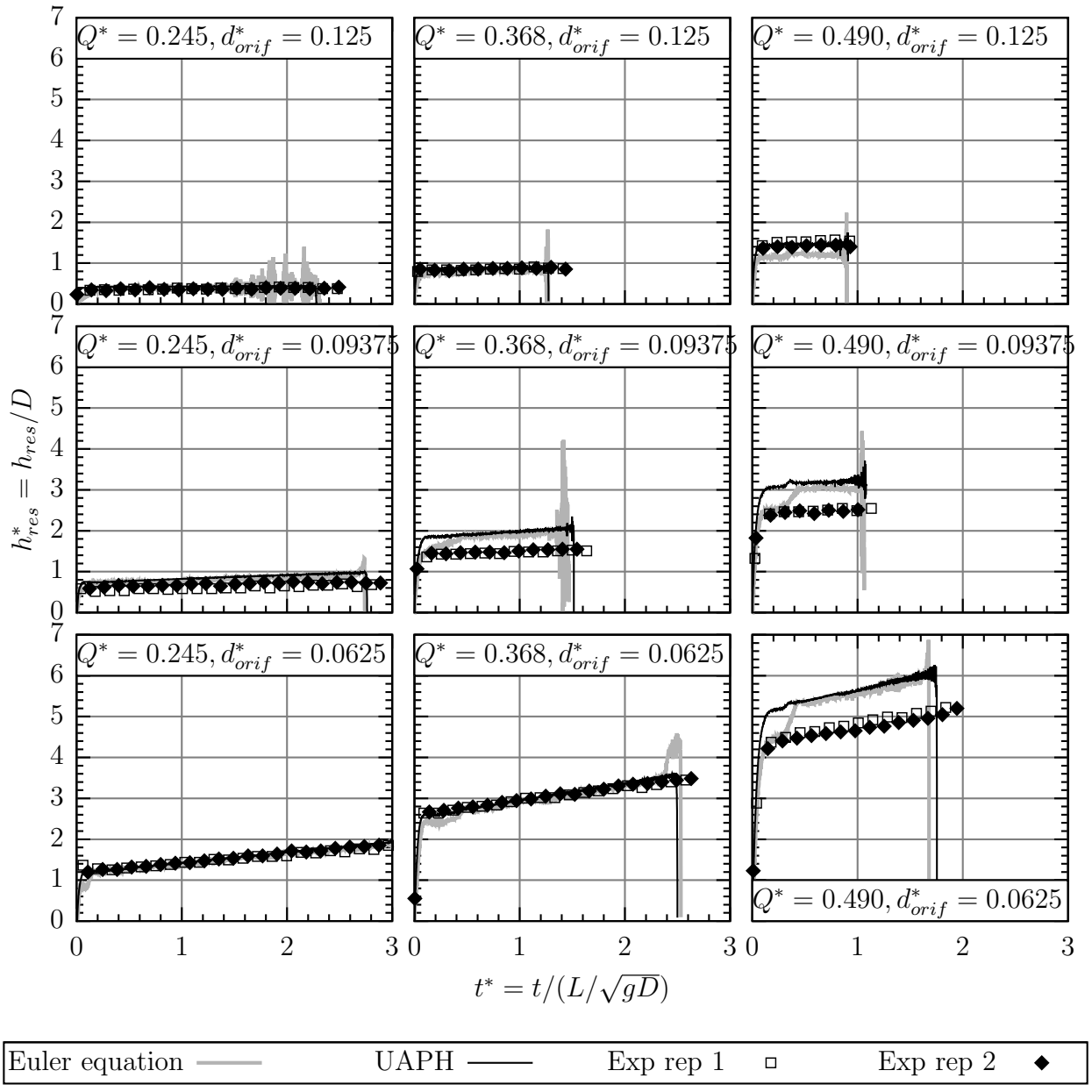

Figure 5.17: Experimental and predicted pressures at the ventilation orifice for all tested cases with slope of 1.0%

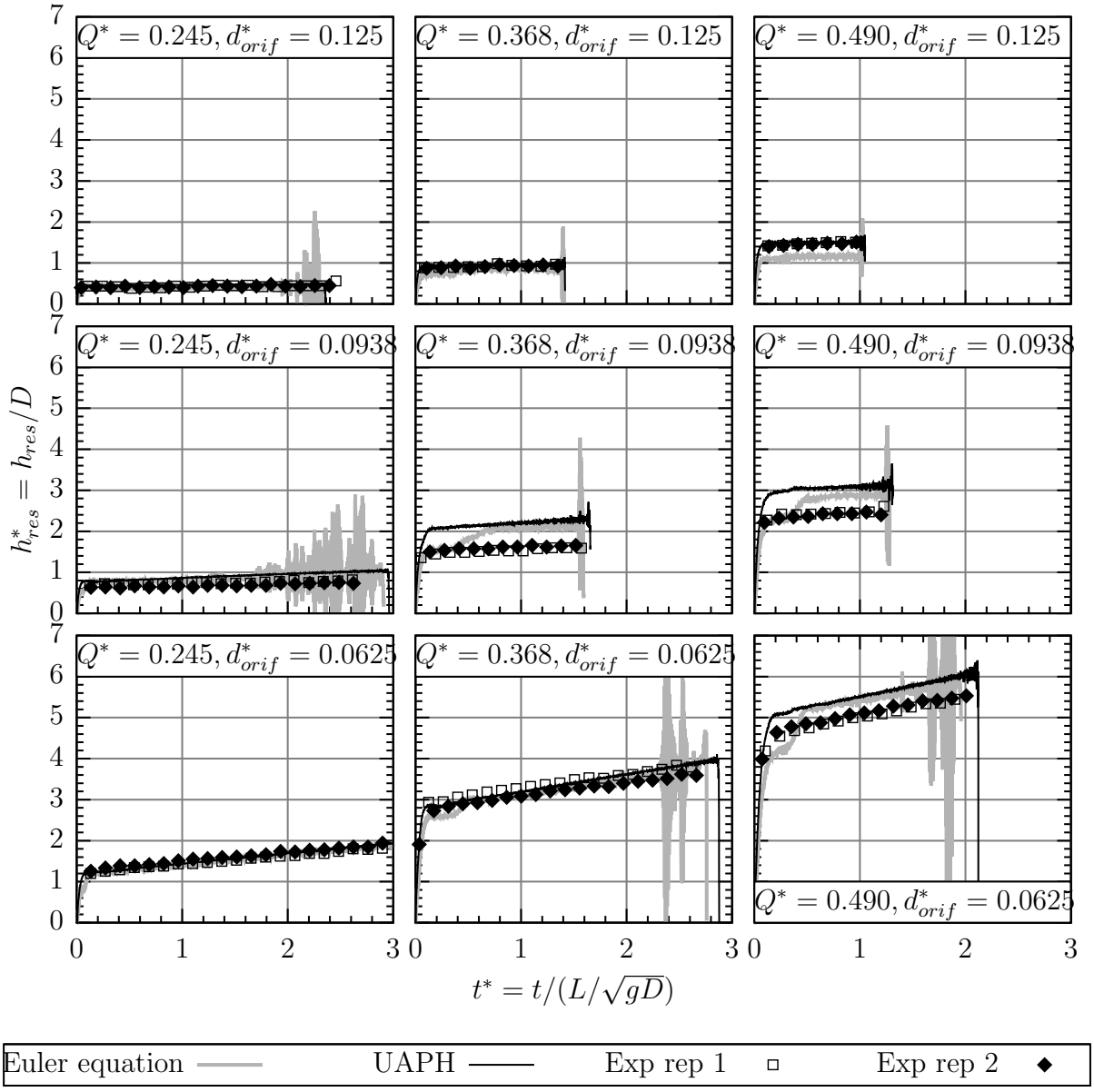

Figure 5.18: Experimental and predicted pressures at the ventilation orifice for all tested cases with slope of 2.0%

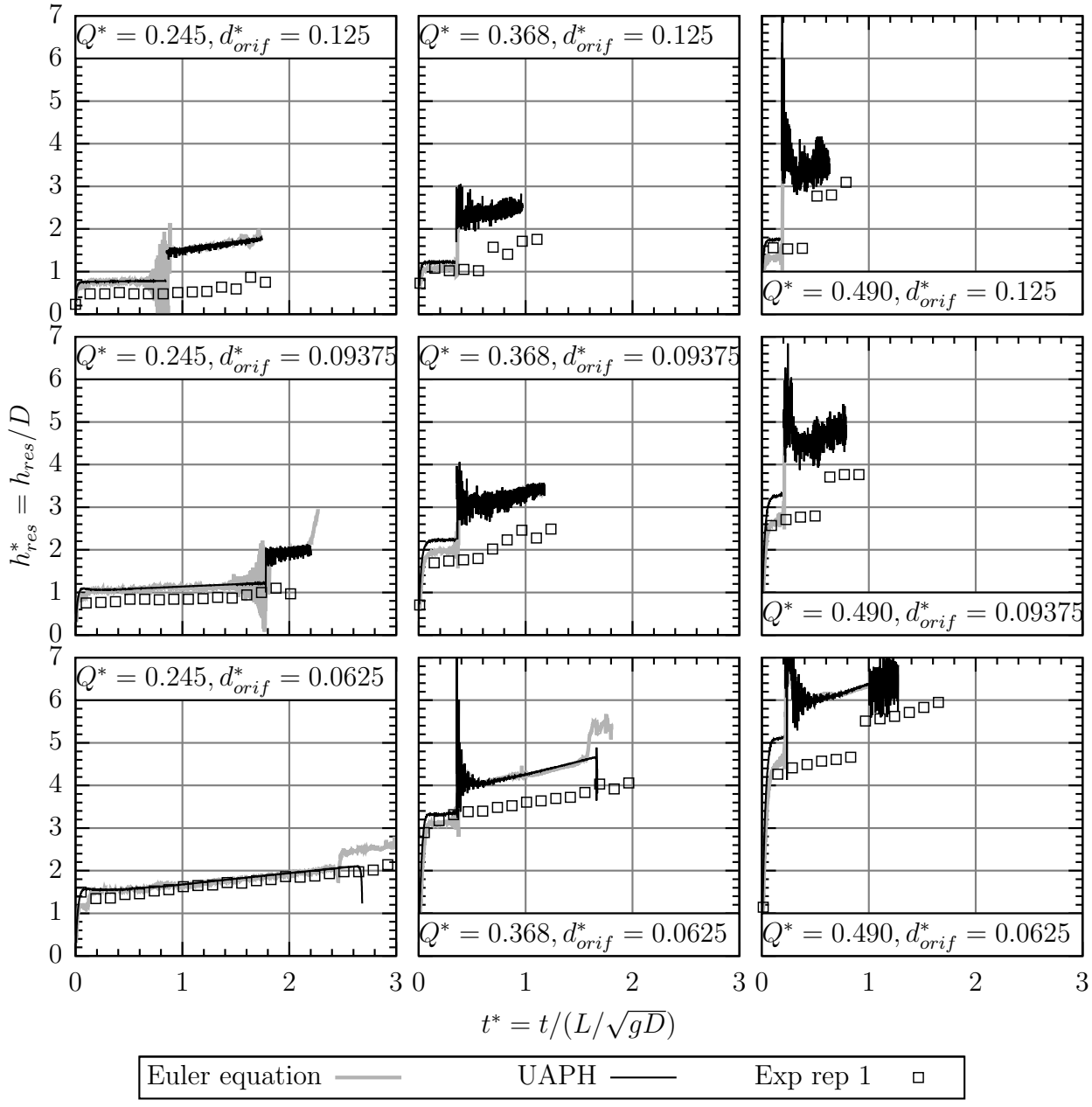

Figure 5.19: Experimental and predicted pressures at $x^* = 0.39$ (from downstream valve) for all tested cases with slope of 0.5%

and pipe filling bore resulted in an open channel bore. Unlike the experiments, the predicted pressurization front does not retreat following the breakdown. There was a slight over-prediction of the pressure head in cases when interface breakdown occurred; results obtained with Euler equation indicate the instant of the breakdown by a second, smaller increase in pressure head at $t^* \approx 0.2$. This discrepancy, however, was not significant and has not compromised the general accuracy of the numerical model.

Figure 5.20 contains a comparison between experimental results and numerical predictions of the pressure head variation at the upstream reservoir during the filling events for cases with 0.5% slope. One notices generally good agreement between experimental and numerical results. The reservoir discharge point within the pipeline was in free surface flow regime until the arrival of the backward moving pressurization interface. One recalls that prior to the knife gate valve closure, the reservoir head was steady. Considering that the inflow rate into the reservoir was constant, the increase in reservoir head following the knife gate valve maneuver indicates a drop in the inflow rate admitted into the pipeline due to the almost instantaneous air pressurization. Steeper reservoir pressure head increase is linked to stronger air pressurization, and the drop in flow rate resulted in the depression wave which trigged interface breakdown events. Error bars plotted in Figure 5.20 reflect the accuracy of the manometer used in the experiments ($\pm 0.01m$).

It can be observed that both models yielded similarly accurate results when compared to experimental data despite the two considerably different approaches to simulate air phase. An aspect to be considered is the computational effort involved in each air phase modeling alternative. In general, the simulation time using the Euler equation model was over 9 times larger than one required by the UAPH model approach for the comparison with the experimental results. Not only due to the additional model complexity, but the enforcement of the Courant condition for the air phase simulation using resulted in even smaller time steps as the celerity of the air phase was in the order of 300 m/s.

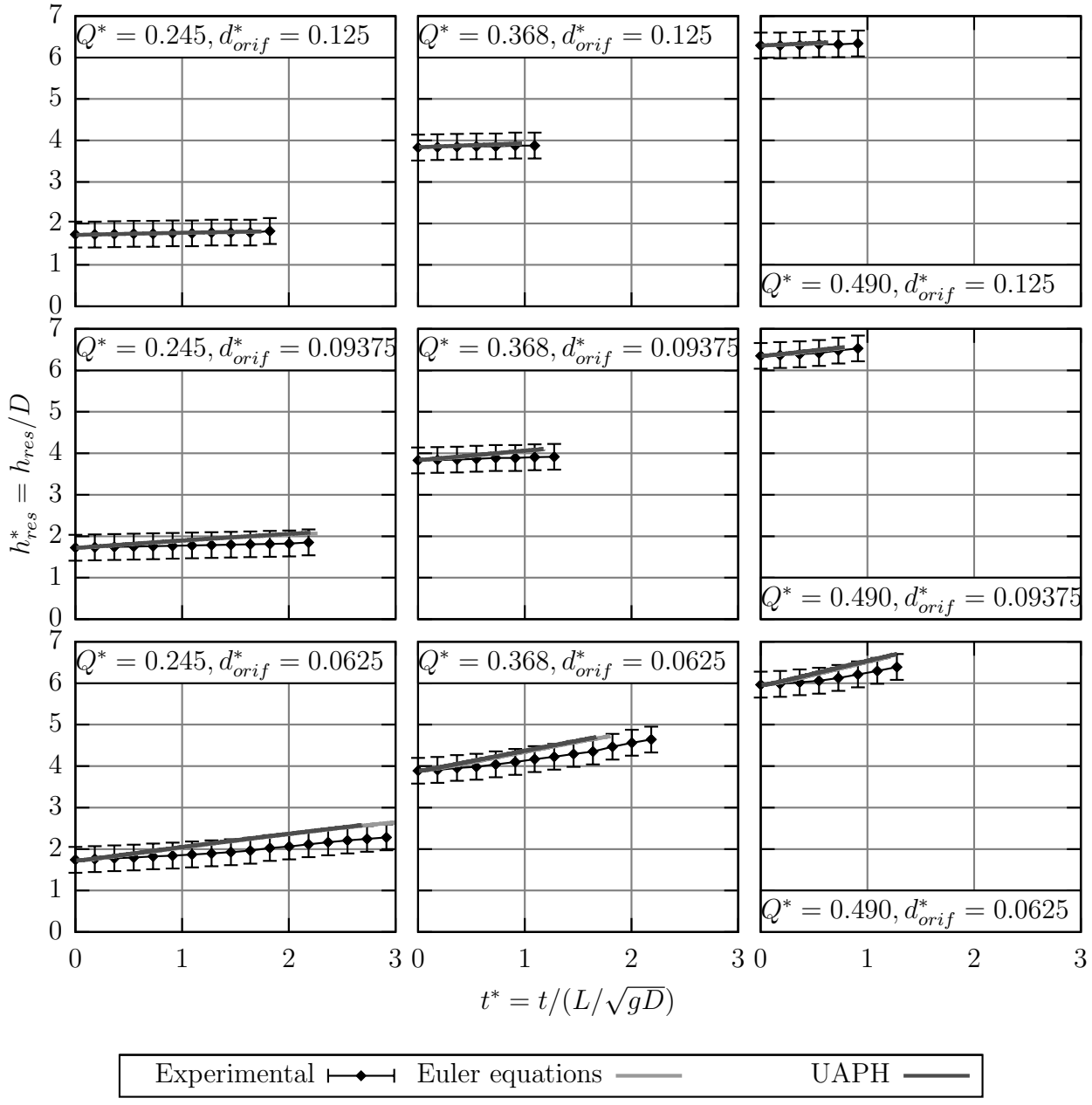

Figure 5.20: Experimental and predicted reservoir heads for all tested cases with slope of 0.5%

Another aspect to be considered is the continuity error for the air phase. The Euler equation model had an average continuity error of 7.97%, while the UAPH model had 0%. The likely source of the continuity error for the Euler equation model are the orifice boundary condition and the limitation of the correction factor ϕ (equation 4.32) to a certain value, which distorts the actual required air compression due to pocket vertical shrinking. However, this continuity error does no seem to affect the final pressure results, as a link between this error and a higher discrepancy between model and experimental results could not be established in table 5.4 and figures 5.16 to 5.19.

Both models had close average percentages of the total initial air volume expelled before calculations stopped (stop criteria of an one cell air pocket or crash), which were 98.3% of the initial air for the Euler equations model and 96.5% for the UAPH. However, this value was less than 90% for three cases with the UAPH model, which was considered as an issue of early simulation stop, while Euler equation model had the index above 90% for all the cases. Also, 50% of the UAPH model simulations stopped due to crash close to the simulation end, while only 11 % of the cases for the Euler equations had this problem. However, the oscillations at the end of the simulations with the Euler equations model might have caused the second water cell to touch the crown of the pipe, causing an air pocket of one cell length and thus causing the stop criteria to be prematurely triggered.

Parameters			Euler					UAPH				
S (%)	Q (GPM)	d_{orif} (in)	Physical time (s)	Computational time (s)	Filled Air vol. (%)	Cont. error (%)	Jump Position (m)	Physical time (s)	Computational time (s)	Filled Air vol. (%)	Cont. error (%)	Jump Position (m)
0.5	40	0.250	100.8	656	99.3	1.913	1.90	89.4	46	66.3	0	7.91
0.5	40	0.375	84.9	363	97.8	3.656	3.95	84.2	34	92.6	0	3.74
0.5	40	0.500	79.1	254	98.3	2.706	1.03	79.1	28	99.1	0	0.22
0.5	40	2.000	78.0	248	97.6	0.416	0.60	78.1	27	99.2	0	0.32
0.5	60	0.250	79.8	297	93.3	6.609	5.58	78.3	29	82.1	0	5.42
0.5	60	0.375	72.8	187	97.1	3.306	0.54	72.9	21	98.6	0	0.22
0.5	60	0.500	70.7	136	98.2	6.13	0.32	70.7	20	98.8	0	0.16
0.5	60	2.000	69.8	120	98.4	8.26	0.27	69.7	17	98.9	0	0.16
0.5	80	0.250	73.3	165	92.4	8.768	4.44	74.0	25	92.4	0	2.33
0.5	80	0.375	68.5	156	98.0	8.808	0.27	68.6	18	98.6	0	0.16
0.5	80	0.500	66.9	93	98.3	12.296	0.22	66.9	17	98.5	0	0.16
0.5	80	2.000	66.3	81	98.6	12.352	0.16	66.2	13	98.5	0	0.16
1.0	40	0.250	107.0	652	100.0	4.953	0.22	103.3	57	88.1	0	3.84
1.0	40	0.375	89.7	417	98.7	6.141	2.17	90.0	41	96.9	0	1.95
1.0	40	0.500	85.1	339	98.7	5.837	1.08	84.8	35	98.9	0	0.70
1.0	40	2.000	83.2	308	97.6	2.053	0.65	83.4	33	98.9	0	0.76
1.0	60	0.250	87.5	357	98.7	7.586	2.33	87.1	43	92.6	0	2.60
1.0	60	0.375	75.9	245	98.9	7.786	0.32	76.4	25	99.3	0	0.16
1.0	60	0.500	73.9	172	98.7	5.574	0.32	73.8	21	99.2	0	0.16
1.0	60	2.000	72.1	149	98.8	7.977	0.27	72.0	18	99.2	0	0.16
1.0	80	0.250	78.2	226	99.2	11.17	1.68	79.0	29	97.7	0	0.70
1.0	80	0.375	71.5	195	98.6	8.68	0.27	71.7	22	98.9	0	0.16
1.0	80	0.500	69.8	127	98.7	11.804	0.22	69.9	19	98.9	0	0.16
1.0	80	2.000	68.8	110	98.9	12.723	0.16	68.7	16	98.8	0	0.16
2.0	40	0.250	111.1	653	100.0	4.956	0.22	110.0	63	94.8	0	1.84
2.0	40	0.375	91.6	418	98.2	6.796	0.97	92.1	41	98.5	0	0.97
2.0	40	0.500	85.2	317	98.4	6.551	0.92	85.6	33	99.5	0	0.16
2.0	40	2.000	83.6	299	98.6	3.698	0.43	83.6	35	100.0	0	0.27
2.0	60	0.250	89.9	372	99.1	10.585	1.41	91.2	42	97.1	0	1.14
2.0	60	0.375	77.3	272	99.5	11.902	0.16	78.0	28	99.4	0	0.16
2.0	60	0.500	75.3	196	98.9	9.017	0.27	75.4	23	99.3	0	0.16
2.0	60	2.000	73.6	169	99.0	11.426	0.22	73.5	21	99.3	0	0.16
2.0	80	0.250	81.2	415	97.4	12.85	1.14	83.0	34	98.5	0	0.49
2.0	80	0.375	73.9	239	98.8	10.599	0.27	74.3	24	99.1	0	0.16
2.0	80	0.500	71.2	145	98.9	15.379	0.22	71.4	20	99.0	0	0.16
2.0	80	2.000	70.6	131	99.1	15.669	0.16	70.5	18	99.0	0	0.16

Table 5.4: Summary of results of both models

5.3.2 Model comparison with actual pipeline filling event

The comparisons between the field data and the numerical predictions for the filling of CAESB ductile iron pipeline are presented below in Figures 5.22 to 5.24. This 350 mm diameter transmission main has a pump station, and the filling process occurs in two steps. In the first step, the initial 4.4-km extension line is filled by gravity, throttling the upstream butterfly valve so that the inflow rate is limited to $Q^* = 0.18$. In the second step, pumps are turned on and the remainder 2.8 km of the pipeline is filled. The analysis below focuses in simulation of the initial 1,700 meters of the gravity filling. The air valves positioned at x=400 m correspond to a couple of 50-mm, spherical shutter air release valves. The actual discharge area of these valves was not measured, and was calibrated in the numerical model so that the observed air pressure at the discharge point was approximately similar to the measurements.

The pipeline profile is shown 5.21, and the assumed values for the Manning roughness was $n = 0.011$ and for the celerity was 100 m/s. While the anticipated celerity is much larger, the adopted value is adequate considering that the modeling is not focusing on transient pressure issues but instead on pipeline filling. Moreover, the larger celerity helped limit the computational effort for the simulations.

The work by [Vasconcelos et al., 2009b] applied the TPA model that did not incorporate effects of air pressurization to simulate pipeline filling. Figure 5.22 presents a comparison of the pressure head hydrograph measured downstream from the pump station ($x \approx 380m$), and the sample frequency was 4 seconds. One notices that the field measurement signal an increase in the pressure head at about 200 seconds into the simulation and attains a stable level. At about $t > 1100$ s the pressure begins to steadily rise again and will arrive at 8 m when $t > 2700$ s. The results obtained with the traditional TPA model indicate a small pressure (corresponding to the water depth) until about $t = 2300$ s, when the pressure rapidly climbs achieving levels over 7.5 m after $t = 3500$ s. The results obtained with both the proposed model better approach the field measurements. Pressure begins to climb at

t=500 seconds, and will arrive at 8.0 m for T=2900 seconds (Euler equation model). The UAPH model presents fairly good agreement too, but at $t = 1700$ s it begins to diverge from the solution obtained with the Euler equation, and pressure will attain the 8.0 m only for $t = 3500$ s.

An analogous comparison, this time however focusing on the measured and predicted inflow rate admitted into the pipeline, is presented in Figure 5.24. Flow measurements in the water main were performed with an electromagnetic flow meter, with a sampling frequency of 1 minute. The butterfly valve opening was gradual, and took approximately 4 minutes. The simulation performed with the traditional TPA model (presented in [Vasconcelos et al., 2009b]) reproduced this gradual opening; the results presented here have skipped this for simplicity, assuming the final opening right on the onset of simulation. Flow measurement indicate an initial flow rate slightly above 40 L/s, which will start declining for $t > 1600$ s, stabilizing in 29 L/s when t=2700 seconds. Assuming that the flow rate drop is caused by air pressurization (as in the case of the experiments performed in this study), there seems to be a slight inconsistency with the pressure measurements which indicate that pressure begins to climb when for $t > 1200s$. The cause for this possible inconsistency is not determined. The numerical prediction by the TPA model indicate that the flow rate drop will occur much later, whereas the proposed model indicate the flow rate drop occurring much sooner, as soon as air pressure begins to climb in the pipeline.

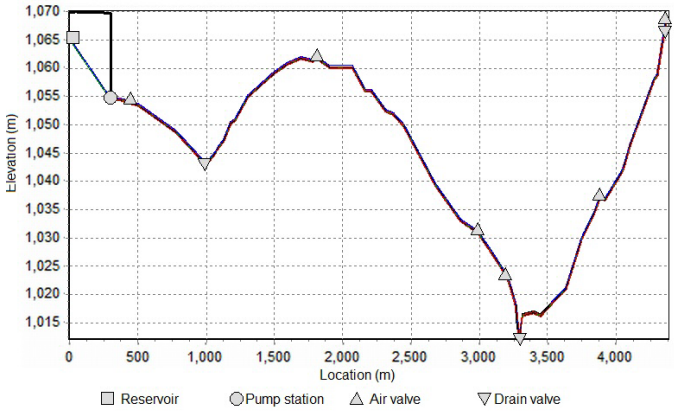

Figure 5.21: Real water main's sketch

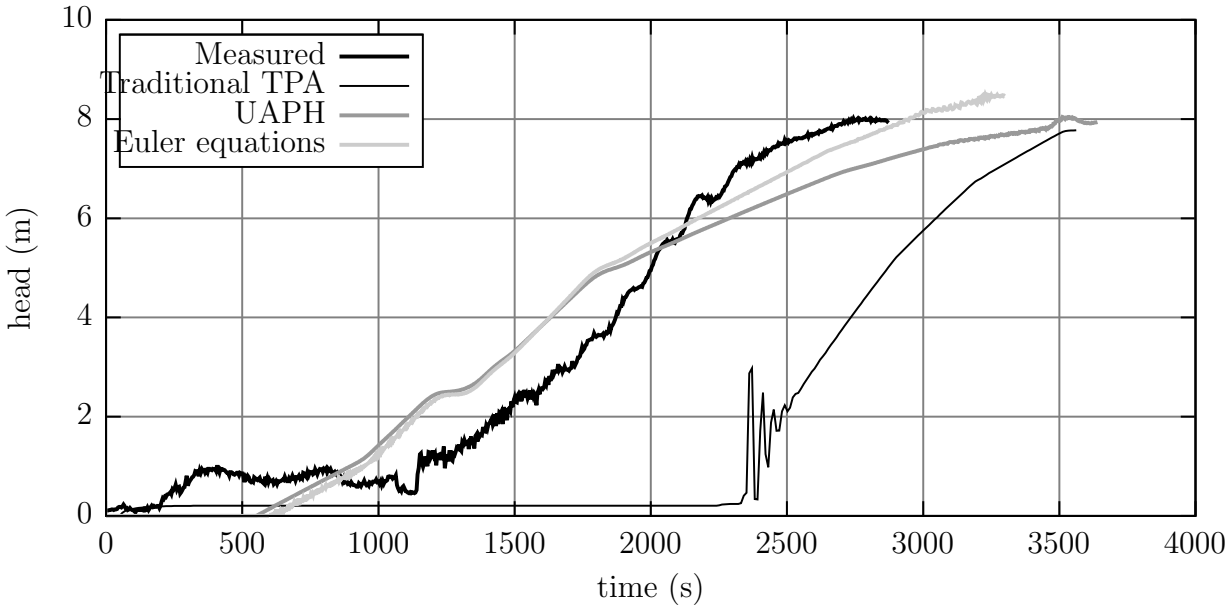

Figure 5.22: Field measurements and predicted heads at the upstream ventilation valve of the water main

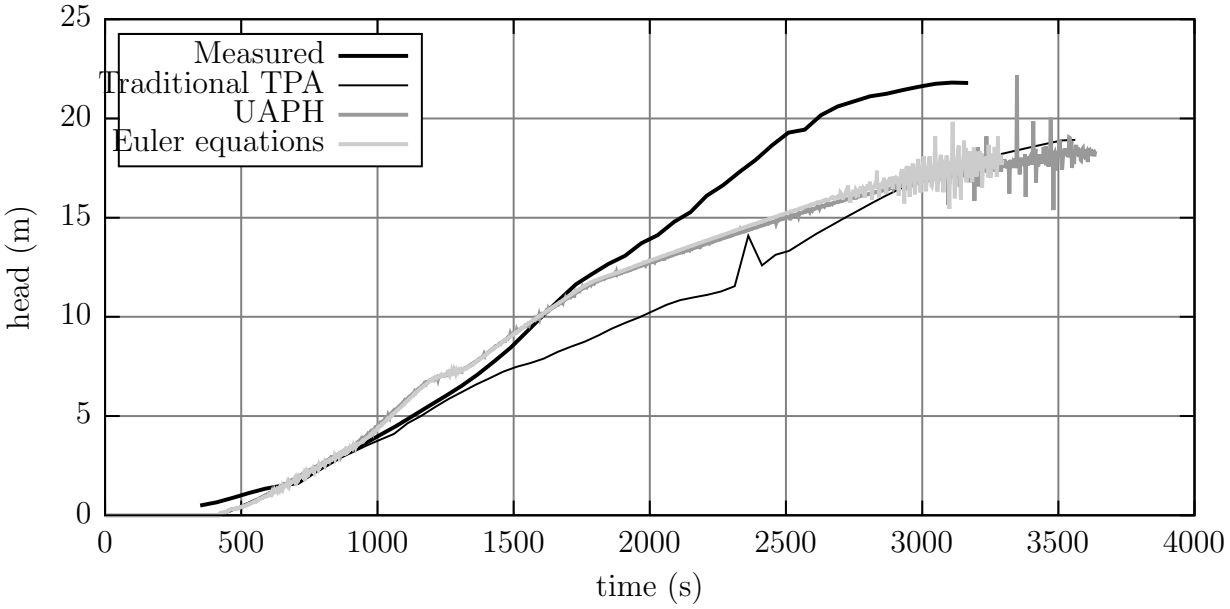

Figure 5.23: Field measurements and predicted heads at the downstream ventilation valve of the water main

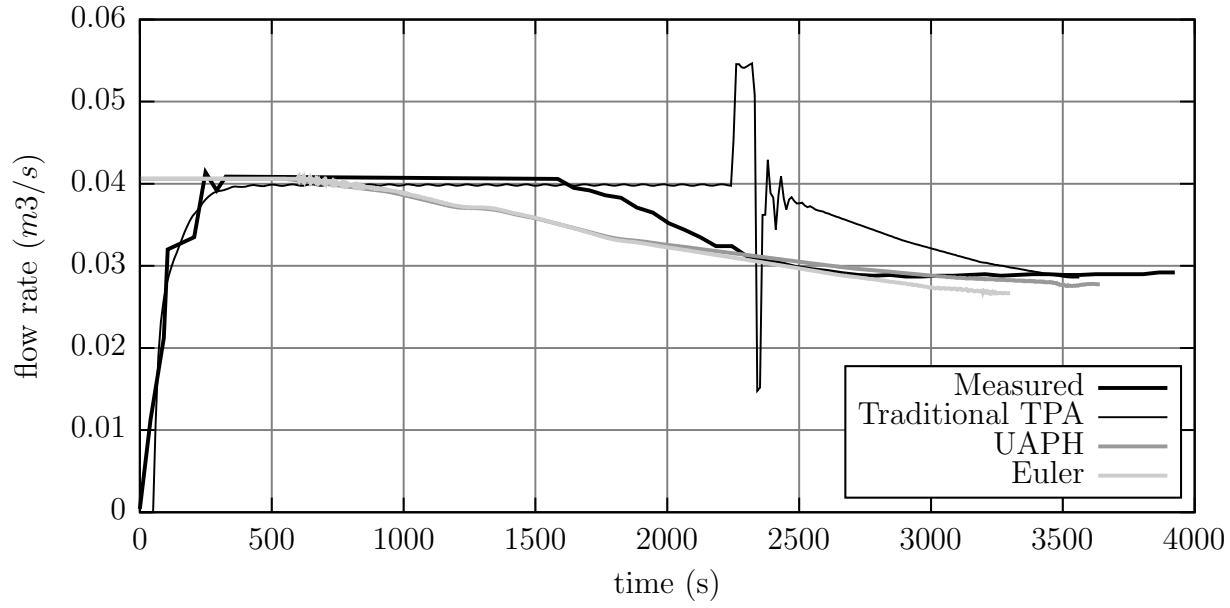

Figure 5.24: Field measurements and flow rates at the upstream ventilation valve of the water main

5.4 Conclusion

This work presented two model alternatives for the modeling of the filling of a water main, together with experimental investigations on the subject with a scale model. Several numerical models have been developed to simulate this problem, however each of them with certain limitations which prevent most of them to be used for practical applications. Also, published data for the expelling of air pockets through an air valve during a refilling process is limited.

This work presented results from a proposed model that couples the Saint-Venant equations and the Euler equations to simulate the filling of water mains accounting for air pressurization. The idea was to better simulate pressure gradients in the air phase, and with this be able to predict the filling events with greater accuracy. While examples presented for the first version of the model were not a precise depiction of the conditions anticipated during water main filling, it served to illustrate the importance of incorporating air pressurization in the computations of water main filling with limited ventilation. Also, it was noted that for the simulation of this type of problem, especially when interface breakdown occurs, the model must account variations in the cross sectional area of the air flow.

With this, the second version of the models incorporated a more sophisticated mathematical model based the Euler equations for the air phase, allowing for variable cross sectional area as well as for air frictional losses. In the second version, both presented numerical models (Euler equations and UAPH approaches) successfully predicted the pressures heads and flow rates for laboratory and field data, which showed both model's capacity of simulating typical engineering actual conditions. Both models were also able to predict the occurrence of different flow features such as interface breakdown and interaction between bores and depression waves. Also, a comparison between both approaches with actual experimental results showed that, for the range of tested cases in the laboratory as well as for the actual water main case, the UAPH approach can be used instead of the Euler equations model

with no significant loss of precision and with a gain in implementation simplicity and computational effort. Still, the UAPH model had more crashes and early stops than the Euler equations model, which may prevent certain cases to be properly simulated with UAPH. Improvements still need to be done to account better for the occurrence of interface breakdown and drown inlets, which still cause non physical results. Also functionalities to account for air pocket movement (dragging and flotation) need to be incorporated.

An experimental investigation was performed varying common actual operation parameters, which are the inlet flow rate, pipe slope, and ventilation size. With the results of this investigation, data was provided to calibrate/assess the proposed models and also other researcher's models still to be developed. A comprehensive analysis of what was observed in the experimental data was also included, clarifying events and features of this type of flow, such as interface breakdowns.

Experimental and numerical results show the importance that ventilation design has on the maximum pressures observed in a system. A considerable increase in the maximum pressure in the system together with a increase in the filling time was observed if ventilation is smaller than adequate. Experiments also showed the sequence of events leading to an interface breakdown in a supercritical filling event, which is:

1. Air pressure increase due to the formation of an air pocket;
2. Inflow rate decreases generating a depression wave; and
3. This depression wave intercepts the pressuring bore and, if strong enough, causes the interface breakdown to happen.

The two main scientific contributions of this work were:

1. Development of a feasible modeling framework to simulate the filling of water mains accounting for air effects; and

2. Demonstration that lumped approach for air phase modeling (UAPH) has comparable accuracy with discretized model based on Euler equations at a much reduced computational effort.

The suggested follow ups working on this topic are:

- Modification on the modeling frameworks to account for air pocket flotation and dragging;
- More generic model implementation to make it possible the simulation more realistic problems with complex geometries and several air pockets;
- Consideration of a wider range of air pocket formation mechanisms; and
- Development of wider range of anticipated boundary conditions in water main filling events; and
- Development of a coupled numerical solution for Euler and Saint Venant equations, possibly based on the HLL Riemann solver.

Bibliography

[Akan, 2006] Akan, A. (2006). *Open channel hydraulics*. Butterworth-Heinemann.

[Arai and Yamamoto, 2003] Arai, K. and Yamamoto, K. (2003). Transient analysis of mixed free-surface-pressurized flows with modified slot model 1: Computational model and experiment. In *Proc. FEDSM03 4th ASME-JSME Joint Fluids Engrg. Conf. Honolulu, Hawaii, Paper*, volume 45266.

[Benjamin, 1968] Benjamin, T. B. (1968). Gravity currents and related phenomena. *Journal of Fluid Mechanics*, 31(02):209–248.

[Bentley, 2010] Bentley, S. (2010). Hammer.

[Bourdarias and Gerbi, 2007] Bourdarias, C. and Gerbi, S. (2007). A finite volume scheme for a model coupling free surface and pressurised flows in pipes. *Journal of Computational and Applied Mathematics*, 209(1):109–131.

[Capart et al., 2003] Capart, H., Eldho, T., Huang, S., Young, D., and Zech, Y. (2003). Treatment of natural geometry in finite volume river flow computations. *Journal of Hydraulic Engineering*, 129:385.

[Capart et al., 1997] Capart, H., Sillen, X., and Zech, Y. (1997). Numerical and experimental water transients in sewer pipes. *Journal of hydraulic research*, 35(5):659–672.

[Chaiko and Brinckman, 2002] Chaiko, M. and Brinckman, K. (2002). Models for analysis of water hammer in piping with entrapped air. *Journal of fluids engineering*, 124:194.

[Chaudhry, 2008] Chaudhry, M. (2008). *Open-channel flow*. Springer Verlag.

[Cunge and Wegner, 1964] Cunge, J. and Wegner, M. (1964). Intégration numérique des équations d'écoulement de barré de saint-venant par un schéma implicite de différences finies. *La Houille Blanche*, (1):33–39.

[Cunge et al., 1980] Cunge, J. A. et al. (1980). *Practical Aspects of Computational River Hydraulics*. Pitman Advanced Pub. Program.

[De Martino et al., 2008] De Martino, G., Fontana, N., and Giugni, M. (2008). Transient flow caused by air expulsion through an orifice. *Journal of Hydraulic Engineering*, 134:1395.

[Fabre and Liné, 1992] Fabre, J. and Liné, A. (1992). Modeling of two-phase slug flow. *Annual review of fluid mechanics*, 24(1):21–46.

[Falvey, 1980] Falvey, H. (1980). Air-water flow in hydraulic structures. *NASA STI/Recon Technical Report N*, 81:26429.

[Fuamba, 2002] Fuamba, M. (2002). Contribution on transient flow modelling in storm sewers contribution sur la modélisation de lâ[U+0080][U+0099]écoulement transitoire dans les collecteurs. *Journal of hydraulic research*, 40(6):685.

[Fuertes et al., 2000] Fuertes, V., Arregui, F., Cabrera, E., and Iglesias, P. (2000). Experimental setup of entrapped air pockets model validation. In *BHR GROUP CONFERENCE SERIES PUBLICATION*, volume 39, pages 133–146. Bury St. Edmunds; Professional Engineering Publishing; 1998.

[Godunov, 1959] Godunov, S. (1959). A difference method for numerical calculation of discontinuous solutions of the equations of hydrodynamics. *Matematicheskii Sbornik*, 89(3):271–306.

[Gómez and Achiaga, 2001] Gómez, M. and Achiaga, V. (2001). Mixed flow modelling produced by pressure fronts from upstream and downstream extremes. In *Urban Drainage Modeling*, pages 461–470. ASCE.

[Guinot, 2003] Guinot, V. (2003). *Godunov-type schemes: an introduction for engineers*, volume 1. Elsevier Science.

[Hamam and McCorquodale, 1982] Hamam, M. and McCorquodale, J. (1982). Transient conditions in the transition from gravity to surcharged sewer flow. *Canadian Journal of Civil Engineering*, 9(2):189–196.

[Harten et al., 1983] Harten, A., Lax, P., and Van Leer, B. (1983). On upstream differencing and godunov-type schemes for hyperbolic conservation laws. *SIAM review*, pages 35–61.

[Issa and Kempf, 2003] Issa, R. and Kempf, M. (2003). Simulation of slug flow in horizontal and nearly horizontal pipes with the two-fluid model. *International journal of multiphase flow*, 29(1):69–95.

[Izquierdo et al., 1999] Izquierdo, J., Fuertes, V., Cabrera, E., Iglesias, P., and Garcia-Serra, J. (1999). Pipeline start-up with entrapped air. *Journal of hydraulic research*, 37(5):579–590.

[Kabiri Samani et al., 2006] Kabiri Samani, A., Borghei, S., and SAEIDI, M. (2006). Entrapped air in long water tunnels during transition from a pressurized to free-surface flow regime. *Scientia Iranica*, 13(2):174–186.

[Kalinske and Bliss, 1943] Kalinske, A. and Bliss, P. (1943). Removal of air from pipe lines by flowing water. *Proceedings of the American Society of Civil Engineers (ASCE)*, 13(10):3.

[Kerger et al., 2011] Kerger, F., Erpicum, S., Dewals, B., Archambeau, P., and Pirotton, M. (2011). 1d unified mathematical model for environmental flow applicated to aerated mixed flows. *Advances in Engineering Software*, 42(9):660–670.

[Krönig, 1856] Krönig, A. (1856). Grundzüge einer theorie der gase. *Annalen der Physik*, 175(10):315–322.

[KYPipe, 2010] KYPipe (2010). Pipe2010: Surge.

[León et al., 2009] León, A., Ghidaoui, M., Schmidt, A., and García, M. (2009). Application of godunov-type schemes to transient mixed flows. *J. Hydraulic Res*, 47(2):147–156.

[León et al., 2010] León, A., Ghidaoui, M., Schmidt, A., and García, M. (2010). A robust two-equation model for transient-mixed flows.

[León et al., 2006] León, A., Ghidaoui, M., Schmidt, A., Garcia, M., et al. (2006). Godunov-type solutions for transient flows in sewers. *Journal of Hydraulic Engineering*, 132:800.

[León et al., 2008] León, A., Ghidaoui, M., Schmidt, A., García, M., et al. (2008). Efficient second-order accurate shock-capturing scheme for modeling one-and two-phase water hammer flows. *Journal of Hydraulic Engineering*, 134:970.

[LeVeque, 1992] LeVeque, R. (1992). *Numerical methods for conservation laws*. Birkhauser.

[Li and McCorquodale, 1999] Li, J. and McCorquodale, A. (1999). Modeling mixed flow in storm sewers. *Journal of Hydraulic Engineering*, 125:1170.

[Liou and Hunt, 1996] Liou, C. P. and Hunt, W. A. (1996). Filling of pipelines with undulating elevation profiles. *J. Hydr. Engrg.*, 122(10):534–539.

[Macchione and Morelli, 2003] Macchione, F. and Morelli, M. (2003). Practical aspects in comparing shock-capturing schemes for dam break problems. *Journal of Hydraulic Engineering*, 129:187.

[Malekpour et al., 2011] Malekpour, A., BW, K., et al. (2011). Rapid filling analysis of pipelines with undulating profiles by the method of characteristics. *ISRN Applied Mathematics*, 2011.

[Martin, 1976] Martin, C. S. (1976). Entrapped air in pipelines. *Second BHRA International conference on pressure surges*.

[McCorquodale and Hamam, 1983] McCorquodale, J. and Hamam, M. (1983). Modeling surcharged flow in sewers. In *Proc., Int'l Symposium on Urban Hydrology, Hydraulics and Sediment Control, University of Kentucky, Lexington, Kentucky*, pages 331–338.

[McInnis and Karney, 1995] McInnis, D. and Karney, B. W. (1995). Transients in distribution networks: Field tests and demand models. *Journal of Hydraulic Engineering*.

[Politano et al., 2007] Politano, M., Odgaard, A., and Klecan, W. (2007). Case study: Numerical evaluation of hydraulic transients in a combined sewer overflow tunnel system. *Journal of Hydraulic Engineering*, 133:1103.

[Pothof and Clemens, 2010] Pothof, I. and Clemens, F. (2010). Experimental study of air-water flow in downward sloping pipes air-water flow in downward sloping pipes. *International Journal of Multiphase Flow*.

[Potter, 2004] Potter, M. C. (2004). *Mecânica dos Fluidos*. Thomson, 3 edition.

[Pozos et al., 2010] Pozos, O., Sanchez, A., Rodal, E., and Fairuzov, Y. (2010). Effects of water-air mixtures on hydraulic transients. *Canadian Journal of Civil Engineering*, 37(9):1189–1200.

[Preissmann, 1961] Preissmann, A. (1961). Propagation des intumescences dans les canaux et rivieres. In *First Congress of the French Association for Computation, Grenoble, France*, pages 433–442.

[Press, 1989] Press, W. (1989). *Numerical recipes in Pascal: the art of scientific computing*. Cambridge Univ Pr.

[Pulliam, 1994] Pulliam, T. H. (1994). The euler equations. Technical report, NASA Ames Research Center.

[Roe, 1981] Roe, P. (1981). Approximate riemann solvers, parameter vectors, and difference schemes. *Journal of computational physics*, 43(2):357–372.

[Sanders et al., 2011] Sanders, B., Bradford, S., et al. (2011). Network implementation of the two-component pressure approach for transient flow in storm sewers. *Journal of Hydraulic Engineering*, 137:158.

[Sjöberg and CTH., 1982] Sjöberg, A. and CTH. (1982). *The Sewer Network Models DAGVL-A and DAGVL-DIFF.* Water Resource Publications.

[Song et al., 1983] Song, C., Cardle, J., and Leung, K. (1983). Transient mixed-flow models for storm sewers. *Journal of hydraulic engineering*, 109(11):1487–1504.

[Sturm, 2001] Sturm, T. W. (2001). *Open Channel Hydraulics*. McGraw-Hill, 1 edition.

[Toro, 2009] Toro, E. (2009). *Riemann solvers and numerical methods for fluid dynamics: a practical introduction*. Springer Verlag.

[Toro et al., 1994] Toro, E., Spruce, M., and Speares, W. (1994). Restoration of the contact surface in the hll-riemann solver. *Shock waves*, 4(1):25–34.

[Toro, 2001] Toro, E. F. (2001). *Shock-Capturing Methods for Free-Surface Shallow Flows*. WILEY.

[Trajkovic et al., 1999] Trajkovic, B., Ivetic, M., Calomino, F., and D'Ippolito, A. (1999). Investigation of transition from free surface to pressurized flow in a circular pipe. *Water science and technology*, 39(9):105–112.

[Tran, 2011] Tran, P. (2011). Propagation of pressure waves in two-component bubbly flow in horizontal pipes. *Journal of Hydraulic Engineering*, 137:668.

[Trindade and Vasconcelos, 2011] Trindade, B. and Vasconcelos, J. (2011). Numerical simulation of water pipeline filling events with limited ventilation. ASCE.

[Vasconcelos, 2005] Vasconcelos, J. (2005). *Dynamic approach to the description of flow regime transition in stormwater systems*. PhD thesis, University of Michigan.

[Vasconcelos and Wright, 2004] Vasconcelos, J. and Wright, S. (2004). Numerical modeling of the transition between free surface and pressurized flow in storm sewers. *Innovative modeling of urban water systems, Monograph*, 12:189–214.

[Vasconcelos and Wright, 2009] Vasconcelos, J. and Wright, S. (2009). Investigation of rapid filling of poorly ventilated stormwater storage tunnels. *Journal of hydraulic research*, 47(5):547–558.

[Vasconcelos et al., 2006] Vasconcelos, J., Wright, S., and Roe, P. (2006). Improved simulation of flow regime transition in sewers: Two-component pressure approach. *Journal of Hydraulic Engineering*, 132:553.

[Vasconcelos et al., 2009a] Vasconcelos, J., Wright, S., and Roe, P. (2009a). Numerical oscillations in pipe-filling bore predictions by shock-capturing models. *Journal of Hydraulic Engineering*, 135:296.

[Vasconcelos, 2007] Vasconcelos, J. G. (2007). *Métodos Numéricos Aplicados a Escoamentos Hidráulicos*. Faculdade de Tecnologia.

[Vasconcelos et al., 2009b] Vasconcelos, J. G., Moraes, J. R. S., and Gebrim, D. V. B. (2009b). Field measurements and numerical modeling of a water pipeline filling events. In *Event Proc. 33rd IAHR Congress*.

[Vasconcelos and Trindade, 2011] Vasconcelos, J. G. and Trindade, B. C. (2011). Discretized air phase modeling in the simulation of pipeline refilling operations.

[Vasconcelos and Wright, 2005] Vasconcelos, J. G. and Wright, S. J. (2005). Experimental investigation of surges in a stormwater storage tunnel. *Journal of Hydraulic Engineering*, 131(10):853–861.

[Vasconcelos, 2008] Vasconcelos, J. G., M. D. T. B. (2008). Applicability of transient flow models to water mains subjected to flow regime transition. In *Proc. XXXI Interamerican Congress in Sanitary Engineering, Santiago, Chile*.

[Wiggert, 1972] Wiggert, D. (1972). Transient flow in free-surface, pressurized systems. *Journal of the Hydraulics division*, 98(1):11–27.

[WISNER and Bucarest, 1967] WISNER, P. and Bucarest, R. (1967). Air demand and pulsatory pressures in bottom outlets. *Rapport sur la réunion*, 1:46.

[Wylie and Streeter, 1993] Wylie, E. B. and Streeter, V. L. (1993). *Fluid Tansients*. McGraw-Hill, 9 edition.

[Zhou, 2000] Zhou, F. (2000). *Effects of trapped air on flow transients in rapidly filling sewers/–by Fayi Zhou.* PhD thesis, University of Alberta.

[Zhou et al., 2002a] Zhou, F. et al. (2002a). Transient flow in a rapidly filling horizontal pipe containing trapped air. *Journal of Hydraulic Engineering*, 128(6).

[Zhou et al., 2002b] Zhou, F., Hicks, F. E., and Steffler, P. M. (2002b). Observations of air–water interaction in a rapidly filling horizontal pipe. *Journal of Hydraulic Engineering*, 128(6):635–639.

[Zhou et al., 2011] Zhou, L., Liu, D., and Zhang, Q. (2011). The influence of entrapped air pockets on hydraulic transients in water pipelines. *Journal of Hydraulic Engineering*, 1:264.